Molecular Design and Realization of Highly Efficient Thermally Activated Delayed Fluorescence Emitters for Organic Light-Emitting Diodes

Yoshimasa Wada

2020

Contents

General Introduction

I. Backgrounds

Organic light-emitting diodes (OLEDs) are one of the most attractive lighting sources because of their advantages: thinness, light-weight, low power consumption, and fast response time. In the early stage of OLEDs research, fluorescent materials (e.g. tris(8-hydroxyquinolinato)aluminium (Alq_3)) were widely used [1]. However, singlet/triplet excitons are generated in 1/3 ratio by charge recombination due to spin statistic, and only 25% of excitons can decay radiatively while 75% of excitons decay non-radiatively. Subsequently, phosphorescent materials (e.g. tris(2-phenylpyridinato)iridium(III) ($Ir(ppy)_3$)) were developed to improve the exciton utilization efficiency and realized 100% of internal quantum efficiency [2]. This is because phosphorescent materials containing heavy metal atoms such as iridium (Ir) and platinum (Pt) in its molecular structure can decay radiavely even from triplet to ground singlet state due to heavy atom effect. More recently, thermally activated delayed fluorescence (TADF) materials are developed [3]. TADF materials require no metal atom in its molecular structure without sacrificing exciton utilization and thus considered to be promising alternative to

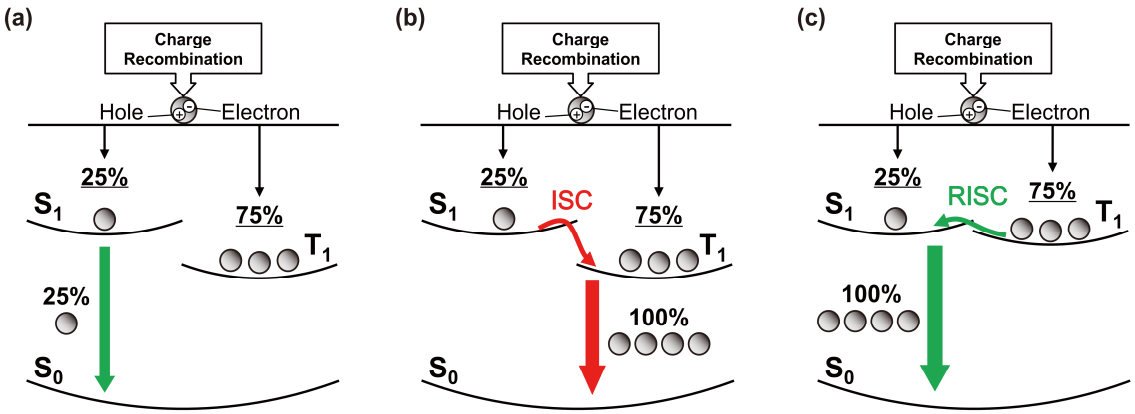

Figure I. Emission scheme in OLEDs for (a) fluorescent (b) phosphorescent, and (c) TADF materials.

phosphorescent materials. Schematic mechanisms for fluorescent, phosphorescent, and TADF materials are summarized in Figure I.

TADF materials and their molecular design

TADF materials can up-convert triplet excitons into singlet excitons through reverse intersystem crossing (RISC) by thermal energy. Thereby 100% of excitons fluoresce from singlet states in OLEDs. In order to achieve efficient RISC, the energy gap (ΔE_{ST}) between lowest excited singlet (S_1) and lowest triplet (T_1) states should be small. Considering two molecular orbitals and two electrons system, electron transition takes place within them and ΔE_{ST} can be written as the following equation (1). Here, $\boldsymbol{r}_1$ and $\boldsymbol{r}_2$ denotes a position space of first electron and second electron, respectively, and φ_i and φ_f denotes a wave function before and after the electron transition, respectively.

$$\Delta E_{ST} \propto \left\langle \varphi_i(\boldsymbol{r_2})\varphi_f(\boldsymbol{r_1}) \middle| \frac{1}{|\boldsymbol{r_1}-\boldsymbol{r_2}|} \middle| \varphi_i(\boldsymbol{r_1})\varphi_f(\boldsymbol{r}_2) \right\rangle \quad (1)$$

From the eq. (1), ΔE_{ST} can be small when the overlap between φ_i and φ_f is small. However, conventional organic aromatic molecules (e.g. anthracene) are likely to be ππ*-like S_1 and T_1 states, which bring about large overlap between φ_i and φ_f. The large overlap results in large ΔE_{ST} of 0.5-1.0 eV, which is far beyond the thermal energy of ~ 0.026 eV. In order to realize small ΔE_{ST}, separation of φ_i and φ_f, which intuitively correspond to frontier molecular orbitals (HOMO and LUMO), should be promising. Adachi and his coworkers have tackled this issue by combining electron donor and acceptor fragments in one molecule, and realized purely organic efficient TADF materials [3, 4]. Among the molecules, ΔE_{ST} of most efficient TADF material of 4CzIPN was experimentally determined to be small value of 0.083 eV.

Mechanism of RISC process

Since the pioneering work, vast amount of effort has been devoted to develop efficient TADF molecules [5-7]. However, the RISC mechanism of TADF materials has not yet been fully understood. RISC was originally considered to be taken place between S_1 and T_1 states and spin-mixing between these two states is responsible for the efficient RISC as described in following equation (2) [3]. Here, λ and H_{SO} denotes first-order mixing coefficient and spin-orbit interaction between S_1 and T_1, respectively.

$$\lambda \propto \frac{H_{SO}}{\Delta E_{ST}} \quad (2)$$

As the author mentioned above, most of TADF materials consists of donor and acceptor fragments, and both S_1 and T_1 states are likely to be the same CT states. From the well-known El-Sayed's rule [8], spin-orbit coupling matrix element value (SOCMEV) between the same configurations is zero, and therefore the λ between the S_1 and T_1 states of the same CT states vanishes. More recently, it has been reported that higher lying triplet states, particularly locally excited triplet states (^{3}LE), are responsible for the RISC process [9-16], because SOCMEV between different configuration of ^{3}LE and ^{1}CT states should be significant. Therefore, energy level matching of the three states, ^{3}LE, ^{1}CT, and ^{3}CT is a promising way to achieve efficient and fast RISC. The development of such TADF molecule and its molecular design strategy is one of current interests.

Device structure and fabrication of OLEDs

In 1987, first efficient OLED was demonstrated by C.W. Tang and S.A. Vanslyke, in which the OLED contains only two organic layers sandwiched by anode and cathode [1]. A present OLED generally consists of a stack of organic layers sandwiched by inorganic anode and cathode. Each organic layer has specific function of hole injection (HIL), hole transporting

(HTL), electron blocking (EBL), light emitting (EML), hole blocking (HBL), electron transporting (ETL), and electron injection (EIL) as shown in the Figure II. In general, these organic layers and a cathode are sequentially deposited onto patterned anode substrate in vacuum chamber at low pressure and the resulting devices are finally encapsulated at inert atmosphere. This low pressure (high vacuum) and encapsulation process is highly required so as to avoid oxygen molecules and moisture, which degrade device performances and device lifetime. However, high running cost and large amount of materials loss by using the vacuum chamber are undesirable for wide spread use of OLEDs, and therefore solution processing is highly desired as an alternative approach to vacuum deposition. For instance, inkjet printing uses molecules as much as needed to form the required thickness of film on the target position and do not waste materials. Also the method does not require huge space and running cost which is essential for vacuum deposition apparatus. However, materials used for vacuum deposition cannot be directly diverted to solution processing partly because of low solubility of the materials. Therefore, development of solution-processable materials is required for the solution processed OLED.

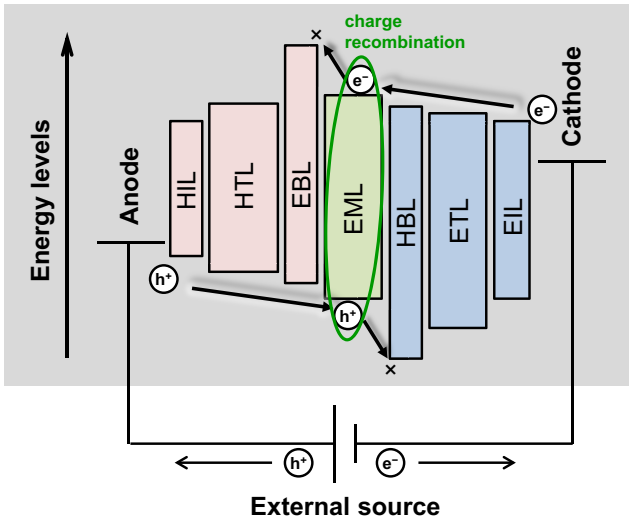

Figure II. Device structure of present OLEDs.

II. Outline of this thesis

The aim of this thesis is to investigate the molecular design for highly efficient TADF molecules, and thereby realize highly efficient OLEDs. The content of this thesis is as follows.

In Chapter 1, a molecular design of highly efficient solution-processable TADF material, is investigated. Solution-processed OLEDs have great potential to achieve easy and low-cost fabrication of large-area flat panel displays and next-generation solid-state lighting sources. Regarding emitting materials, TADF emitters are especially attractive because unlike phosphorescent emitters, they allow high electroluminescence efficiency without using rare metals. Therefore, solution-processed OLEDs using TADF emitters are promising to realize low-cost and highly efficient devices, but there were at that time only a few reports on them [17-20]. In this chapter, the combination of electron donating fragment of 9,9-Dimethyl-9,10-dihydroacridine and electron accepter fragment 2,4,6-triphenyl-1,3,5-triazine (leading to 3ACR-TRZ) is investigated as a potential molecular structure for solution-processable TADF emitter. Theoretical calculation of 3ACR-TRZ predicted that steric hindrance of protons between the donor and the acceptor resulted in large torsion angle between them, which resulted in well-separated HOMO and LUMO. Experimentally, 3ACR-TRZ clearly exhibited TADF with high photoluminescent quantum yield (PLQY) of 97% in a solid-state host layer and the ΔE_{ST} was determined to be very small value of 0.015 eV. Moreover, 3ACR-TRZ displayed a high maximum external quantum efficiency (EQE_{MAX}) of 18.6% in its application to solution-processed OLEDs.

In Chapter 2, solution-processed host-free TADF OLED is investigated. DMAC-TRZ, which composed of the same donor and acceptor core of 3ACR-TRZ, is used as a TADF molecule. Theoretical calculation of DMAC-TRZ predicted that HOMO and LUMO was well-separated and similar TADF performance was expected as well as 3ACR-TRZ. In fact,

DMAC-TRZ exhibited great TADF performance not only in the doped film but also in the neat film (host-free). DMAC-TRZ exhibited PLQY of 84% even in the solution-processed neat film, which indicate that concentration quenching is well suppressed. Furthermore, DMAC-TRZ exhibited bipolar carrier transporting property with both hole and electron mobilities of ~ 10^{-4} cm^2 V^{-1} s^{-1}. From these observation, host-free OLED were fabricated by solution process. Regarding host-free OLEDs, the fabrication process is simplified and film reliability is increased compared with traditional OLEDs containing an emitter doped in a host material as the emitting layer. However, few highly efficient solution-processed host-free OLEDs had been reported at that time. Their EQEs were still low; examples were 5.1% [21], the highest reported at that time, and 3.4% [22], the second highest, for TADF host-free OLEDs. DMAC-TRZ-based solution-processed OLEDs achieved EQE_{MAX} of 17.6%. The value was at that time the highest among all the solution-processed host-free TADF OLEDs.

In Chapter 3, molecular design of thermally-stable and solution-processable deep-blue TADF materials are are investigated. Although efficient deep-blue emitters are essential to achieve excellent color reproducibility and low energy consumption for OLEDs, molecular design is relatively difficult in the deep-blue region, and furthermore, the design of solution-processable materials is even more difficult. Adachi and coworkers have demonstrated excellent device performance for *vacuum-processed* TADF OLEDs showing EQE of 19.2% with Commission International de l'Eclairage (CIE) coordinate of CIE(0.148, 0.098) [23]. However, for *solution-processed* TADF OLEDs, no EQE higher than the limitation of normal fluorescence-based OLEDs (5.0–7.5%) with $y < 0.15$ in CIE coordinates had yet been reported at that time. There is a trade-off in TADF molecular design between solution-processability, deepness of blue emission color, and TADF efficiency. In this chapter, adamantyl substitution strategy is reported to overcome the trade-off and to simultaneously realize "deep-blue",

"thermally stable", and "solution-processable" TADF emitters. As the author introduced above in Chapter 1 and 2, molecular structure containing 9,9-dimethyl-9,10-dihydroacridine and 2,4,6-triphenyl-1,3,5-triazine was found out to be promising for solution-processing, but 3ACR-TRZ and DMAC-TRZ were green and sky-blue TADF emitters, respectively. Here, solution-processable deep-blue three TADF emitters, MA-TA, FA-TA, and PA-TA, were realized by simply introducing adamantyl substituents to their molecular structures. Adamantyl substituents have been introduced to molecular frameworks to improve "physical" properties, but their "electron donating" behavior had not been fully utilized in TADF molecules. As demonstrated in this chapter, this behavior dramatically changes the molecular "electronic" properties and is crucial to achieve efficient deep-blue emission. As a result, the *adamantyl substitution* simultaneously endowed high solubility, excellent thermal stability, and efficient deep-blue emission. An EQE of 22.1% with blue electroluminescence, having CIE(0.15, 0.19), is achieved. This EQE was the highest yet among *solution-processed* TADF OLEDs with $y <$ 0.20 in CIE(x, y) coordinates, and comparable to even that of a *solution-processed* phosphorescent OLED (EQE of 18.2% in CIE(0.14, 0.18)) at that time [24]. Our second device shows much deeper blue emission of CIE(0.15, 0.13) with EQE of 11.2%, which was likewise the highest EQE yet for *solution-processed* TADF OLEDs with $y < 0.15$ in CIE(x, y) coordinates.

In Chapter 4, systematic molecular design to achieve very fast RISC is investigated. Since the pioneering work by Adachi's group [3], RISC has been enabled in TADF molecules by minimizing the energy gap ΔE_{ST} between lowest triplet state (T_1) and lowest excited singlet state (S_1). However, the present TADF molecules are charge transfer (CT) type to make ΔE_{ST} small. From the well-known El-Sayed rule, transitions between T_1 and S_1 with the same CT character (i.e. ^{3}CT and ^{1}CT, respectively) are forbidden because of its vanishingly small spin-orbit

coupling (SOC). Therefore, the RISC process in such molecules is relatively ineffective and slow. To realize fast RISC, a large SOC is required in addition to a small ΔE_{ST}. The realization of fast RISC is of current interest. Many researchers have tackled this problem and intervention of locally excited triplet state (^{3}LE) between ^{3}CT and ^{1}CT has been reported to be an effective approach [10]. Molecules with energy matching of the three states, $E(^3\text{CT}) \approx E(^3\text{LE}) \approx E(^1\text{CT})$, where E(X) denotes the energy level of the X state, is the ideal situation. However, no concrete molecular design principles have been proposed or established to date. This chapter propose a systematic and robust molecular design approach to achieve very fast k_{RISC}. The ideal energy level matchings was realized not only between ^{1}CT and ^{3}CT but also between ^{1}CT and ^{3}LE by optimizing the intersegment distance between face-to-face aligned donor and acceptor moieties in a molecule. However, in contrast to the guiding principles of the previous studies mentioned above, this energy level matching alone was still insufficient for fast RISC; the SOC of the above completely face-to-face system is almost zero, even between the ^{1}CT and ^{3}LE. This problem was found to be solved by simply "*tilting*" the face-to-face alignment. A donor-acceptor combination with a triptycene scaffold realized this tilted face-to-face alignment with optimal intersegment distance. The molecule, named TpAT-tFFO, successfully realized the fastest RISC rate constant of more than 10^7 s^{-1} among all organic systems composed of hydrogen, carbon, and nitrogen atoms, beyond the frame of TADF as known to date.

In Chapter 5, direct RISC between CT-type singlet and triplet states is theoretically and experimentally investigated. As the author mentioned above, present efficient TADF molecules are likely to be the similar CT states (i.e. ^{3}CT and ^{1}CT respectively) and inclusion of different configuration such as ^{3}LE is responsible for the efficient RISC in such TADF materials. On the contrary to this, Chapter 3 reported a highly efficient deep-blue TADF material, MA-TA, where the energy levels of ^{3}LE lie too high (compared to those of both CT-type S_1 and T_1 states) to

participate in the TADF process. In this chapter, the RISC process on MA-TA was investigated. Owing to the simple energy level diagram, it was found, both from theoretically and experimentally, that efficient RISC is achievable even directly between the CT-type S_1 and T_1 state, whereas higher lying T_n (n = 2,3,4…) states are NOT involved in the RISC process. Moreover, MA-TA was experimentally found to be less sensitive to host polarity and/or polarizability and achieved similar TADF performance even in different host materials, which is opposite behaviour to conventional TADF materials. Details are discussed in the Chapter 5, but this insensitivity can be attributed to the energy level diagram of ^{3}LE > ^{1}CT ≈ ^{3}CT because this order is not affected by the host polarity and/or polarizability. Consequently, the molecular design where ^{3}LE > ^{1}CT ≈ ^{3}CT is beneficial not only for achieving efficient RISC, but also for facile device optimization in that emitters is less sensitive to host choice. Here, please note that the results do not contradict to the molecular design, where involvement of any different configuration such as ^{3}LE state "accelerates" the RISC process as discussed in Chapter 4.

III. References

[1] C. W. Tang and S. A. VanSlyke, *Appl. Phys. Lett.* **1987**, *51*, 913.

[2] M. A. Baldo, S. Lamansky, P. E. Burrows, M. E. Thompson and S. R. Forrest, *Appl. Phys. Lett.* **1999**, *75*, 4.

[3] H. Uoyama, K. Goushi, K. Shizu, H. Nomura and C. Adachi, *Nature* **2012**, *492*, 234.

[4] A. Endo, K. Sato, K. Yoshimura, T. Kai, A. Kawada, H. Miyazaki and C. Adachi, *Appl. Phys. Lett.* **2011**, *98*, 083302.

[5] Z. Yang, Z. Mao, Z. Xie, Y. Zhang, S. Liu, J. Zhao, J. Xu, Z. Chi and M. P. Aldred, *Chem. Soc. Rev.* **2017**, *46*, 915.

[6] M. Y. Wong and E. Zysman-Colman, *Adv. Mater.* **2017**, *29*, 1605444.

[7] T. Huang, W. Jiang and L. Duan, *J. Mater. Chem. C* **2018**, *6*, 5577.

[8] M. A. El-Sayed, *J. Chem. Phys.* **1963**, *38*, 2834.

[9] C. M. Marian, *J. Phys. Chem. C* **2016**, *120*, 3715.

[10] M. K. Etherington, J. Gibson, H. F. Higginbotham, T. J. Penfold and A. P. Monkman, *Nat. Commun.* **2016**, *7*, 13680.

[11] F. B. Dias, J. Santos, D. R. Graves, P. Data, R. S. Nobuyasu, M. A. Fox, A. S. Batsanov, T. Palmeira, M. N. Berberan-Santos, M. R. Bryce and A. P. Monkman, *Adv. Sci.* **2016**, *3*, 1600080.

[12] J. Gibson, A. P. Monkman and T. J. Penfold, *Chemphyschem* **2016**, *17*, 2956.

[13] I. Lyskov and C. M. Marian, *J. Phys. Chem. C* **2017**, *121*, 21145.

[14] T. Hosokai, H. Matsuzaki, H. Nakanotani, K. Tokumaru, T. Tsutsui, A. Furube, K. Nasu, H. Nomura, M. Yahiro and C. Adachi, *Sci. Adv.* **2017**, *3*, e1603282.

[15] H. Noda, H. Nakanotani and C. Adachi, *Sci. Adv.* **2018**, *4*, eaao6910.

[16] H. Noda, X.-K. Chen, H. Nakanotani, T. Hosokai, M. Miyajima, N. Notsuka, Y. Kashima, J.-L. Brédas and C. Adachi, *Nat. Mater.* **2019**, *18*, 1084.

[17] K. Kawano, K. Nagayoshi, T. Yamaki and C. Adachi, *Org. Electron.* **2014**, *15*, 1695.

[18] Y. Suzuki, Q. S. Zhang and C. Adachi, *J. Mater. Chem. C* **2015**, *3*, 1700.

[19] R. Komatsu, H. Sasabe, S. Inomata, Y.-J. Pu and J. Kido, *Synth. Met.* **2015**, *202*, 165.

[20] Y. J. Cho, K. S. Yook and J. Y. Lee, *Adv. Mater.* **2014**, *26*, 6642.

[21] M. Y. Wong, G. J. Hedley, G. Xie, L. S. Kölln, I. D. W. Samuel, A. Pertegás, H. J. Bolink and E. Zysman-Colman, *Chem. Mater.* **2015**, *27*, 6535.

[22] K. Albrecht, K. Matsuoka, K. Fujita and K. Yamamoto, *Angew. Chem. Int. Ed.* **2015**, *54*, 5677.

[23] L.-S. Cui, H. Nomura, Y. Geng, J. U. Kim, H. Nakanotani and C. Adachi, *Angew. Chem. Int. Ed.* **2017**, *56*, 1571.

[24] G. Sarada, W. Cho, A. Maheshwaran, V. G. Sree, H.-Y. Park, Y.-S. Gal, M. Song and S.-H. Jin, *Adv. Funct. Mater.* **2017**, *27*, 1701002.

Chapter 1

Highly Efficient Electroluminescence from a Solution-Processable Thermally Activated Delayed Fluorescence Emitter

1.1. Introduction

Solution-processed organic light-emitting diodes (OLEDs) have great potential for low-cost fabrication of large-area flat-panel displays and next-generation solid-state lighting sources. Solution processing has an advantage over vacuum deposition in terms of easy fabrication of large-area OLEDs. However, solution-processed OLEDs have suffered from low device performance when compared with that of vacuum-deposited ones. Much effort has been devoted to improving the luminescence efficiency and stability of solution-processed OLEDs, with phosphorescent emitters being widely used as emitting dopants [1]. Recently, thermally activated delayed fluorescence (TADF) emitters have attracted considerable attention as emitting dopants for OLEDs because unlike phosphorescent emitters, they allow high electroluminescence (EL) efficiency without rare metals, and have diverse chemical structures [2]. Specifically, electron-donating acridan [3-7] (ACR) and electron-accepting triazine [8-17] (TRZ) units have been used as effective building blocks for TADF emitters.

While the use of TADF emitters in vacuum-deposited OLEDs has achieved great success, few reports have been published on TADF-based solution-processed OLEDs [18-21]. In this study, we develop a solution-processable TADF emitter, 2,4,6-tris(4-(9,9-dimethylacridan-10-yl)phenyl)-1,3,5-triazine (3ACR-TRZ, Figure 1.1a). When doped into a solid-state host layer, 3ACR-TRZ shows efficient TADF and high photoluminescence (PL) and EL efficiency. Using 3ACR-TRZ as an emitting dopant, we realize a solution-processed OLED exhibiting a high external quantum efficiency (EQE) of 18.6%.

1.2. Results and discussion

TADF involves thermal activation from triplet excited states (T_n, where $n \geq 1$) to singlet excited states (S_m, where $m \geq 1$) [22]. The EL efficiency of a TADF-based OLED depends largely on the conversion efficiency of T_n to S_m in a TADF emitter. To promote efficient T_n-to-S_m conversion, a TADF emitter is required to have a small energy difference between T_n and S_m. This requirement can be satisfied by spatially separating its frontier orbitals [22]. Figure 1.1a shows the chemical structure of 3ACR-TRZ containing three ACR units and one TRZ unit, the synthesis and characterization of which are presented in Supplementary Information (Supplementary Figure 1.1 and 1.2). Theoretical calculations based on density functional theory (DFT) at the PBE0/6-31G(d) level implemented in the Gaussian 09 program package [23] revealed that 3ACR-TRZ has three quasi-degenerate occupied orbitals and two quasi-degenerate unoccupied molecular orbitals (Figure 1.1a). The highest occupied molecular orbital (HOMO), HOMO−1, and HOMO−2 of 3ACR-TRZ show similar distribution patterns, each being predominantly localized on the ACR units. The lowest unoccupied molecular orbital (LUMO) and LUMO+1 are localized on the central TRZ unit, leading to good spatial separation between the occupied and unoccupied molecular orbitals. Such effective separation is caused by the large torsion angle of almost 90° between the ACR and TRZ units, which originates from steric hindrance between protons of ACR and those of TRZ, as shown in Figure 1.1a. Figure 1.1b displays excitation energies for S_1–S_3 and T_1–T_3 calculated with time-dependent DFT (TD-DFT) at the PBE0/6-31G(d) level (denoted as TD-PBE0/6-31G(d)) in the Gaussian 09 program package. Electronic transitions from the ground state of 3ACR-TRZ to S_1–S_3 and T_1–T_3 can be viewed as electron transfer from the outer ACR units to the central TRZ unit. The theoretical calculations predict that S_1, S_2, and S_3 are luminescent states and almost degenerate. Because T_1, T_2, and T_3 are also almost degenerate, not only S_1 and T_1, but also S_2, S_3, T_2, and T_3 can be

involved in the TADF process. The energy differences between T_n and S_m (n, m = 1–3) are less than 8.8 meV, so they are sufficiently small to allow efficient T_n-to-S_m conversion and generate TADF. These small energy differences originate from the well-separated frontier molecular orbitals of 3ACR-TRZ.

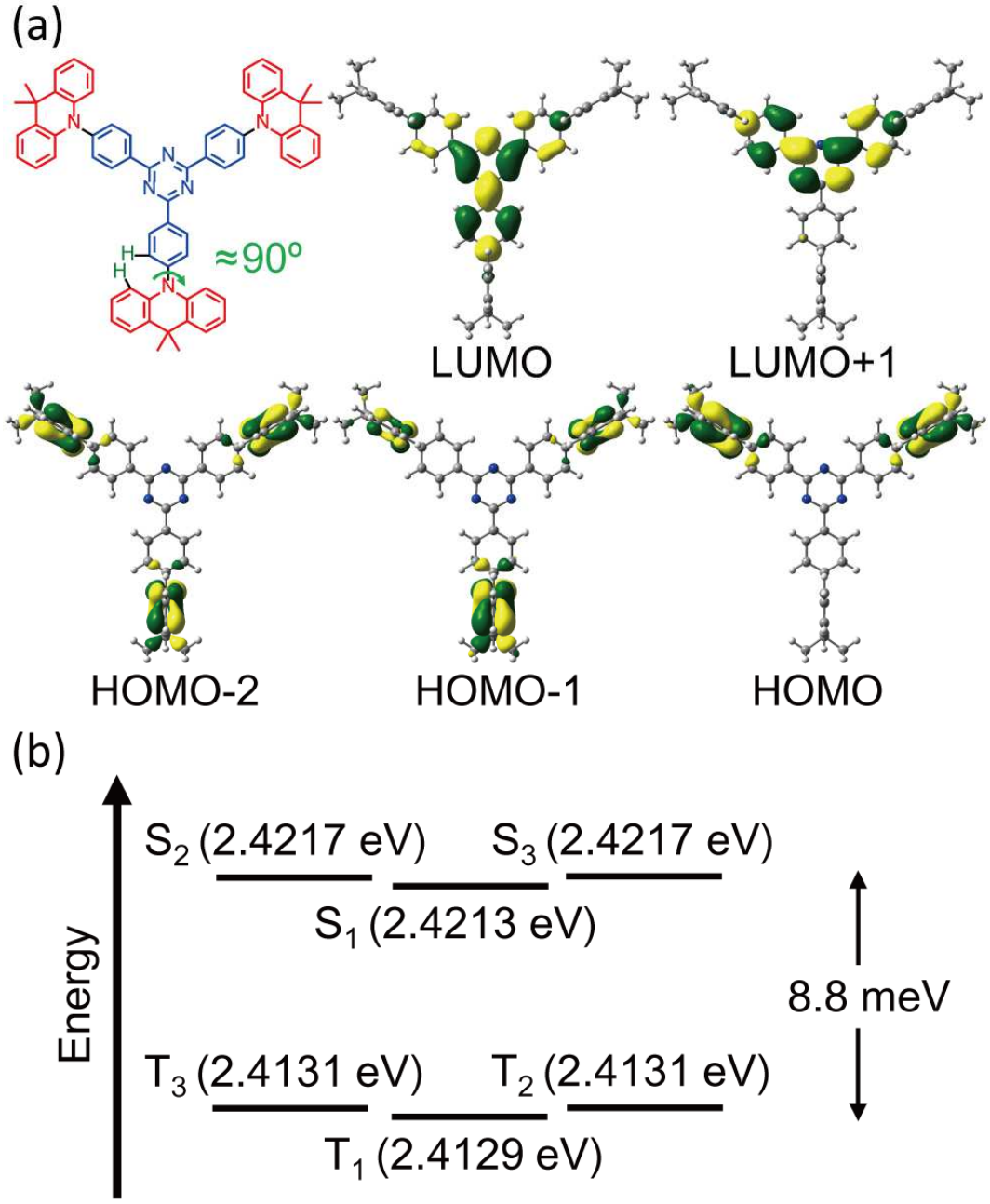

Figure 1.1. (a) Chemical structure of 3ACR-TRZ and its HOMO−2, HOMO−1, HOMO, LUMO, and LUMO+1 calculated at the PBE0/6-31G(d) level of theory. (b) Energy level diagram for low-lying singlet and triplet excited states of 3ACR-TRZ calculated with TD-PBE0/6-31G(d).

Experimentally, 3ACR-TRZ showed TADF behavior and a high photoluminescence quantum yield (PLQY). Figure 1.2 depicts UV-Vis absorption and PL spectra measured for 3ACR-TRZ in toluene solution (1.0×10^{-5} M) at room temperature. The peak maximum of the first absorption band is 391 nm and that of the emission spectrum is 511 nm. The PLQY of the solution sample was 22%. After bubbling Ar gas through the solution for 15 min, the PLQY increased markedly to 94%. The inset of Figure 1.3 shows transient PL decay measurements for the solution of 3ACR-TRZ. Before Ar bubbling, the decay curve contained only a prompt component (intense peak) and no delayed component was found, suggesting that TADF is quenched by molecular oxygen dissolved in the solution [24]. This resulted in a low PLQY of 22%. In contrast, after Ar bubbling, a delayed component (long tail) was clearly observed, showing that triplet states of 3ACR-TRZ survive because of the removal of molecular oxygen from the solution. This observation demonstrates that 3ACR-TRZ shows TADF in toluene solution after Ar bubbling and that efficient T_n-to-S_m (n, m = 1–3) conversion occurs, leading to the increase in PLQY.

To examine the TADF behavior of 3ACR-TRZ in a solid-state host layer, 3ACR-TRZ (16 wt%) was doped into 4,4'-bis(carbazol-9-yl)biphenyl (CBP) host. A 16 wt% 3ACR-TRZ:CBP film was fabricated by spin coating. The emission spectrum of the doped film with a peak maximum at 504 nm using an excitation wavelength of 340 nm was slightly blue shifted compared with that of the toluene solution (Figure 1.2). The doped film showed green emission and a high PLQY of 98%. Emission from CBP was not observed, suggesting that excitation energy is effectively transferred from CBP to 3ACR-TRZ. Figure 1.3 shows transient PL decays of the doped film measured at 100, 200, and 300 K. All decay curves contain prompt and delayed components, and the intensity of the delayed component increases with temperature. Therefore, the delayed component was attributed to TADF. At 300 K, the lifetimes of the prompt

and delayed components were 22 ns and 6.7 μs, respectively. From the transient PL decay profile measured at 300 K, PLQYs for the prompt and delayed components (denoted as Φ_p and Φ_d, respectively) were determined to be 51% and 47%, respectively. The triplet-to-light conversion efficiency is thus calculated to be 96% (= $\Phi_d/(1-\Phi_p)$), which makes 3ACR-TRZ attractive as a TADF emitter for OLEDs. To estimate the singlet–triplet energy gap (ΔE_{ST}) of the doped film, its transient PL decay was measured in increments of 20 K from 100 to 300 K. From an Arrhenius plot of the rate constant for the reverse intersystem crossing from triplet to singlet excited states, ΔE_{ST} was estimated to be 15 meV (Supplementary Figure 1.3 in the Supplementary Information). The method of determining ΔE_{ST} has been described in detail elsewhere [25].

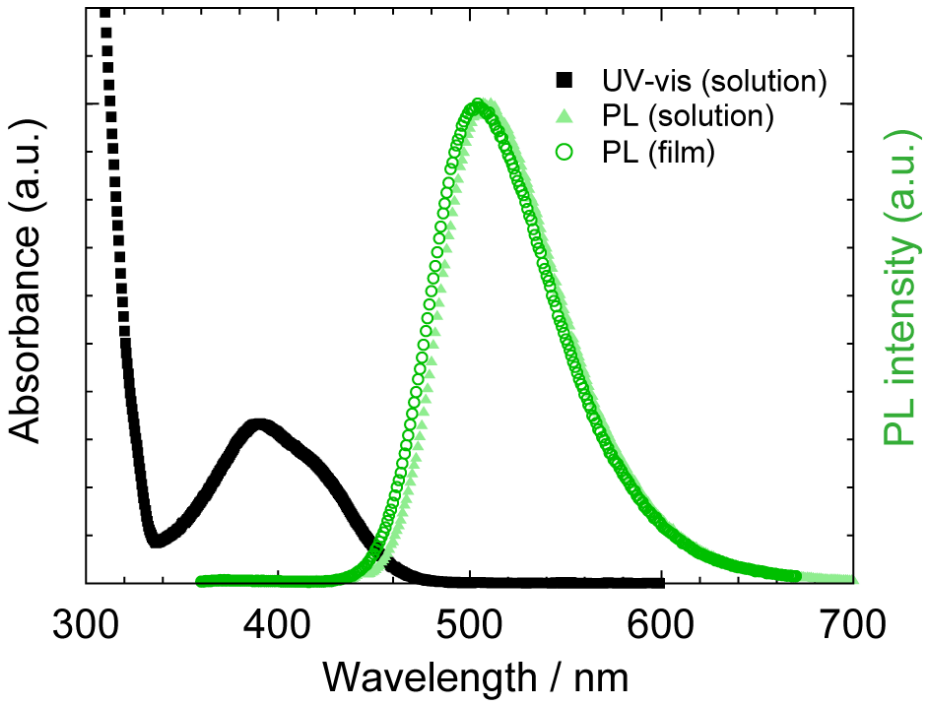

Figure 1.2. UV-Vis absorption and PL spectra for 3ACR-TRZ in toluene solution (1.0×10^{-5} M) together with the PL spectrum for a 16 wt% 3ACR-TRZ:CBP film.

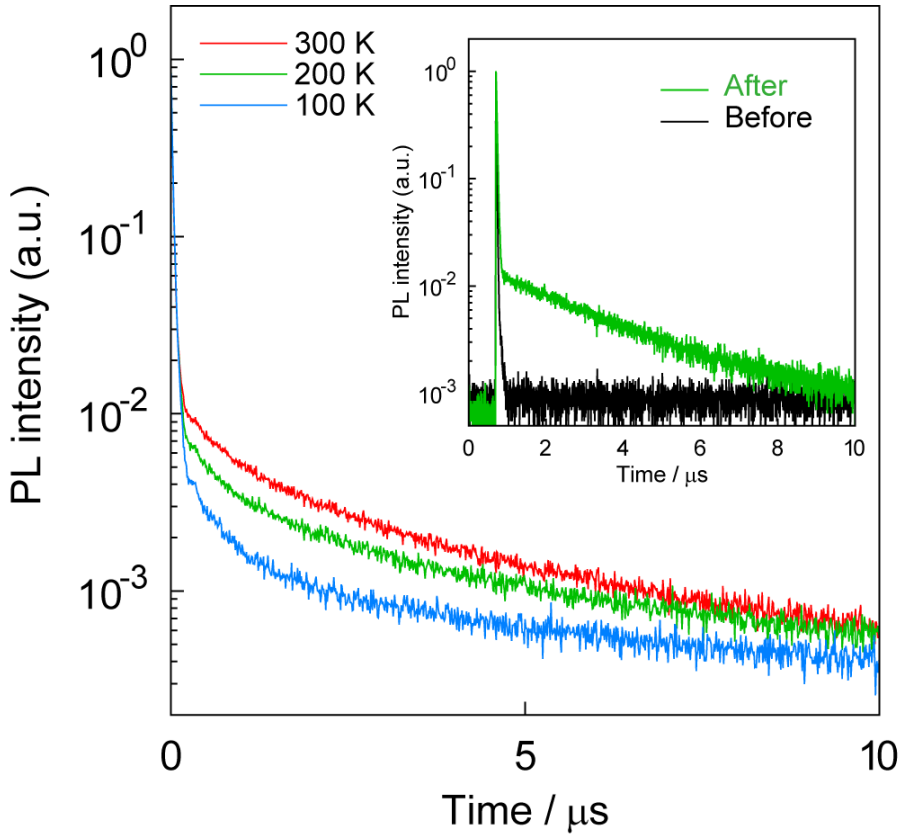

Figure 1.3. Transient PL decay curves for a 16 wt% 3ACR-TRZ:CBP film measured at 100, 200, and 300 K. The inset shows transient PL decay curves for 3ACR-TRZ in toluene solution measured before and after Ar bubbling.

A solution-processed OLED containing 3ACR-TRZ as an emitting dopant was fabricated. The device structure was indium tin oxide (ITO) (50 nm)/poly(3,4-ethylenedioxythiophene)–poly(styrenesulfonate) (PEDOT:PSS) (35 nm)/16 wt% 3ACR-TRZ:CBP (55 nm)/1,3-bis[3,5-di(pyridin-3-yl)phenyl]benzene (BmPyPhB) (30 nm)/lithium quinolin-8-olate (Liq) (1 nm)/Al (80 nm). An energy diagram of this device is provided in Supplementary Figure 1.4. The PEDOT:PSS (Heraeus, AI 4083) layer was spin-coated on a pre-cleaned ITO substrate at 4000 rpm for 10 s. The substrate was then dried at 120 °C for 30 min. To form the emitting layer, 3ACR-TRZ (16 wt%) was mixed with CBP and dissolved in chloroform. The combined weight of 3ACR-TRZ and CBP was 10 mg. The solution (10 mg/mL) was stirred with a stirrer bar for 25 min. The emitting layer was then spin coated on the PEDOT:PSS layer at 1000 rpm for 30 s. The layers were dried at 30 °C for 25 min under vacuum and then moved to a vacuum chamber. After heating the substrate at 90 °C for 20 min, the electron-transporting layer (BmPyPhB), electron-injection layer (Liq), and cathode (Al) were sequentially deposited. BmPyPhB and Liq were deposited at a pressure of 2×10^{-5} Pa and deposition rate of < 1.0 Å s^{-1}. Al was deposited at a pressure of 2×10^{-4} Pa and deposition rate of < 1.5 Å s^{-1}. Figure 1.4 shows current density–EQE characteristics and EL spectrum of the device. The OLED exhibited green emission with a maximum EQE of 18.6% at a current density of 0.06 mA cm^{-2}.

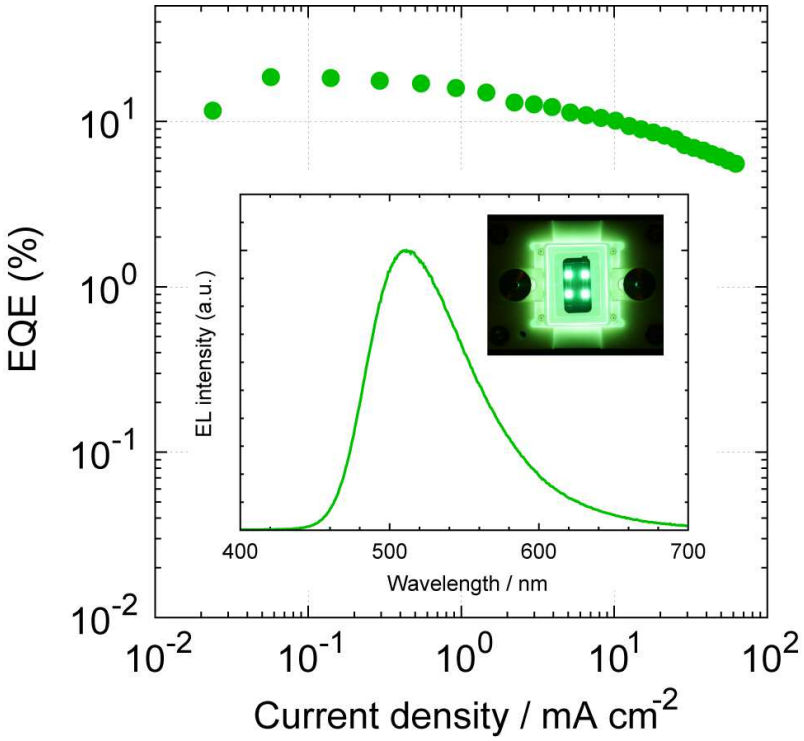

Figure 1.4. Current density–EQE characteristics of a solution-processed OLED. The inset shows the EL spectrum of the device at a current density of 1×10^3 cd m^{-2}, and the photograph shows EL emission from the OLED.

Contributions from prompt emission and TADF to the experimental EQE can be estimated from Φ_p and Φ_d values (51% and 47%, respectively, as determined above). The EQE of a TADF-based OLED can be described as follows [26]:

$$\eta_p = 0.25\Phi_p\gamma\eta_{\text{out}} \quad (1)$$

$$\eta_d = \left[0.75 + 0.25\left(1 - \Phi_p\right)\right]\frac{\Phi_{\text{d}}}{1 - \Phi_{\text{p}}}\gamma\eta_{\text{out}} \quad (2)$$

$$\text{EQE} = \eta_{\text{p}} + \eta_{\text{d}} \quad (3)$$

where η_p and η_d denote the contributions from prompt emission and TADF to the EQE, γ and η_{out} are the charge recombination factor and light-outcoupling efficiency of the OLED, respectively. The values of γ and η_{out} are 0–1 and 0.2–0.3, respectively, so $\gamma\eta_{out}$ is considered to be 0–0.3. In our case, the theoretical EQE is consistent with the experimental maximum EQE of 18.6% when $\gamma\eta_{out}$ = 0.193, leading to η_p = 2.46% and η_d=16.17%. Therefore, η_d is much larger than η_p, suggesting that TADF contributes substantially to the maximum EQE of the device.

1.3. Conclusion

In summary, we developed a green TADF emitter, 3ACR-TRZ, suitable for use in solution-processed OLEDs. Transient PL decay measurements of a 16 wt% 3ACR-TRZ:CBP film confirmed that 3ACR-TRZ emitted TADF with a high PLQY of 98%. A solution-processed OLED containing 3ACR-TRZ as an emitting dopant displayed a maximum EQE of 18.6%. These results further confirm that TADF emitters with diverse chemical structures can realize high EL efficiency without using rare metals. Solution-processable TADF emitters such as 3ACR-TRZ have great potential for developing low-cost large-area OLEDs.

1.4. References

[1] L. Duan, L. Hou, T.-W. Lee, J. Qiao, D. Zhang, G. Dong, L. Wang and Y. Qiu, *J. Mater. Chem.* **2010**, *20*, 6392.

[2] H. Uoyama, K. Goushi, K. Shizu, H. Nomura and C. Adachi, *Nature* **2012**, *492*, 234.

[3] K. Nasu, T. Nakagawa, H. Nomura, C. J. Lin, C. H. Cheng, M. R. Tseng, T. Yasuda and C. Adachi, *Chem. Commun.* **2013**, *49*, 10385.

[4] T. Takahashi, K. Shizu, T. Yasuda, K. Togashi and C. Adachi, *Sci. Technol. Adv. Mater.* **2014**, *15*, 034202.

[5] H. Ohkuma, T. Nakagawa, K. Shizu, T. Yasuda and C. Adachi, *Chem. Lett.* **2014**, *43*, 1017.

[6] Q. Zhang, B. Li, S. Huang, H. Nomura, H. Tanaka and C. Adachi, *Nat. Photon.* **2014**, *8*, 326.

[7] W.-L. Tsai, M.-H. Huang, W.-K. Lee, Y.-J. Hsu, K.-C. Pan, Y.-H. Huang, H.-C. Ting, M. Sarma, Y.-Y. Ho, H.-C. Hu, C.-C. Chen, M.-T. Lee, K.-T. Wong and C.-C. Wu, *Chem. Commun.* **2015**, *51*, 13662.

[8] A. Endo, K. Sato, K. Yoshimura, T. Kai, A. Kawada, H. Miyazaki and C. Adachi, *Appl. Phys. Lett.* **2011**, *98*, 083302.

[9] K. Sato, K. Shizu, K. Yoshimura, A. Kawada, H. Miyazaki and C. Adachi, *Phys. Rev. Lett.* **2013**, *110*, 247401.

[10] T. Serevicius, T. Nakagawa, M. C. Kuo, S. H. Cheng, K. T. Wong, C. H. Chang, R. C. Kwong, S. Xia and C. Adachi, *Phys. Chem. Chem. Phys.* **2013**, *15*, 15850.

[11] H. Tanaka, K. Shizu, H. Miyazaki and C. Adachi, *Chem. Commun.* **2012**, *48*, 11392.

[12] H. Tanaka, K. Shizu, H. Nakanotani and C. Adachi, *Chem. Mater.* **2013**, *25*, 3766.

[13] K. Shizu, M. Uejima, H. Nomura, T. Sato, K. Tanaka, H. Kaji and C. Adachi, *Phys. Rev. Applied* **2015**, *3*, 014001.

[14] Y. Sakai, Y. Sagara, H. Nomura, N. Nakamura, Y. Suzuki, H. Miyazaki and C. Adachi,

Chem. Commun. **2015**, *51*, 3181.

[15] J. Lee, K. Shizu, H. Tanaka, H. Nakanotani, T. Yasuda, H. Kaji and C. Adachi, *J. Mater. Chem. C* **2015**, *3*, 2175.

[16] S. Hirata, Y. Sakai, K. Masui, H. Tanaka, S. Y. Lee, H. Nomura, N. Nakamura, M. Yasumatsu, H. Nakanotani, Q. Zhang, K. Shizu, H. Miyazaki and C. Adachi, *Nat. Mater.* **2015**, *14*, 330.

[17] M. Kim, S. K. Jeon, S.-H. Hwang and J. Y. Lee, *Adv. Mater.* **2015**, *27*, 2515.

[18] K. Kawano, K. Nagayoshi, T. Yamaki and C. Adachi, *Org. Electron.* **2014**, *15*, 1695.

[19] Y. Suzuki, Q. Zhang and C. Adachi, *J. Mater. Chem. C* **2015**, *3*, 1700.

[20] R. Komatsu, H. Sasabe, S. Inomata, Y.-J. Pu and J. Kido, *Synth. Met.* **2015**, *202*, 165.

[21] Y. J. Cho, K. S. Yook and J. Y. Lee, *Adv. Mater.* **2014**, *26*, 6642.

[22] N. J. Turro, V. Ramamurthy and J. C. Scaiano, University Science Books, Sausalito, California, USA, **2010**.

[23] M. J. Frisch, G. W. Trucks, H. B. Schlegel, G. E. Scuseria, M. A. Robb, J. R. Cheeseman, G. Scalmani, V. Barone, B. Mennucci, G. A. Petersson, H. Nakatsuji, M. Caricato, X. Li, H. P. Hratchian, A. F. Izmaylov, J. Bloino, G. Zheng, J. L. Sonnenberg, M. Hada, M. Ehara, K. Toyota, R. Fukuda, J. Hasegawa, M. Ishida, T. Nakajima, Y. Honda, O. Kitao, H. Nakai, T. Vreven, J. A. Montgomery, J. E. Peralta, F. Ogliaro, M. Bearpark, J. J. Heyd, E. Brothers, K. N. Kudin, V. N. Staroverov, R. Kobayashi, J. Normand, K. Raghavachari, A. Rendell, J. C. Burant, S. S. Iyengar, J. Tomasi, M. Cossi, N. Rega, J. M. Millam, M. Klene, J. E. Knox, J. B. Cross, V. Bakken, C. Adamo, J. Jaramillo, R. Gomperts, R. E. Stratmann, O. Yazyev, A. J. Austin, R. Cammi, C. Pomelli, J. W. Ochterski, R. L. Martin, K. Morokuma, V. G. Zakrzewski, G. A. Voth, P. Salvador, J. J. Dannenberg, S. Dapprich, A. D. Daniels, Ö. Farkas, J. B. Foresman, J. V. Ortiz, J. Cioslowski and D. J. Fox, GAUSSIAN 09, Revision C.01, Gaussian, Inc., Wallingford, CT,

2009.

[24] T. Nakagawa, S. Y. Ku, K. T. Wong and C. Adachi, *Chem. Commun.* **2012**, *48*, 9580.

[25] K. Goushi, K. Yoshida, K. Sato and C. Adachi, *Nat. Photon.* **2012**, *6*, 253.

[26] K. Shizu, J. Lee, H. Tanaka, H. Nomura, T. Yasuda, H. Kaji and C. Adachi, *Pure Appl. Chem.* **2015**, *87*, 627.

1.5. Supplementary Information

General procedures

^{1}H and ^{13}C NMR spectra were recorded with a Bruker Avance III 800 MHz spectrometer (800 MHz for ^{1}H NMR spectra and 201 MHz for ^{13}C NMR spectra). Chemical shifts are reported in δ (ppm) using tetramethylsilane as an internal standard. NMR spectra are shown below. The reaction was carried out under Ar atmosphere. UV-Vis and PL spectra (Figure 1.2) were measured using a UV-Vis spectrophotometer (UV-3150, Shimadzu, Japan) and spectrofluorometer (Fluoromax-4P, HORIBA, Japan), respectively. PLQYs were determined using an absolute PLQY spectrometer (Quantaurus-QY C11347-01, Hamamatsu Photonics, Japan). Transient PL decays of the solution (the inset figure in Figure 1.3) were detected using a fluorescence lifetime measurement system (Quantaurus-Tau C11367-02, Hamamatsu Photonics, Japan). The temperature-dependent transient PL decay of the doped film (Figure 1.3) was measured using a fluorescence lifetime measurement system (Quantaurus-Tau C11367-01, Hamamatsu Photonics, Japan) and a cryostat (Oxford Instruments, Optistat DN2, UK). Current density–EQE characteristics (Figure 1.4) were measured using an EQE measurement system (C9920-12, Hamamatsu Photonics, Japan) with a source meter (2400 Broad Purpose SourceMeter, Keithley, Japan).

Synthesis and characterization of 2,4,6-tris(4-(9,9-dimethylacridan-10-yl)phenyl)-1,3,5-triazine (3ACR-TRZ)

[Synthesis]

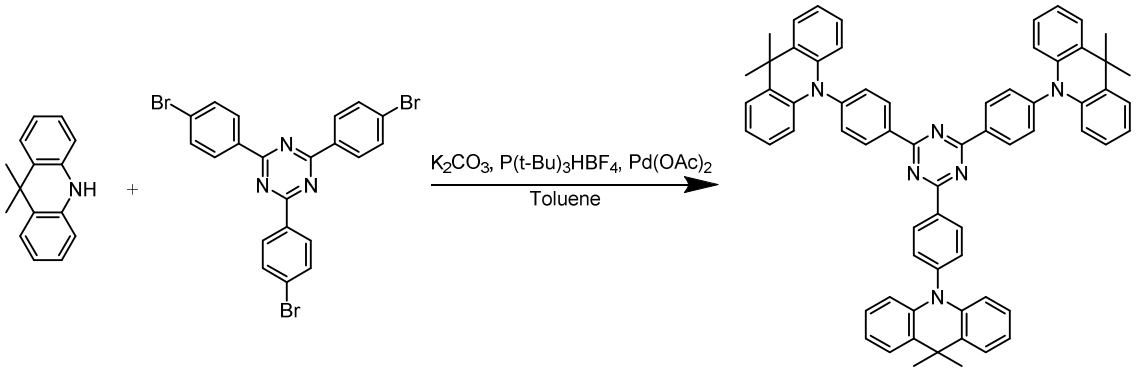

9,9-Dimethylacridan (501 mg, 2.40 mmol), 2,4,6-tris(4-bromophenyl)-1,3,5-triazine (355 mg, 0.649 mmol) potassium carbonate (889 mg 6.43 mmol), tri-*tert*-butylphosphonium tetrafluoroborate (66.5 mg, 0.229 mmol) and palladium(II) acetate (15.0 mg, 66.8 μmol) were dissolved in anhydrous toluene (40.0 mL) and stirred at 121 °C for 24 h. After termination of the reaction, the reaction mixture was poured into distilled water, and extracted with dichloromethane. The organic phase was dried over anhydrous magnesium sulfate, filtered and concentrated under reduced pressure. The crude product was purified by column chromatography on silica gel (chloroform/hexane = 2/3, Rf = 0.53). The obtained product was further purified by recrystallization from toluene to give 451 mg (0.48 mmol, 68%) of 3ACR-TRZ.

[NMR]

^{1}H NMR (800 MHz, $CDCl_3$): δ = 9.08 (d, J = 8.56 Hz, 6H), 7.61 (d, J = 8.48 Hz, 6H), 7.50 (dd, J = 3.88, 1.52 Hz, 6H), 7.00–7.03 (m, 6H), 6.96–6.98 (m, 6H), 6.41 (dd, J = 4.10, 1.6 Hz, 6H), 1.73 (s, 18H); ^{13}C NMR (800 MHz, $CDCl_3$): δ = 171.5, 145.8, 140.6, 135.7, 131.7, 131.6, 130.5, 126.5, 125.4, 121.0, 114.3, 36.1, 31.3.

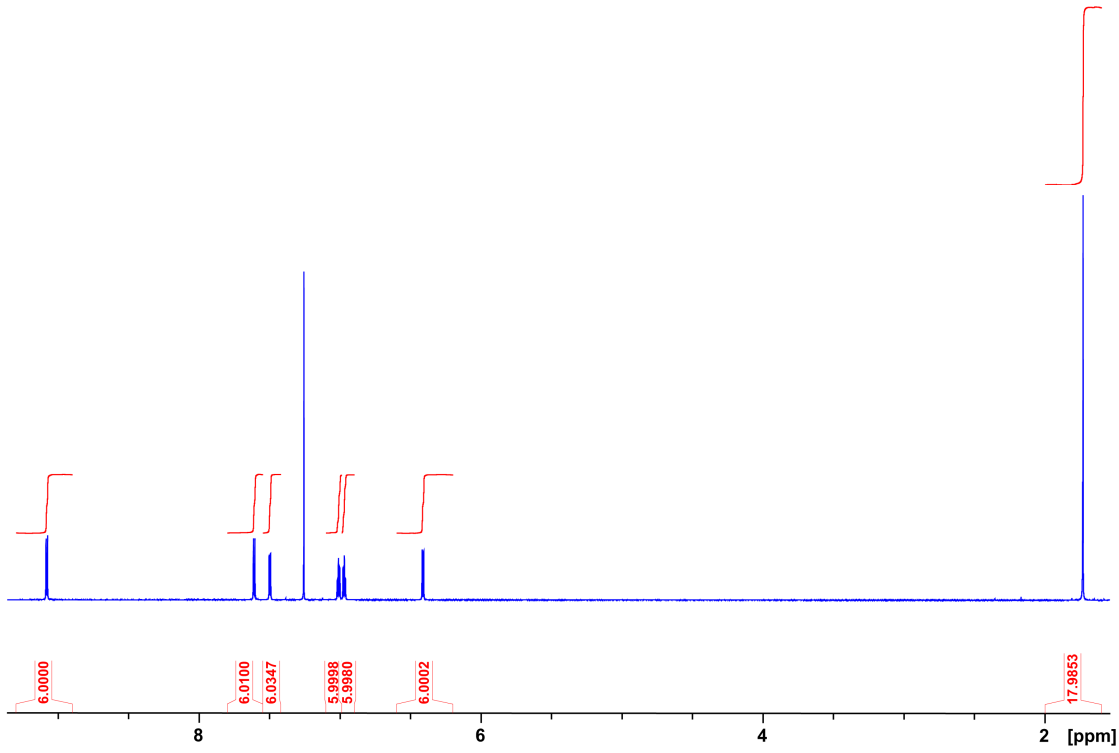

Supplementary Figure 1.1. ^{1}H NMR spectrum of 3ACR-TRZ.

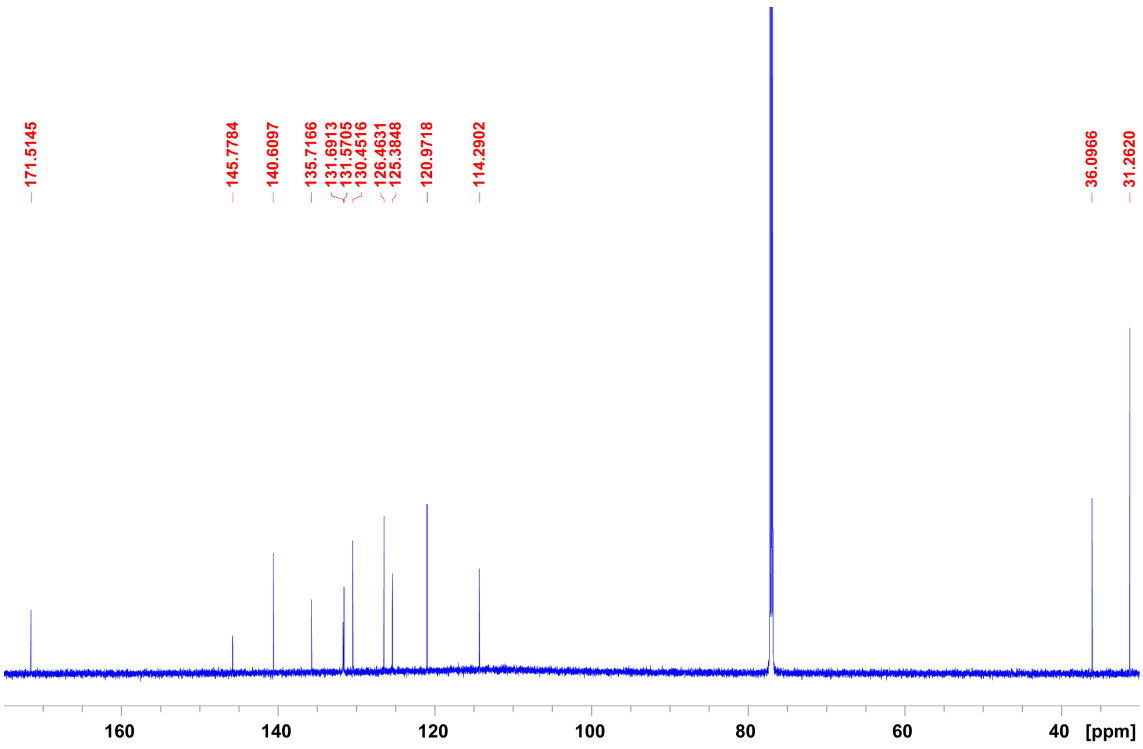

Supplementary Figure 1.2. ^{13}C NMR spectrum of 3ACR-TRZ.

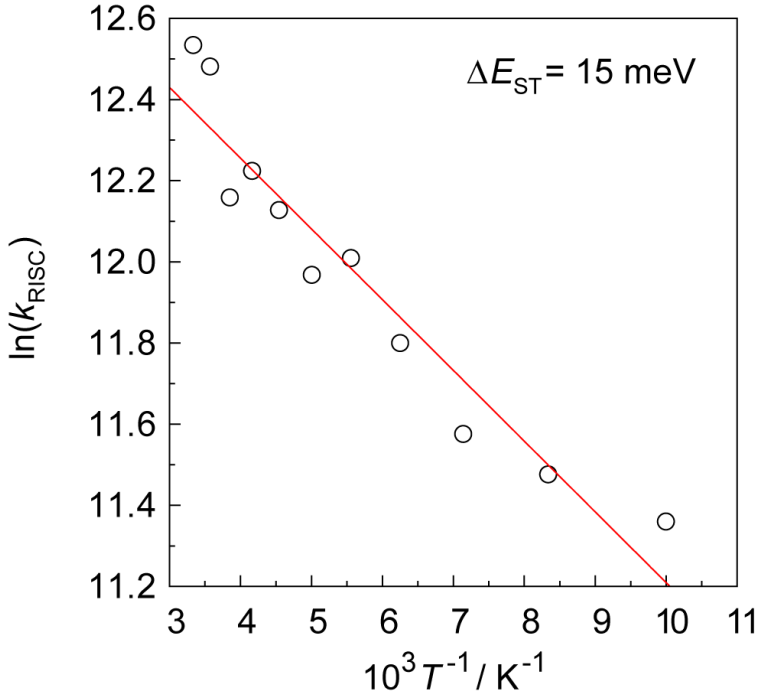

Supplementary Figure 1.3. Arrhenius plot of the rate constant for reverse intersystem crossing (k_{RISC}) from triplet to singlet excited states of a 16 wt% 3ACR-TRZ:CBP film.

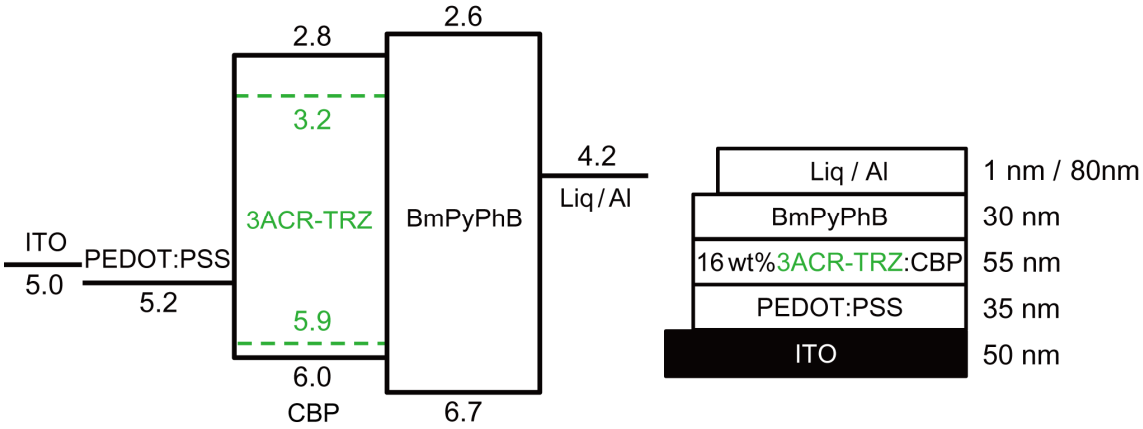

Supplementary Figure 1.4. Energy diagram of a device with the structure ITO/PEDOT:PSS/16 wt% 3ACR-TRZ:CBP/BmPhPhB/Liq/Al (left) and the thickness of each layer (right). The HOMO energy level of 3ACR-TRZ was estimated using a photoelectron spectrometer (Riken Keiki, AC-3) and the LUMO level was estimated from the HOMO level and the absorption edge (460 nm, Figure 1.2) of the UV-Vis absorption spectrum of 3ACR-TRZ.

Chapter 2

Highly Efficient Solution-Processed Host-Free Organic Light-Emitting Diodes Showing an External Quantum Efficiency of Nearly 18% with a Thermally Activated Delayed Fluorescence Emitter

2.1. Introduction

Organic light-emitting diodes (OLEDs) are commercially available as flat-panel displays of smartphones and televisions and attract great attention for use as a next-generation solid-state lighting source. Although vacuum vapor deposition has been widely used to fabricate OLEDs, this method has several drawbacks, such as high production cost, difficulty fabricating multidopant OLEDs, and limited scalability and resolution. Solution processing is a promising alternative to vacuum vapor deposition to fabricate OLEDs because it can lower the production cost and realize large-area high-resolution displays [1, 2]. However, it is difficult to fabricate multilayered OLEDs by solution processing, and OLEDs produced by this method show poor device performance compared with that of vapor-deposited OLEDs.

In conventional OLEDs, the emitting layer is composed of a light-emitting material and host material. The performance of OLEDs depends largely on the choice of host material. The host material should have sufficiently large excited-state energies, bipolar transport properties, and suitable HOMO and LUMO energy levels to achieve high luminescence efficiency and good charge balance. In particular, for solution-processed OLEDs, the choice of host materials is further limited to soluble host materials. Host-free OLEDs (sometimes called non-doped OLEDs) contain only an emitting material in the emitting layer (that is, neat film), which circumvents the limitations of host materials. Furthermore, host-free OLEDs can avoid disadvantages of conventional OLEDs such as: (1) the strong dependence of optical properties

and electroluminescence (EL) efficiency on the combination of emitting dopant and host material; (2) the marked influence of doping concentration on device performance, which makes device optimization difficult; (3) the aggregation of emitting dopants in solution processing, which degrades device performance [3].

Phosphorescent [4, 5] and thermally activated delayed fluorescence (TADF) [6-8] emitters have been used in OLEDs that achieve high performance because these emitters can efficiently convert electrogenerated excitons into light and potentially realize an internal quantum efficiency of nearly 100%. For host-free OLEDs, emitting materials should exhibit weak concentration quenching to realize high photoluminescence quantum yields (PLQYs) of their neat films. Some vacuum deposited neat films of TADF emitter molecules with peripheral substituents to inhibit intermolecular frontier orbital interactions have been found to exhibit high PLQYs; host-free OLEDs using these films as emitting layers have achieved external quantum efficiencies (EQEs) of nearly 20% [9]. In contrast, the PLQYs of neat films of solution-processable emitters are still low, as are EQEs of solution-processed host-free OLEDs (3.4% [10] and 5.1% [11]). Recently, we developed a solution-processable TADF emitter, 2,4,6-tris(4-(9,9-dimethylacridan-10-yl)phenyl)-1,3,5-triazine (3ACR-TRZ) composed of acridan (ACR) and triphenyltriazine (TRZ) fragments (Figure 2.1). Using 3ACR-TRZ as an emitting dopant, we realized a highly efficient solution-processed OLED showing an EQE of 18.6% [12]. At approximately the same time, using a TADF emitter 10-(4-(4,6-diphenyl-1,3,5-triazin-2-yl)phenyl)-9,9-dimethylacridan (DMAC-TRZ), which is composed of the same electron donor and acceptor fragments of 3ACR-TRZ (Figure 2.1), Wong and co-workers realized a highly efficient host-free OLED [13]. Their OLED contained a vapor-deposited neat DMAC-TRZ film as an emitting layer. These observations motivated us to develop host-free OLEDs containing a neat DMAC-TRZ film fabricated by solution processing

as an emitting layer.

In this study, a neat DMAC-TRZ film is prepared by spin coating. The neat film shows a high PLQY of 84%, which is almost identical to that of a DMAC-TRZ film prepared by vacuum vapor deposition. Using a spin-coated neat DMAC-TRZ film as the emitting layer, we fabricate OLEDs with a structure of indium tin oxide (ITO)/poly(3,4-ethylenedioxythiophene)–poly(styrenesulfonate) (PEDOT:PSS)/DMAC-TRZ/1,3-bis[3,5-di(pyridin-3-yl)phenyl]benzene (BmPyPhB) or 4,6-bis(3,5-di(pyridin-4-yl)phenyl)-2-methylpyrimidine (B4PyMPM)/lithium quinolin-8-olate (Liq)/Al. The OLEDs exhibit a maximum EQE (EQE_{MAX}) of 17.6%, which is the highest obtained for solution-processed host-free OLEDs. In addition, a high EQE of 13.7% at a luminance of 1,000 cd m^{-2} is achieved by optimizing the thickness and materials of the electron-transport layer (ETL).

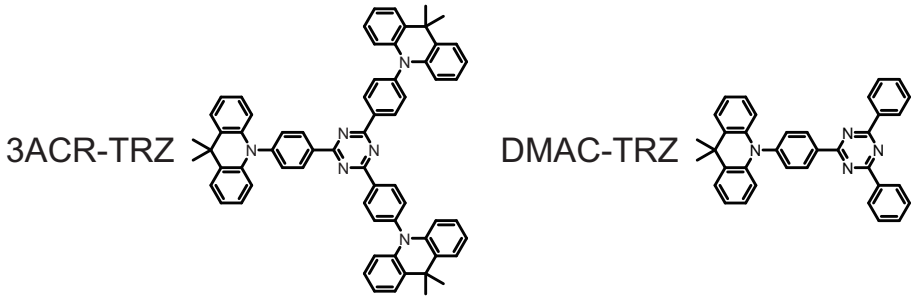

Figure 2.1. Chemical structures of 3ACR-TRZ and DMAC-TRZ.

2.2. Results and discussion

To evaluate DMAC-TRZ as a potential emitter in solution-processed host-free OLEDs, a neat DMAC-TRZ film was fabricated by spin coating. The synthesis and characterization of DMAC-TRZ are provided in the Supplementary Information (Supplementary Figure 2.1). Absorption and photoluminescence (PL) peak maxima of the spin-coated film appeared at 388 and 498 nm, respectively (Figure 2.2a), which are close to those of a vapor-deposited neat DMAC-TRZ film [13]. Transient PL decay measurements revealed that the spin-coated film displayed prompt and delayed fluorescence (Figure 2.2b). The intensity of the delayed component clearly increases with temperature from 100 to 300 K, which is characteristic of TADF emitters. The PLQY of the spin-coated neat film was 84% at 300 K under argon atmosphere; almost identical to the reported PLQY of the vapor-deposited film (83%) [13]. In addition, the PLQY of the spin-coated neat film (84%) was only slightly lower than that of an 8wt% DMAC-TRZ-doped host layer fabricated by vapor deposition (90%) [13], suggesting that the concentration quenching of DMAC-TRZ emission is effectively suppressed even in the spin-coated neat film. Note that the PLQY of 84% is the highest reported for a solution-processed neat film of a TADF [10, 11] or phosphorescent [14] material. From the PL decay curve measured at 300 K, the 84% PLQY is composed of 44% prompt and 40% delayed components. The triplet-to-light conversion efficiency of the spin-coated film was estimated to be at least 71%. In addition, electron and hole mobilities of DMAC-TRZ were determined to be of the order of 10^{-4} and 10^{-5} cm^2 V^{-1} s^{-1}, respectively, by a time-of-flight (TOF) technique (Figure 2.2c), revealing bipolar transport properties. All of these results indicate that DMAC-TRZ is promising as an emitter for solution-processed host-free OLEDs.

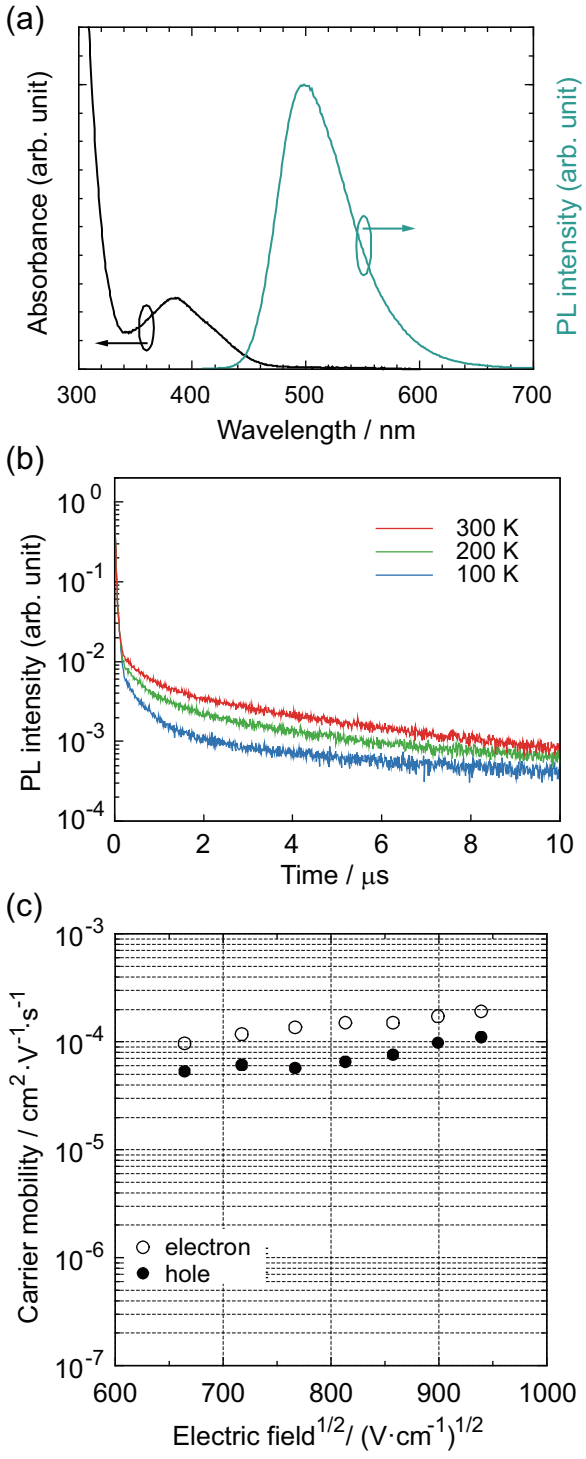

Figure 2.2. (a) UV-vis and PL spectra of a solution-processed DMAC-TRZ neat film. (b) Transient PL decay curves of a solution-processed DMAC-TRZ neat film measured at 100, 200 and 300 K. (c) Electron and hole mobilities of DMAC-TRZ measured by a TOF technique.

We next fabricated solution-processed host-free OLEDs using a neat DMAC-TRZ film as an emitting layer. The device architecture was ITO (50 nm)/PEDOT:PSS (40 nm)/DMAC-TRZ (70 nm)/BmPyPhB or B4PyMPM (*X* nm)/Liq (1 nm)/Al (80 nm) where *X* is 30 or 60. The PEDOT:PSS and DMAC-TRZ layers were spin coated and the following layers were vapor deposited. Detailed information about device fabrication is provided as Supplementary Information. Figure 2.3a shows the energy diagram for the OLEDs and chemical structures of the materials used. When the thickness of the BmPyPhB layer was 30 nm, the highest EQE_{MAX} of 17.6% was obtained at 29.5 cd m^{-2} (Figure 2.3b and Table 2.1). Note that this value is the highest among solution-processed host-free OLEDs reported to date. However, the OLED shows a high turn-on voltage of 4.8 V and low EQEs at high luminance (Table 2.1). The EQE decreased considerably to 10.7% at 100 cd m^{-2} (defined as EQE_{100}) and 2.9% at 1,000 cd m^{-2} (defined as EQE_{1000}). Changing the thickness of the BmPyPhB layer from 30 to 60 nm had little effect on EQE_{MAX} (17.5%), but the device performance improved slightly at high luminance with an EQE_{100} of 11.8% and EQE_{1000} of 4.0%.

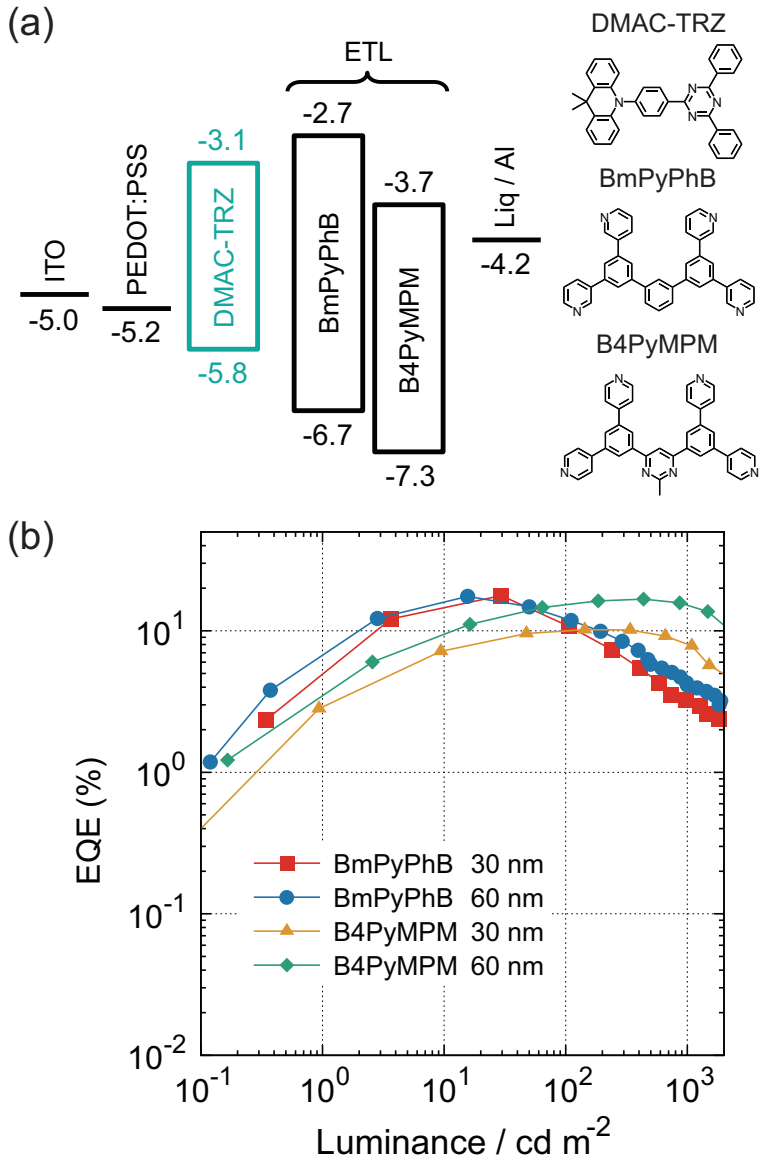

Figure 2.3. (a) Energy diagram of solution-processed host-free OLEDs containing DMAC-TRZ as an emitter. The chemical structures of DMAC-TRZ, BmPyPhB, and B4PyMPM are shown on the right. (b) Luminance–EQE characteristics of solution-processed host-free OLEDs.

Table 2.1. Device performance of solution-processed host-free OLEDs.

ETL	ETL Thickness / nm	EQE_{MAX} (%)	EQE_{100} [a] (%)	EQE_{1000} [b] (%)	Turn on [c] / V
BmPyPhB	30	17.6	10.7	2.9	4.8
	60	17.5	11.8	4.0	4.8
B4PyMPM	30	10.2	10.2	7.8	3.9
	60	16.8	16.3	13.7	4.0

[a] at 100 cd m^{-2}. [b] at 1,000 cd m^{-2}. [c] at 1 cd m^{-2}.

To further improve the device performance, we changed the ETL. While the LUMO energy level of a BmPyPhB layer (−2.7 eV) is higher than that of a DMAC-TRZ layer (−3.1 eV), the LUMO energy level of a B4PyMPM layer (−3.7 eV) [15] is lower than that of a DMAC-TRZ layer, which should facilitate electron injection from Al. At the same time, the HOMO energy level of the B4PyMPM layer (−7.3 eV) is sufficiently low to block holes injected from ITO. We fabricated OLEDs using B4PyMPM as an ETL with thicknesses of 30 and 60 nm. A device with a 30-nm B4PyMPM layer exhibited an EQE_{MAX} of 10.2% at 143 cd m^{-2}, which was lower than EQE_{MAX} of the devices containing BmPyPhB, but the device performance was improved at high luminance. In the case with a 60-nm-thick B4PyMPM layer, the device performance dramatically improved. EQE_{MAX} was 16.8%, comparable to that of the devices with BmPyPhB. It is notable that the EQE_{MAX} was recorded at a high luminance of 436 cd m^{-2}. Furthermore, the device showed a high EQE_{100} of 16.3% and retained a high EQE_{1000} of 13.7%. In addition, the B4PyMPM-based OLEDs exhibited lower turn-on voltages than the BmPyPhB-based ones, as summarized in Table 2.1.

2.3. Conclusion

In summary, we demonstrated highly efficient solution-processed host-free OLEDs. A spin-coated DMAC-TRZ neat film showed a high PLQY of 84%; the highest reported value among solution-processed neat films of TADF and phosphorescent materials. Solution-processed host-free OLEDs using DMAC-TRZ as an emitter exhibited a EQE_{MAX} of 17.6%, which is also the highest value reported for solution-processed host-free OLEDs to date. Our findings indicate that TADF emitters are promising to realize solution-processed host-free OLEDs. Furthermore, we believe this host-free strategy releases deep-blue OLEDs, in particular, from the complication of host investigation. We would like to tackle this issue in the future.

2.4. References

[1] L. Duan, L. Hou, T.-W. Lee, J. Qiao, D. Zhang, G. Dong, L. Wang and Y. Qiu, *J. Mater. Chem.* **2010**, *20*, 6392.

[2] M. Cai, T. Xiao, E. Hellerich, Y. Chen, R. Shinar and J. Shinar, *Adv. Mater.* **2011**, *23*, 3590.

[3] S. Reineke, K. Walzer and K. Leo, *Phys. Rev. B* **2007**, *75*, 125328.

[4] M. A. Baldo, D. F. O'Brien, Y. You, A. Shoustikov, S. Sibley, M. E. Thompson and S. R. Forrest, *Nature* **1998**, *395*, 151.

[5] H. Sasabe and J. Kido, *Eur. J. Org. Chem.* **2013**, *2013*, 7653.

[6] A. Endo, K. Sato, K. Yoshimura, T. Kai, A. Kawada, H. Miyazaki and C. Adachi, *Appl. Phys. Lett.* **2011**, *98*, 083302.

[7] H. Uoyama, K. Goushi, K. Shizu, H. Nomura and C. Adachi, *Nature* **2012**, *492*, 234.

[8] H. Kaji, H. Suzuki, T. Fukushima, K. Shizu, K. Suzuki, S. Kubo, T. Komino, H. Oiwa, F. Suzuki, A. Wakamiya, Y. Murata and C. Adachi, *Nat. Commun.* **2015**, *6*, 8476.

[9] D. X. Ding, Z. Zhang, Y. Wei, P. F. Yan and H. Xu, *J. Mater. Chem. C* **2015**, *3*, 11385.

[10] K. Albrecht, K. Matsuoka, K. Fujita and K. Yamamoto, *Angew. Chem. Int. Ed.* **2015**, *54*, 5677.

[11] M. Y. Wong, G. J. Hedley, G. Xie, L. S. Kölln, I. D. W. Samuel, A. Pertegás, H. J. Bolink and E. Zysman-Colman, *Chem. Mater.* **2015**, *27*, 6535.

[12] Y. Wada, K. Shizu, S. Kubo, K. Suzuki, H. Tanaka, C. Adachi and H. Kaji, *Appl. Phys. Lett.* **2015**, *107*, 183303.

[13] W.-L. Tsai, M.-H. Huang, W.-K. Lee, Y.-J. Hsu, K.-C. Pan, Y.-H. Huang, H.-C. Ting, M. Sarma, Y.-Y. Ho, H.-C. Hu, C.-C. Chen, M.-T. Lee, K.-T. Wong and C.-C. Wu, *Chem. Commun.* **2015**, *51*, 13662.

[14] X. Xu, X. Yang, J. Zhao, G. Zhou and W.-Y. Wong, *Asian J. Org. Chem.* **2015**, *4*, 394.

[15] H. Sasabe, D. Tanaka, D. Yokoyama, T. Chiba, Y.-J. Pu, K.-i. Nakayama, M. Yokoyama and J. Kido, *Adv. Funct. Mater.* **2011**, *21*, 336.

2.5. Supplementary Information

Synthesis and Characterization of DMAC-TRZ.

[Synthesis]

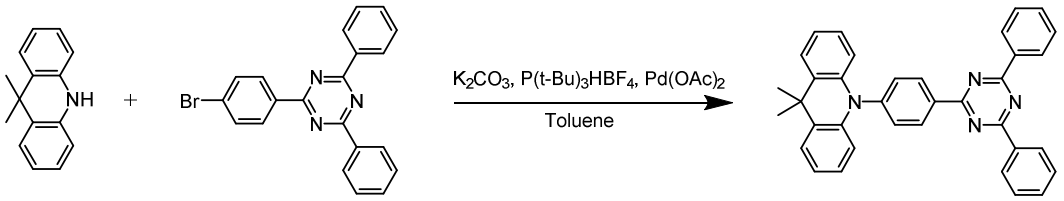

9,9-Dimethylacridan (500 mg, 2.39 mmol), 2-(4-bromophenyl)-4,6-diphenyl-1,3,5-triazine (1.02 g, 2.63 mmol), potassium carbonate (990 mg, 7.16 mmol), tri-*tert*-butylphosphonium tetrafluoroborate (41.6 mg, 0.143 mmol) and palladium(II) acetate (8.05 mg, 35.8 μmol) were dissolved in anhydrous toluene (20.0 mL) and stirred at 121 °C for 16 h under Ar atmosphere. The reaction mixture was cooled to ambient temperature to terminate the reaction and poured into brine. The organic phase was extracted with chloroform, dried over anhydrous magnesium sulfate, filtered and concentrated under reduced pressure. The crude product was purified by column chromatography on silica gel (chloroform/hexane = 1:1, Rf = 0.56) to give 887 mg (1.72 mmol, 71.9%) of DMAC-TRZ. DMAC-TRZ was further purified by sublimation before use. The ^{1}H NMR spectrum of sublimed DMAC-TRZ, recorded with a 600-MHz spectrometer (ECA-600, JEOL, Japan) is shown in Supplementary Figure 2.1. Chemical shifts are reported in δ (ppm) using tetramethylsilane as an internal standard.

[NMR]

^{1}H NMR (600 MHz, $CDCl_3$): δ = 9.03 (d, J = 8.3 Hz, 2H), 8.82 (d, J = 7.2 Hz, 4H), 7.60–7.66 (m, 6H), 7.57 (d, J = 8.3 Hz, 2H), 7.49 (dd, J = 7.6, 1.6 Hz, 2H), 6.95–7.01 (m, 4H), 6.38 (dd, J = 8.1, 1.0 Hz, 2H), 1.73 (s, 6H).

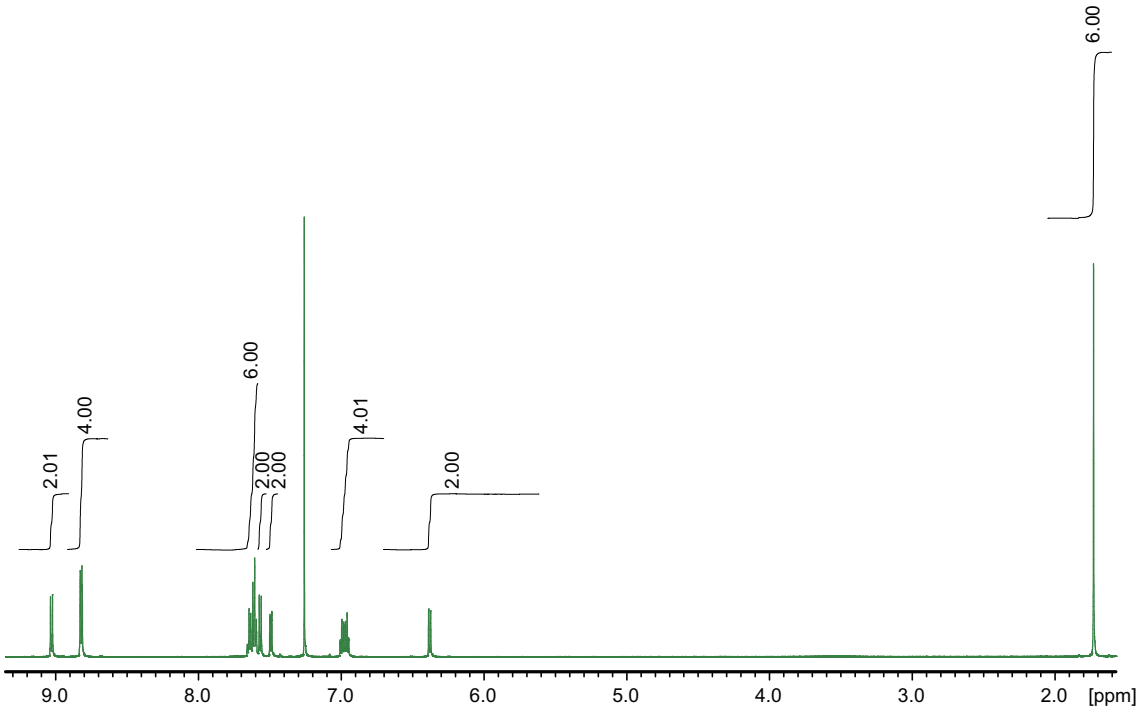

Supplementary Figure 2.1. ^{1}H NMR spectrum of DMAC-TRZ.

Fabrication of OLEDs.

Devices with the structure ITO (50 nm)/PEDOT:PSS (40 nm)/DMAC-TRZ (70 nm)/BmPyPhB or B4PyMPM (*X* nm)/Liq (1 nm)/Al (80 nm) were fabricated as follows. The PEDOT:PSS layer was spin coated on a pre-cleaned ITO substrate at 4000 rpm for 10 s. The substrate was then dried at 120 °C for 30 min and cooled for 10 min under N_2 atmosphere. DMAC-TRZ was dissolved in chloroform to give a concentration of 10 mg mL^{-1}, stirred for 25 min and then spin coated on the PEDOT:PSS layer at 1000 rpm for 30 min. The layers were dried at 30 °C for 25 min under vacuum and then moved to a vacuum chamber. After heating the substrate at 90 °C for 20 min, the ETL (BmPyPhB or B4PyMPM), electron-injection layer (Liq), and cathode (Al) were sequentially deposited. The deposition pressure of the ETL and Liq was ~10^{-5} Pa and that of Al was ~10^{-4} Pa. The deposition rates of ETL, Liq and Al were 0.1–0.2, 0.01–0.02 and 0.1–0.2 nm s^{-1}, respectively.

Characterization of emitting material and OLEDs.

UV-vis and PL spectra of DMAC-TRZ were measured using a UV-vis spectrophotometer (UV-3150, Shimadzu, Japan) and spectrofluorometer (Fluoromax-4P, HORIBA, Japan), respectively. PLQYs were determined using an absolute PLQY spectrometer (Quantaurus-QY C11347-01, Hamamatsu Photonics, Japan). The temperature-dependent transient PL decay of a DMAC-TRZ neat film was measured using a fluorescence lifetime measurement system (Quantaurus-Tau C11367-01, Hamamatsu Photonics, Japan) and a cryostat (Oxford Instruments, Optistat DN2, UK). The HOMO energy level of DMAC-TRZ was estimated using a photoelectron spectrometer (AC-3, Riken Keiki, Japan) and the LUMO level was estimated from the HOMO level and the absorption edge (460 nm) of its UV-vis absorption spectrum. Hole and electron mobilities of DMAC-TRZ were measured with a TOF apparatus (TOF-401-3, Sumitomo Heavy Industries, Japan). The device structure of the TOF sample was ITO (50 nm)/DMAC-TRZ (3.4 μm)/Al (20 nm). A 337-nm N_2 gas laser and 100-Ω resistor were used to generate and detect photocarriers. All measurements were performed at 300 K. Luminance–EQE characteristics were measured using an absolute EQE measurement system (C9920-12, Hamamatsu Photonics, Japan) with a source meter (2400, Keithley, Japan).

Chapter 3

Adamantyl Substitution Strategy for Realizing Solution-Processable Thermally-Stable Deep-Blue Thermally Activated Delayed Fluorescence Materials

3.1. Introduction

Organic light-emitting diodes (OLEDs) have attracted considerable attention as a promising solid-state lighting source and have recently found practical applications in displays for smartphones and televisions. They are potentially flexible, light-weight and cost-effective devices because the bulk of their structure is composed of organic molecules. However, the fabrication process of these devices, vacuum deposition, incurs a large running cost for maintaining the chamber in vacuum. Therefore, solution-processing has been studied as a low-cost alternative. Highly efficient solution-processed OLEDs containing soluble phosphorescent emitters have been developed [1-6]. However, the molecular frameworks of these phosphorescent emitters contain expensive and unevenly distributed heavy metal elements such as Ir, Pt or Au, which hinders the widespread use of OLEDs. This problem has been solved by the use of thermally activated delayed fluorescence (TADF) materials, a more recently developed class of emitter, without sacrificing the light-emitting efficiency. Since the first report of a TADF emitter, 4CzIPN [7], effort has been devoted to develop "*vacuum-processable*" novel TADF materials as promising alternatives to phosphorescent materials. These studies were recently summarized in refs.[8, 9]. In contrast, few "*solution-processable*" TADF materials have been reported so far, and among those that are known, highly efficient emitters are especially rare [10-15]. In particular, solution-processable deep-blue emitters are urgently required to achieve high efficiency, excellent color reproducibility, and low energy consumption. However, there has been no report of solution-processed TADF OLEDs exceeding the theoretical limit of

external quantum efficiency (EQE) for normal fluorescence-based OLEDs (5.0–7.5%) with deep-blue emission color of y < 0.15 in Commission Internationale de l'Eclairage (CIE) coordinates, CIE (x, y), as far as we know.

As a representative TADF molecular framework, acridan and triazine have been well investigated, and several materials containing either or both of these fragments have shown efficient TADF in the case of vacuum-processed OLEDs [16-30]. We have reported that those containing acridan and triazine as electron donor and acceptor, respectively, (denoted the acridan-triazine system) exhibited high device performance with EQE of nearly 18% in their application to solution-processed OLEDs [12, 31]. Judging from these preceding studies, we speculate that the acridan-triazine system is promising for the development of solution-processable TADF materials. However, those molecules exhibit green to sky-blue emission, being far from deep-blue.

Organic molecules drastically change their properties in response to even slight structural modification. Here, we will show newly-developed, highly efficient, solution-processable, deep-blue TADF emitters with a subtle but crucial molecular alteration, adamantyl substitution, of the acridan-triazine molecular framework. This approach differs from conventional alkyl chain introduction. Adamantyl fragments have previously been introduced into organic molecular frameworks to enhance the thermal stability and solubility of materials [32-35], but here we also employ adamantyl groups as electron "donors," which potentially broaden the energy gap of the TADF material to realize deep-blue emission. In this study, we first clarify the requirements for designing efficient deep-blue TADF molecules, and second demonstrate the device performance of OLEDs consisting of the newly-designed TADF emitters based on our adamantyl substitution strategy. Our novel molecules exhibited maximum EQE (EQE_{MAX}) of 11.2% with CIE (0.15, 0.13) and EQE_{MAX} of 22.1% with CIE (0.15, 0.19) in their application to

solution-processed OLEDs. To our knowledge, those EQE_{MAX} values are the best yet for emission with $y < 0.15$ and $y < 0.20$ in CIE coordinates for solution-processed TADF-OLEDs.

3.2. Results and discussion

Although the higher states of excited singlet states (S_m) and triplet states (T_n), where m and n are integers greater than one, potentially participate in the TADF process, TADF is normally believed to occur via reverse intersystem crossing (RISC) from the lowest excited triplet (T_1) to lowest excited singlet state (S_1). The normally spin-forbidden RISC is allowed by spin mixing of S_1 and T_1, whose mixing coefficient is inversely proportional to the energy difference between these two states (ΔE_{ST}) [36], and thus, emitters with small ΔE_{ST} promisingly induce effective RISC. ΔE_{ST} depends largely on the spatial overlap between the initial (φ_i) and final (φ_f) wave functions during the electronic transition and therefore, the charge transfer (CT)-dominated S_1 (^{1}CT) and T_1 (^{3}CT) states result in a small $\Delta E_{ST} = E(^1\text{CT}) - E(^3\text{CT})$ value, where $E(^1\text{CT})$ and $E(^3\text{CT})$ denote the energy level of ^{1}CT and ^{3}CT, respectively. This being widely known, TADF materials are mainly composed of electron donor (D) and acceptor (A) moieties, i.e., D-A type molecules [8, 9]. However, when a locally excited (LE)-type triplet state (^{3}LE) (where a ππ*-like electronic transition on the D or A fragment is dominant) lies lower in energy than ^{3}CT of D-A compounds, T_1 of the molecules is formed not by ^{3}CT but ^{3}LE [37, 38]. This results in larger $\Delta E_{ST} = E(^1\text{CT}) - E(^3\text{LE})$ (Figure 3.1a) compared with molecules whose ^{3}CT dominates T_1 ($E(^1\text{CT}) - E(^3\text{CT})$, Figure 3.1b), even when the energy difference between ^{1}CT and ^{3}CT [$E(^1\text{CT}) - E(^3\text{CT})$] is small.

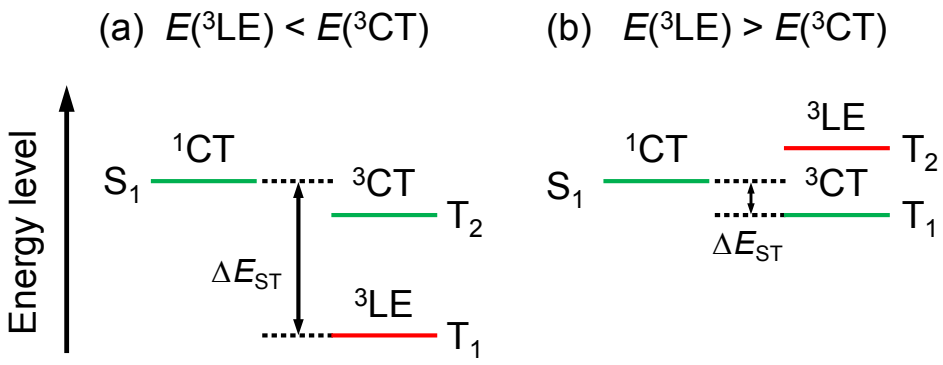

Figure 3.1. Schematic energy diagrams for excited states in the case of (a) $E(^3\text{LE}) < E(^3\text{CT})$ and (b) $E(^3\text{LE}) > E(^3\text{CT})$.

Combining all the above-mentioned considerations, there are four requirements for energy levels in molecular design to achieve efficient D-A-type deep-blue TADF: (i) deep highest occupied molecular orbital (HOMO) energy level for the D segment, (ii) shallow lowest unoccupied molecular orbital (LUMO) energy level for the A segment, (iii) proper HOMO and LUMO energy level arrangement of donor and acceptor to realize CT emission (shallower HOMO of D than that of A and deeper LUMO of A than that of D), and (iv) $E(^3\mathrm{LE})$ of both D and A segments higher than $E(^3\mathrm{CT})$.

We demonstrate our adamantyl substitution strategy as follows. The right side of Table 3.1 summarizes the chemical structures of the acceptor fragments, containing triazine cores, in this study, and their HOMO, LUMO and T_1 energy levels, calculated by density functional theory (DFT) and time-dependent DFT (TD-DFT) at the PBE0/6-31G(d) level of theory using Gaussian 09 [39]. Our strategy is to introduce adamantyl substituents to the 4th and 6th positions of 2-phenyl-1,3,5-triazine, the resulting compound being named TA. First, we compare TA with 2,4,6-triphenyl-1,3,5-triazine, TRZ. The LUMO energy level of TA (−1.45 eV) lies 0.26 eV higher than that of TRZ (−1.71 eV). The T_1 energy level of TA (3.14 eV) is 0.19 eV higher than that of TRZ (2.95 eV). This is because the aromatic phenyl moieties in TRZ conjugate with the 2-phenyl-1,3,5-triazine core (colored in blue in Table 3.1), which induces a drop of both triplet and LUMO energy, while the aliphatic adamantyl fragments of TA do not. To discuss the effect of adamantyl fragments in more detail, let us compare TA with the corresponding hydrogen-substituted molecule, TH, lacking adamantyl substituents (see the rightmost column in Table 3.1). The triplet energy of TA (3.14 eV) is comparable to, or rather, slightly higher than that of TH (3.08 eV). More significantly, the LUMO energy of TA (−1.45 eV) is much shallower than that of TH (−1.79 eV). This indicates that adamantyl fragments act as effective electron-“donating” substituents to “weaken” the electron-accepting property of the

molecule, which pushes up the LUMO energy level.

Table 3.1. Chemical structures of donor and acceptor materials, and their HOMO, LUMO, and T_1 energy levels calculated by DFT and TD-DFT at the PBE0/6-31G(d) level of theory using Gaussian 09.

	Donor			Acceptor		
	MA	FA	PA	TRZ	TA	TH
Chemical structure	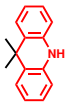	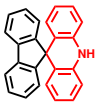	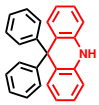	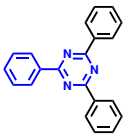	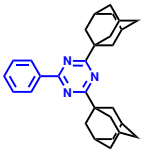	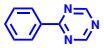
T_1 / eV	3.11	2.94	3.29	2.95	3.14	3.08
LUMO / eV	0.07	−0.66	−0.19	−1.71	−1.45	−1.79
HOMO / eV	−5.12	−5.29	−5.39	−6.96	−6.93	−7.17

The left side of Table 3.1 shows the donor fragments, containing acridan cores (colored in red), and their calculated HOMO, LUMO and T_1 energies. As an example, let us consider the combination of FA and TA in terms of the four energy level requirements for deep-blue TADF mentioned above. As shown in Table 3.1, the HOMO of FA (−5.29 eV) is deeper than that of MA (−5.12 eV) (requirement (i)) and the LUMO of TA (−1.45 eV) is shallower than that of TRZ (−1.71 eV) (requirement (ii)). The HOMO of FA (−5.29 eV) lies shallower than that of TA (−6.93 eV) and the LUMO of TA (−1.45 eV) deeper than that of FA (−0.66 eV) (requirement (iii), see also Figure 3.2a). Figure 3.2b exhibits the molecular structures of FA, TA and FA-TA and their excited energy levels together with their natural transition orbitals (NTOs), which visualize an electronic transition from the ground state (S_0) to S_m or T_n, using the optimized S_0 geometries. Both S_1 and T_1 of FA-TA are dominated by CT transition between FA and TA moieties, resulting in small ΔE_{ST} (the calculated value is 13 meV). CT dominates this T_1 formation because of the sufficiently high ^{3}LE energy of FA-TA (Figure 3.2b), which derives from the high T_1 energies of both FA and TA fragments; T_2, T_3 and T_4 of FA-TA are all of LE type, and originate from T_1 of FA, T_1 of TA and T_2 of FA, respectively (requirement (iv)). MA-TA and PA-TA also exhibit the same trends and their calculated results are summarized in Supplementary Figure 3.2. In summary, all the compounds containing adamantyl groups shown here, MA-TA, FA-TA, and PA-TA, fulfill all the above requirements, and therefore meet the molecular design concept for deep-blue TADF emitters.

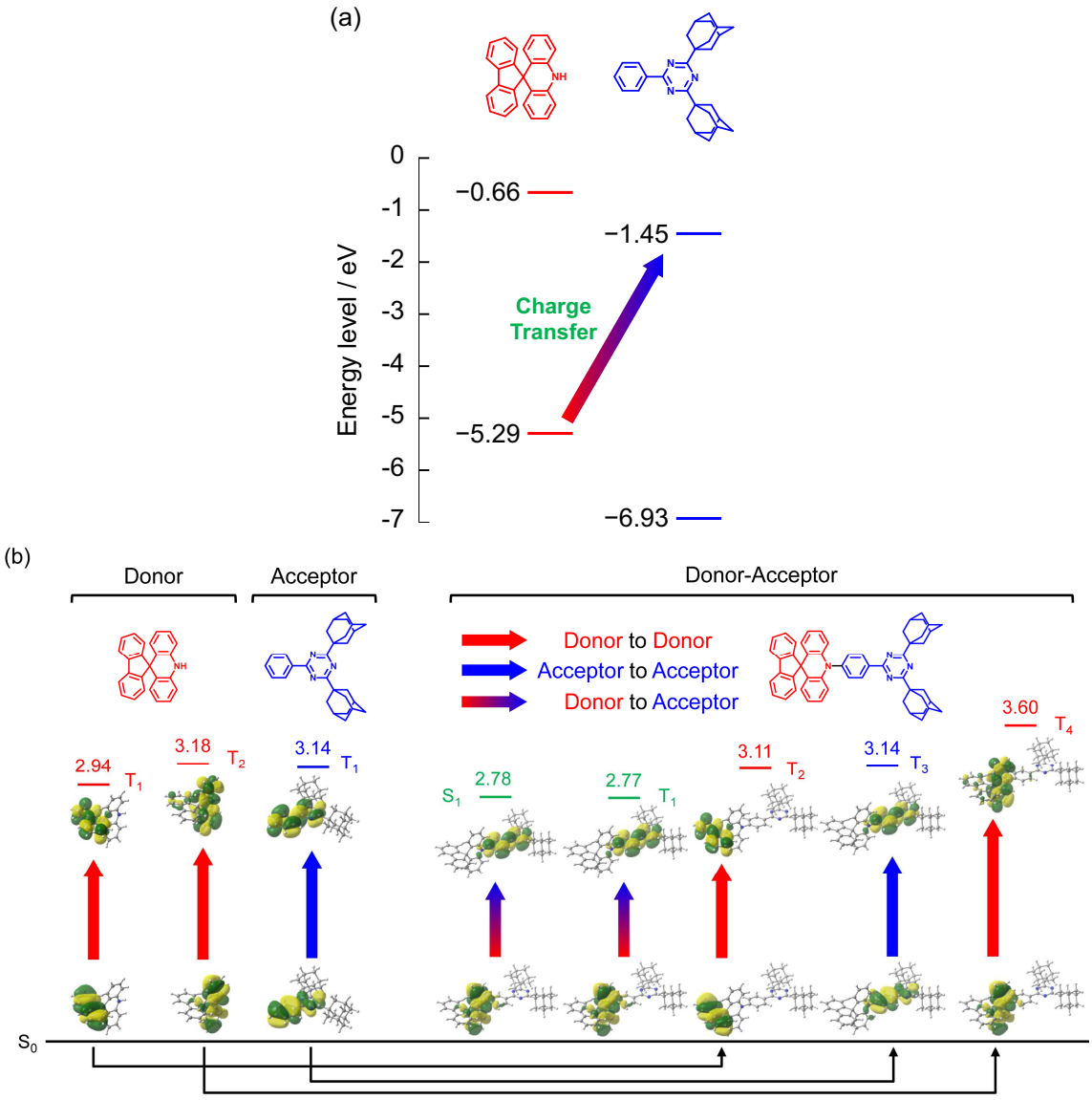

Figure 3.2. (a) HOMO and LUMO energy levels of FA and TA. (b) NTOs of each excited state. The electronic transitions are classified into three types using bold arrows: donor to donor (red), acceptor to acceptor (blue), and donor to acceptor (from red to blue).

The synthetic procedures and characterizations of MA-TA, FA-TA and PA-TA are detailed in Supplementary Information. After their synthesis, all the materials were purified through train sublimation. To assess the feasibility of solution processing, the solubilities of these emitters were examined. PA-TRZ (the combination of PA and TRZ in Table 3.1, see also Supplementary Figure 3.1), which consists of the same fragments as PA-TA but with phenyl instead of adamantyl groups, is reported to be less soluble in common solvents [25]; the low solubility of PA-TRZ hinders the measurement of ^{13}C NMR spectra even in chloroform solution, which might cause difficulty in thin film fabrication when PA-TRZ is applied to solution-processed OLEDs. In sharp contrast, the materials designed herein, MA-TA, FA-TA and PA-TA, were found to be easily dissolved in chloroform at concentrations of over 10 mg mL^{-1}, being high enough to form a thin film for OLEDs. As shown in Supplementary Information, clear ^{13}C NMR spectra were obtained for these materials. The difference between the chemical structures of PA-TA and PA-TRZ is the presence of adamantly segments, rather than phenyl, which improves its solubility. The thermal stability of the emitters was determined by measurement of their glass transition temperatures (T_g) and decomposition temperatures (T_d) (Table 3.2). T_g of MA-TA, 147 °C, is much higher than that of MA-TRZ (the combination of MA and TRZ in Table 3.1, see also Supplementary Figure 3.1), 91 °C [21]. FA-TA and PA-TA showed even higher T_g of 207 and 186 °C, respectively. T_d of MA-TA, FA-TA and PA-TA are 423, 480 and 468 °C, respectively, which are also higher than that of MA-TRZ (305 °C). This high thermal stability is again attributed to adamantyl substitution. The sublimation temperatures (T_{sub}) were also measured by thermogravimetric analysis (TGA) under vacuum. The T_{sub} of MA-TA, FA-TA and PA-TA (317, 372 and 362 °C) were about 100 °C lower than the T_d of respective materials, which ensures the sublimability of these materials. The detailed experimental data of thermal properties are shown in Supplementary Figure 3.3 and 3.4.

Table 3.2. Thermal properties, photophysical properties, and device performances of three emitters, MA-TA, FA-TA, and PA-TA.

	MA-TA	FA-TA	PA-TA
T_g [a)]	147	207	186
T_d [b)]	428	480	468
E_g / eV [c)]	2.90	2.95	3.01
HOMO / eV [d)]	−5.86	−5.91	−6.00
LUMO / eV [e)]	−2.96	−2.96	−2.99
Φ_{PL} [f)]	0.83 (0.99)[g)]	0.76	0.70
Φ_p [h)]	0.48	0.34	0.28
Φ_d [h)]	0.35	0.42	0.42
τ_1 / ns	14.4	12.0	10.6
τ_2 / μs	4.3	8.2	12.1
τ_3 / μs	23.3	54.9	88.4
EQE_{MAX} (%)	22.1	11.2	6.7
CIE (x, y)	(0.15, 0.19)	(0.15, 0.13)	(0.15, 0.10)

Determined from [a)] onset of DSC curve, [b)] 5% weight loss of TGA curve, [c)] intersection of tangents of absorption spectra and PL spectra in toluene solution (red dotted lines in Figure 3.3a), [d)] onset of photoelectron spectroscopy in air (Supplementary Figure 3.5), and [e)] the equation LUMO = HOMO + E_g; [f)] 10 wt% Emitter:CzSi film with excited wavelength of 280 nm; [g)] 10 wt% MA-TA:CzSi drop-cast film with excited wavelength of 360 nm, where MA-TA is directly excited; [h)] Calculated from integrated intensity of prompt (Φ_p) and delayed (Φ_d) emission of PL decay curve. Refer to Supplementary Table 3.2.

Photophysical experiments were also performed, as summarized in Table 3.2. The UV-vis absorption and photoluminescence (PL) spectra of the emitters in 10^{-5} M toluene solution and PL spectra of the neat films are shown in Figure 3.3a. The films were spin-coated on quartz substrates from chloroform solution at the concentration of 10 mg mL^{-1}. In toluene solution, all three emitters showed broad single-peaked spectra without vibrational structures. The emission peak maximum (λ_{MAX}) was observed at 451 nm for PA-TA, which is the deepest blue emission among the three emitters (FA-TA had λ_{MAX} at 454 nm and MA-TA had λ_{MAX} at 469 nm). Surprisingly, the λ_{MAX} of their neat films were blue-shifted to 446 (PA-TA), 452 (FA-TA) and 453 nm (MA-TA), the opposite tendency to that of ordinary emitter materials [21, 40-42]. The reason for these blue-shifts is now under investigation, but the mechanism might involve adamantyl substitution. As will be discussed in the Conclusion, this finding is important for developing host-free TADF OLEDs.

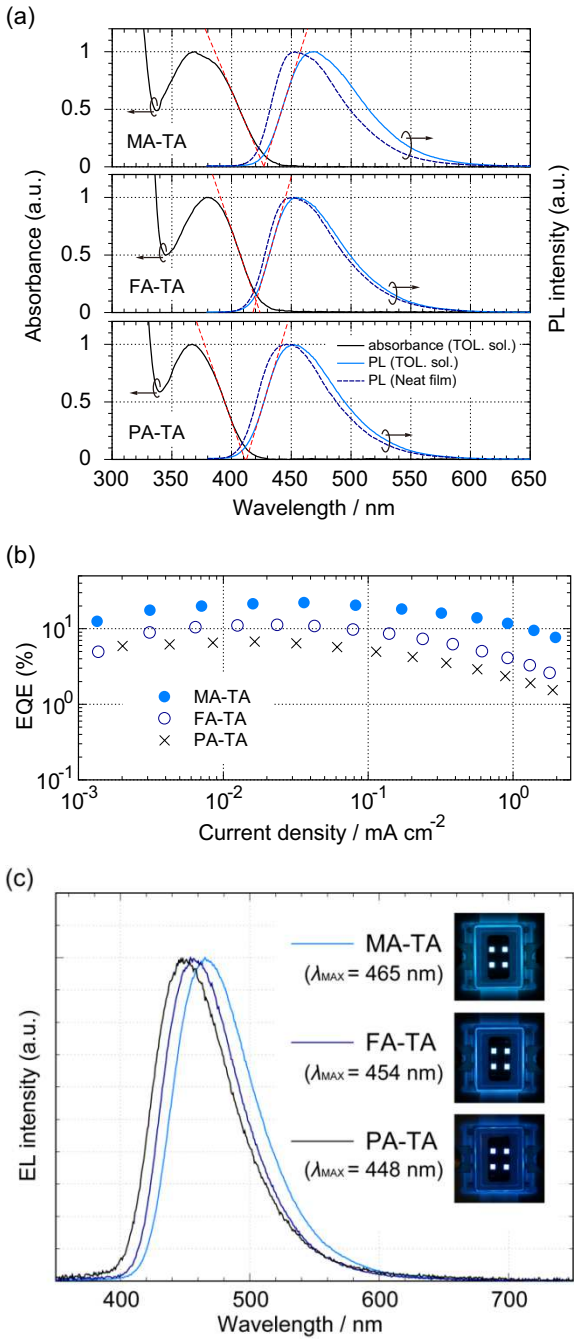

Figure 3.3. (a) UV-vis and PL spectra in 10^{-5} M toluene (Tol.) solution and PL spectra of neat film for MA-TA (top), FA-TA (middle) and PA-TA (bottom). (b) EQE–current density characteristics and (c) EL spectra of solution-processed OLEDs using MA-TA, FA-TA, and PA-TA as emitters. The λ_{MAX} of each spectrum is specified in parenthesis. Photographs of the OLEDs are also shown in (c).

To maximize the efficiency of deep-blue emission in OLEDs, we investigated a range of host materials and doping concentrations. The candidate hosts were 9,9′-(2,2′-dimethyl-[1,1′-biphenyl]-4,4′-diyl)bis(9*H*-carbazole) (CDBP), 1,3-bis(9,9-dimethylacridin-10(9*H*)-yl)benzene (mAP), 9-(4-(*tert*-butyl)phenyl)-3,6-bis(triphenylsilyl)-9*H*-carbazole (CzSi), dibenzo[*b*,*d*]furan-2,8-diylbis(diphenylphosphine oxide) (PPF), and diphenyl[4-(triphenylsilyl)phenyl]phosphine oxide (TSPO1), which are widely used to confine the triplet energy of blue TADF and phosphorescent emitters. Their triplet energies are reported to be 3.0 eV (CDBP [43], mAP [44], and CzSi [45]), 3.1 eV (PPF [46]) and 3.4 eV (TSPO1 [47]) and their molecular structures are shown in Supplementary Figure 3.1. Table 3.3 summarizes the effect of these hosts on the PL quantum yield, Φ_{PL}, and CIE coordinates of 10 wt% FA-TA:Host films. FA-TA exhibited deep-blue emission with CIE coordinates of (0.15, 0.13) in CDBP, mAP, and CzSi hosts. Among those three, the highest Φ_{PL} of 0.76 was obtained in CzSi. FA-TA exhibited higher Φ_{PL} in TSPO1 and PPF than in the other hosts, but the CIE y values were larger. For CzSi and PPF host matrices, we conducted further investigations on the doping concentration dependence, as summarized in Table 3.4 and Supplementary Figure 3.6. The Φ_{PL} in PPF host were nearly constant at around 0.85 across a wide doping concentration range from 10 wt% to 50 wt%, and remained as high as 0.71 even at 80 wt%. However, the PPF matrix is unsuitable for realizing deep-blue OLEDs as the CIE y values were larger than 0.2 at doping concentrations between 10 and 80 wt%. In the CzSi host, Φ_{PL} gradually dropped from 0.76 to 0.63 as the doping concentration increased from 10 wt% to 50 wt%, but values of $y \leq 0.16$ in CIE coordinates were preserved across a wide range of doping concentrations.

Table 3.3. Φ_{PL} and CIE coordinates of 10 wt% FA-TA:Host films.

Host	Φ_{PL} [a)]	CIE (x, y)
CDBP	0.36[b)] (0.32)	$(0.15_5, 0.13_1)$[b)]
mAP	0.67[c)] (0.38)	$(0.15_4, 0.13_8)$[c)]
CzSi	0.76[d)] (0.36)	$(0.15_3, 0.13_3)$[d)]
TSPO1	0.84[e)] (0.57)	$(0.16_0, 0.18_3)$[e)]
PPF	0.86[d)] (0.67)	$(0.16_3, 0.21_6)$[d)]

[a)] Φ_{PL} measured in the air is shown in parentheses; Excited at [b)] 297 nm, [c)] 287 nm, [d)] 280 nm, and [e)] 273 nm.

Table 3.4. Photophysical properties of *X* wt%FA-TA:Host films. Excitation wavelengths are 280 and 383 nm for doped and neat films, respectively.

	Host			
	PPF		CzSi	
Dopant conc. *X* / wt%	Φ_{PL}	CIE (x, y)	Φ_{PL}	CIE (x, y)
10	0.86 (0.67)[a)]	$(0.16_3, 0.21_6)$	0.76 (0.36)[a)]	$(0.15_3, 0.13_3)$
20	0.85 (0.66)[a)]	$(0.16_6, 0.24_1)$	—	—
30	—	—	0.72 (0.35)[a)]	$(0.15_3, 0.15_1)$
50	0.85 (0.57)[a)]	$(0.16_9, 0.26_1)$	0.63 (0.33)[a)]	$(0.15_4, 0.15_9)$
80	0.71 (0.42)[a)]	$(0.16_5, 0.23_5)$	—	—
100 (= neat film)	0.46 (0.33)[a)]	$(0.16_0, 0.13_3)$[b)]	0.46 (0.33)[a)]	$(0.16_0, 0.13_3)$[b)]

[a)] Measured in air; [b)] Excited at 383 nm.

On the basis of the above investigations, an emitter doping concentration of 10 wt% in CzSi host matrix was judged to be suitable for realizing efficient deep-blue OLEDs. A transient PL study of the 10 wt% Emitters:CzSi films was then conducted. At 300 K, the films showed short (commonly termed "prompt") and long-tailed (commonly termed "delayed") components and could be well fitted with three exponential curves. Their lifetimes τ_1 / τ_2 / τ_3 were 14.4 ns / 4.3 μs / 23.3 μs for MA-TA, 12.0 ns / 8.2 μs / 54.9 μs for FA-TA and 10.6 ns / 12.1 μs / 88.4 μs for PA-TA. PL decay curves were also measured at every 20 K from 200 K to 300 K and the relative intensity of the delayed component increased with increasing temperature, which is characteristic TADF behavior (Supplementary Figure 3.7). Here, we used Zhang's methods [48, 49] to determine ΔE_{ST}: the longest two lifetimes are averaged and the average lifetime, τ_d, is used for calculations of ΔE_{ST}. τ_d of 18.3, 44.4, and 69.5 μs were obtained for MA-TA, FA-TA, and PA-TA, respectively, leading to ΔE_{ST} of 0.14, 0.16, and 0.17 eV. Detailed fitting parameters are shown in Supplementary Information.

Finally, we fabricated highly efficient OLEDs, with blue to deep-blue emissions, using solution-processable TADF materials designed by our new strategy. The device architecture was indium tin oxide (ITO) (50 nm)/poly(3,4-ethylenedioxythiophene)–poly(styrenesulfonate) (PEDOT:PSS) (45 nm)/poly(9-vinylcarbazole) (PVK) (15 nm)/10 wt% Emitter:CzSi (35 nm)/TSPO1 (5 nm)/1,3,5-tris(1-phenyl-1*H*-benzo[*d*]imidazol-2-yl)benzene (TPBi) (50 nm)/lithium quinolin-8-olate (Liq) (1 nm)/Al (80 nm). PVK was used to facilitate hole injection from PEDOT:PSS to the emitting layer and to suppress electron leakage from the emitting layer to PEDOT:PSS. TSPO1 was adopted both as a hole- and exciton-blocking layer from the emitting layer to the electron-transporting layer. More details on the device fabrication are provided in Supplementary Information. MA-TA, FA-TA and PA-TA showed EQE_{MAX} / CIE (x,y) of 22.1% / (0.15 0.19), 11.2% / (0.15, 0.13) and 6.7% / (0.15, 0.10), respectively, as shown

in Figure 3.3.

3.3. Conclusion

In conclusion, we have developed solution-processable deep-blue TADF materials, MA-TA, FA-TA and PA-TA, based on an adamantyl substitution strategy. These TADF emitters, containing adamantyl fragments, showed high solubility and high thermal stability, with T_g of 147, 207 and 186 °C. In their application to solution-processed OLEDs, EQE_{MAX} of 11.2% with CIE(0.15, 0.13) and EQE_{MAX} of 22.1% with CIE(0.15, 0.19) were achieved using FA-TA and MA-TA for the dopant, respectively. These efficiencies are the best yet among solution-processed TADF OLEDs for $y < 0.15$ and $y < 0.20$, respectively, as far as we know. Previously, adamantyl substituents have been employed to ensure thermal stability and solubility. In addition to these advantages, our adamantyl substitution strategy in this study clearly reveals that the substitution plays a crucial role for the realization of deep-blue emission. As we have demonstrated, however, some challenges remain regarding host choice. Investigation of potential new hosts is an ongoing activity, especially for deep-blue emitters, to make full use of the excitons generated in OLEDs. Host-free OLEDs (also known as non-doped OLEDs), where the emitting layer consists only of an emitter material, potentially solve the problem, but the realization of host-free deep-blue emitters faces two severe challenges: concentration quenching and spectrum red-shifting in their neat films. While some TADF emitters free of concentration quenching have recently been reported by several groups [21, 25, 40, 50], the red-shift problem remains unsolved. Our TADF emitters surprisingly suppress red-shifting in their neat films relative to their doped films, as seen in Table 3.3 and 3.4, which is in contrast to ordinary emitters. We believe that this promising phenomenon will yield insights into the realization of deep-blue host-free OLEDs.

(Chapter 3 is the unedited Author's version of a Submitted Work that was subsequently accepted

3.4. References

[1] L. Duan, L. Hou, T.-W. Lee, J. Qiao, D. Zhang, G. Dong, L. Wang and Y. Qiu, *J. Mater. Chem.* **2010**, *20*, 6392.

[2] X. Xu, X. Yang, J. Zhao, G. Zhou and W.-Y. Wong, *Asian J. Org. Chem.* **2015**, *4*, 394.

[3] T.-H. Han, M.-R. Choi, C.-W. Jeon, Y.-H. Kim, S.-K. Kwon and T.-W. Lee, *Sci. Adv.* **2016**, *2*, e1601428.

[4] F. K.-W. Kong, M.-C. Tang, Y.-C. Wong, M. Ng, M.-Y. Chan and V. W.-W. Yam, *J. Am. Chem. Soc.* **2017**, *139*, 6351.

[5] G. Sarada, W. Cho, A. Maheshwaran, V. G. Sree, H.-Y. Park, Y.-S. Gal, M. Song and S.-H. Jin, *Adv. Funct. Mater.* **2017**, *27*, 1701002.

[6] M.-C. Tang, C.-H. Lee, S.-L. Lai, M. Ng, M.-Y. Chan and V. W.-W. Yam, *J. Am. Chem. Soc.* **2017**, *139*, 9341.

[7] H. Uoyama, K. Goushi, K. Shizu, H. Nomura and C. Adachi, *Nature* **2012**, *492*, 234.

[8] Z. Yang, Z. Mao, Z. Xie, Y. Zhang, S. Liu, J. Zhao, J. Xu, Z. Chi and M. P. Aldred, *Chem. Soc. Rev.* **2017**, *46*, 915.

[9] M. Y. Wong and E. Zysman-Colman, *Adv. Mater.* **2017**, *29*, 1605444.

[10] Y. J. Cho, K. S. Yook and J. Y. Lee, *Adv. Mater.* **2014**, *26*, 6642.

[11] Y. J. Cho, B. D. Chin, S. K. Jeon and J. Y. Lee, *Adv. Funct. Mater.* **2015**, *25*, 6786.

[12] Y. Wada, K. Shizu, S. Kubo, K. Suzuki, H. Tanaka, C. Adachi and H. Kaji, *Appl. Phys. Lett.* **2015**, *107*, 183303.

[13] J. Luo, S. Gong, Y. Gu, T. Chen, Y. Li, C. Zhong, G. Xie and C. Yang, *J. Mater. Chem. C* **2016**, *4*, 2442.

[14] Y. J. Cho, S. K. Jeon and J. Y. Lee, *Adv. Opt. Mater.* **2016**, *4*, 688.

[15] G. Xie, X. Li, D. Chen, Z. Wang, X. Cai, D. Chen, Y. Li, K. Liu, Y. Cao and S.-J. Su, *Adv.*

Mater. **2016**, *28*, 181.

[16] S. Hirata, Y. Sakai, K. Masui, H. Tanaka, S. Y. Lee, H. Nomura, N. Nakamura, M. Yasumatsu, H. Nakanotani, Q. Zhang, K. Shizu, H. Miyazaki and C. Adachi, *Nat. Mater.* **2015**, *14*, 330.

[17] K. Shizu, J. Lee, H. Tanaka, H. Nomura, T. Yasuda, H. Kaji and C. Adachi, *Pure Appl. Chem.* **2015**, *87*, 627.

[18] H. Kaji, H. Suzuki, T. Fukushima, K. Shizu, K. Suzuki, S. Kubo, T. Komino, H. Oiwa, F. Suzuki, A. Wakamiya, Y. Murata and C. Adachi, *Nat. Commun.* **2015**, *6*, 8476.

[19] J. W. Sun, J. Y. Baek, K.-H. Kim, C.-K. Moon, J.-H. Lee, S.-K. Kwon, Y.-H. Kim and J.-J. Kim, *Chem. Mater.* **2015**, *27*, 6675.

[20] M. Numata, T. Yasuda and C. Adachi, *Chem. Commun.* **2015**, *51*, 9443.

[21] W.-L. Tsai, M.-H. Huang, W.-K. Lee, Y.-J. Hsu, K.-C. Pan, Y.-H. Huang, H.-C. Ting, M. Sarma, Y.-Y. Ho, H.-C. Hu, C.-C. Chen, M.-T. Lee, K.-T. Wong and C.-C. Wu, *Chem. Commun.* **2015**, *51*, 13662.

[22] M. Kim, S. K. Jeon, S.-H. Hwang, S.-S. Lee, E. Yu and J. Y. Lee, *J. Phys. Chem. C* **2016**, *120*, 2485.

[23] I. S. Park, J. Lee and T. Yasuda, *J. Mater. Chem. C* **2016**, *4*, 7911.

[24] K.-C. Pan, S.-W. Li, Y.-Y. Ho, Y.-J. Shiu, W.-L. Tsai, M. Jiao, W.-K. Lee, C.-C. Wu, C.-L. Chung, T. Chatterjee, Y.-S. Li, K.-T. Wong, H.-C. Hu, C.-C. Chen and M.-T. Lee, *Adv. Funct. Mater.* **2016**, *26*, 7560.

[25] T.-A. Lin, T. Chatterjee, W.-L. Tsai, W.-K. Lee, M.-J. Wu, M. Jiao, K.-C. Pan, C.-L. Yi, C.-L. Chung, K.-T. Wong and C.-C. Wu, *Adv. Mater.* **2016**, *28*, 6976.

[26] K. Nakao, H. Sasabe, R. Komatsu, Y. Hayasaka, T. Ohsawa and J. Kido, *Adv. Opt. Mater.* **2017**, *5*, 1600843.

[27] R. Komatsu, T. Ohsawa, H. Sasabe, K. Nakao, Y. Hayasaka and J. Kido, *ACS Appl. Mater. Interfaces* **2017**, *9*, 4742.

[28] R. Komatsu, H. Sasabe, K. Nakao, Y. Hayasaka, T. Ohsawa and J. Kido, *Adv. Opt. Mater.* **2017**, *5*, 1600675.

[29] I. S. Park, H. Komiyama and T. Yasuda, *Chem. Sci.* **2017**, *8*, 953.

[30] L.-S. Cui, H. Nomura, Y. Geng, J. U. Kim, H. Nakanotani and C. Adachi, *Angew. Chem. Int. Ed.* **2017**, *56*, 1571.

[31] Y. Wada, K. Shizu, S. Kubo, T. Fukushima, T. Miwa, H. Tanaka, C. Adachi and H. Kaji, *Appl. Phys. Express* **2016**, *9*, 032102.

[32] C.-H. Chen, W.-J. Shen, K. Jakka and C.-F. Shu, *Synth. Met.* **2004**, *143*, 215.

[33] H. Fukagawa, N. Yokoyama, S. Irisa and S. Tokito, *Adv. Mater.* **2010**, *22*, 4775.

[34] Y. Gu, L. Zhu, Y. Li, L. Yu, K. Wu, T. Chen, M. Huang, F. Wang, S. Gong, D. Ma, J. Qin and C. Yang, *Chem. Eur. J.* **2015**, *21*, 8250.

[35] A. Kovalenko, C. Yumusak, P. Heinrichova, S. Stritesky, L. Fekete, M. Vala, M. Weiter, N. S. Sariciftci and J. Krajcovic, *J. Mater. Chem. C* **2017**, *5*, 4716.

[36] N. J. Turro, V. Ramamurthy and J. C. Scaiano, University Science Books, Sausalito, California, USA, **2010**.

[37] Q. Zhang, J. Li, K. Shizu, S. Huang, S. Hirata, H. Miyazaki and C. Adachi, *J. Am. Chem. Soc.* **2012**, *134*, 14706.

[38] D. D. Zhang, L. A. Duan, Y. L. Li, D. Q. Zhang and Y. Qiu, *J. Mater. Chem. C* **2014**, *2*, 8191.

[39] M. J. Frisch, G. W. Trucks, H. B. Schlegel, G. E. Scuseria, M. A. Robb, J. R. Cheeseman, G. Scalmani, V. Barone, B. Mennucci, G. A. Petersson, H. Nakatsuji, M. Caricato, X. Li, H. P. Hratchian, A. F. Izmaylov, J. Bloino, G. Zheng, J. L. Sonnenberg, M. Hada, M. Ehara, K. Toyota,

R. Fukuda, J. Hasegawa, M. Ishida, T. Nakajima, Y. Honda, O. Kitao, H. Nakai, T. Vreven, J. A. Montgomery, Jr., J. E. Peralta, F. Ogliaro, M. Bearpark, J. J. Heyd, E. Brothers, K. N. Kudin, V. N. Staroverov, T. Keith, R. Kobayashi, J. Normand, K. Raghavachari, A. Rendell, J. C. Burant, S. S. Iyengar, J. Tomasi, M. Cossi, N. Rega, J. M. Millam, M. Klene, J. E. Knox, J. B. Cross, V. Bakken, C. Adamo, J. Jaramillo, R. Gomperts, R. E. Stratmann, O. Yazyev, A. J. Austin, R. Cammi, C. Pomelli, J. W. Ochterski, R. L. Martin, K. Morokuma, V. G. Zakrzewski, G. A. Voth, P. Salvador, J. J. Dannenberg, S. Dapprich, A. D. Daniels, O. Farkas, J. B. Foresman, J. V. Ortiz, J. Cioslowski and D. J. Fox, Revision E.01 ed., Gaussian, Inc., Wallingford CT, **2009**.

[40] Q. Zhang, D. Tsang, H. Kuwabara, Y. Hatae, B. Li, T. Takahashi, S. Y. Lee, T. Yasuda and C. Adachi, *Adv. Mater.* **2015**, *27*, 2096.

[41] K. Albrecht, K. Matsuoka, K. Fujita and K. Yamamoto, *Angew. Chem. Int. Ed.* **2015**, *54*, 5677.

[42] K. Matsuoka, K. Albrecht, K. Yamamoto and K. Fujita, *Sci. Rep.* **2017**, *7*, 41780.

[43] P. Schrögel, A. Tomkevičienė, P. Strohriegl, S. T. Hoffmann, A. Köhler and C. Lennartz, *J. Mater. Chem.* **2011**, *21*, 2266.

[44] J.-A. Seo, M. S. Gong, S. K. Jeon, J. Y. Lee, C. H. Noh and S. H. Kim, *Dyes and Pigments* **2015**, *123*, 254.

[45] M.-H. Tsai, H.-W. Lin, H.-C. Su, T.-H. Ke, C.-C. Wu, F.-C. Fang, Y.-L. Liao, K.-T. Wong and C.-I. Wu, *Adv. Mater.* **2006**, *18*, 1216.

[46] P. A. Vecchi, A. B. Padmaperuma, H. Qiao, L. S. Sapochak and P. E. Burrows, *Org. Lett.* **2006**, *8*, 4211.

[47] S. O. Jeon, S. E. Jang, H. S. Son and J. Y. Lee, *Adv. Mater.* **2011**, *23*, 1436.

[48] Q. Zhang, H. Kuwabara, W. J. Potscavage, Jr., S. Huang, Y. Hatae, T. Shibata and C. Adachi, *J. Am. Chem. Soc.* **2014**, *136*, 18070.

[49] Q. S. Zhang, B. Li, S. P. Huang, H. Nomura, H. Tanaka and C. Adachi, *Nat. Photon.* **2014**, *8*, 326.

[50] J. Lee, N. Aizawa, M. Numata, C. Adachi and T. Yasuda, *Adv. Mater.* **2017**, *29*, 1604856.

3.5. Supplementary Information

Chemical structure of the materials described in the main text

PA-TRZ 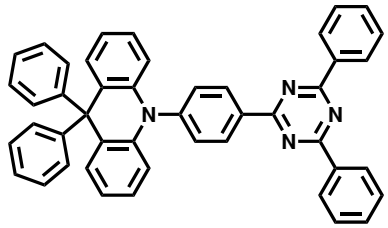

MA-TRZ 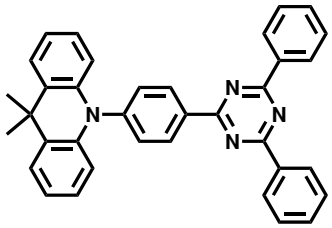

CDBP 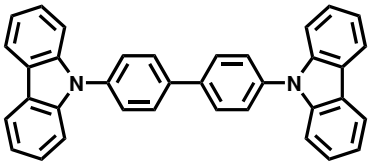

mAP 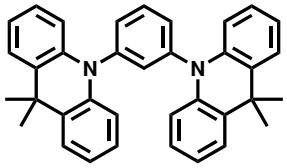

PPF 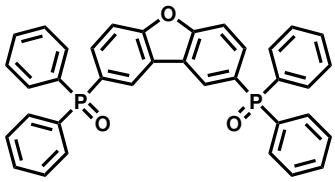

TSPO1 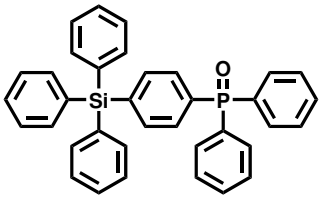

CzSi 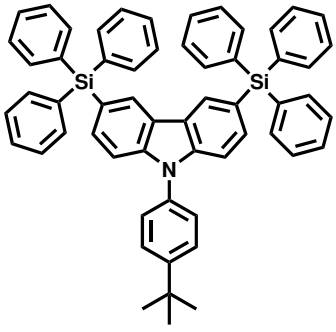

TPBi 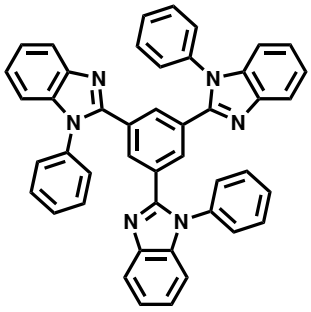

Liq 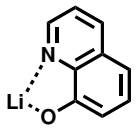

PVK 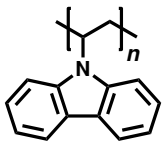

Supplementary Figure 3.1. Chemical structures of the materials described in the main text.

DFT and TD-DFT calculation results of the emitters

Supplementary Table 3.1. The energies of the highest occupied molecular orbital (HOMO), lowest unoccupied molecular orbital (LUMO), lowest excited triplet state (T_1), lowest excited singlet (S_1) state and their gap ($\Delta E_{ST} = S_1 - T_1$) are calculated using the PBE0/6-31G(d) level of theory. The optimized S_0 geometries are used for calculating Franck–Condon excitations (S_0-FC). The oscillator strength (*f*) of the electronic transition between the ground state (S_0) and S_1 is also listed. T_1, S_1, ΔE_{ST} and *f* calculated using the optimized structure of the excited states are also listed.

	HOMO / eV	LUMO / eV	**S_0-FC**				**Excited states opt.**			
			T_1 / eV	S_1 / eV	ΔE_{ST} / meV	*f*	T_1 / eV	S_1 / eV	ΔE_{ST} / meV	*f*
MA-TA	−5.12	−1.69	2.69	2.70	**11**	0	2.41	2.48	**72**	0
FA-TA	−5.20	−1.68	2.77	2.78	**13**	0.0007	2.46	2.55	**94**	0.0001
PA-TA	−5.32	−1.67	2.87	2.93	**55**	0.015	2.50	2.63	**124**	0.0002

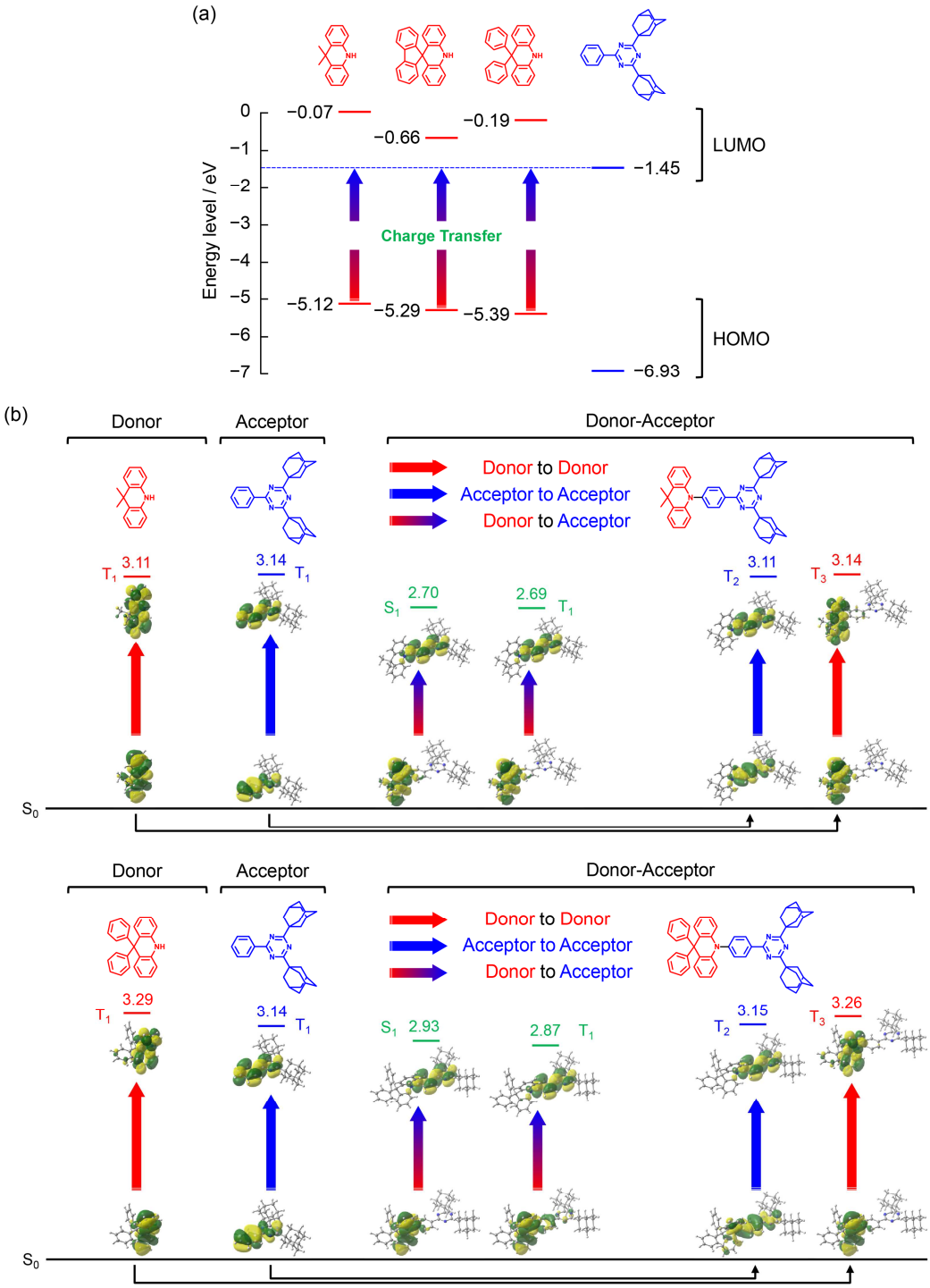

Supplementary Figure 3.2. (a) HOMO and LUMO energy levels of the donor and acceptor fragments. (b) NTOs of each excited state using the optimized ground state geometry for MA-TA (top) and PA-TA (bottom). Red and blue lines indicate that the electronic transition mainly takes place on donor and acceptor fragments, respectively.

Material synthesis and characterization

General procedure for material characterization

^{1}H and ^{13}C NMR spectra were recorded with a JEOL ECA-600 spectrometer (600 MHz for ^{1}H) or Bruker Avance-III (800 MHz for ^{1}H and 201 MHz for ^{13}C). Chemical shifts are reported in δ ppm, using residual protons in deuterated solvents for ^{1}H NMR experiments and solvent peaks for ^{13}C NMR spectra as internal standards. Atmospheric pressure chemical ionization (APCI) mass spectra were measured with a Bruker micrOTOF-Q II (Bruker, Germany). Elemental analysis was conducted by a CHN analyzer, MICRO CORDER JM10 (J-Science Lab Co., Ltd., Japan).

Synthesis of 2,4-di(adamantan-1-yl)-6-(4-bromophenyl)-1,3,5-triazine:

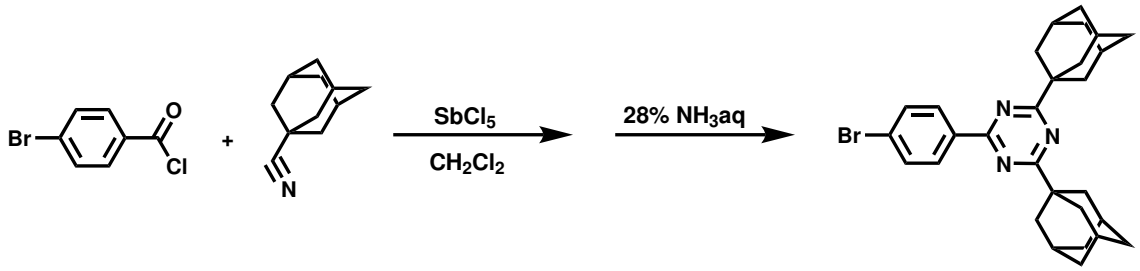

4-Bromobenzoyl chloride (1.72 g, 7.84 mmol) and 1-adamantanecarbonitrile (2.50 g, 15.5 mmol) were dissolved in 10 mL of super-dehydrated CH_2Cl_2 under Ar atmosphere, and stirred for 30 minutes at 0–5 °C in an ice-bath. Antimony(V) chloride solution (1.0 M in methylene chloride) (8.5 mL, 8.5 mmol) was added dropwise into the above solution and slowly warmed up to room temperature. The reaction mixture was continuously stirred for 1 hour at room temperature and refluxed at 45 °C for 38 hours. After the mixture was cooled to room temperature, a greenish white solid was filtrated and washed with CH_2Cl_2. The solid was added slowly to 55 mL of cooled 28% ammonia solution (0–5 °C) and stirred for 30 minutes in an ice-bath. The mixture was warmed up to room temperature and stirred for 16.5 hours. A white solid was filtrated and washed with distilled water. After drying, the solid was dissolved in toluene and hot filtration was conducted twice. After the filtrate was evaporated, the solid was washed with a small amount of acetone, and 1.10 g (2.18 mmol, yield: 28.1%) of pure 2,4-di(adamantan-1-yl)-6-(4-bromophenyl)-1,3,5-triazine was obtained as a white solid.

Material Characterization

2,4-Di(adamantan-1-yl)-6-(4-bromophenyl)-1,3,5-triazine: ^{1}H NMR (600 MHz, $CDCl_3$, δ): 8.47 (d, J = 8.2 Hz, 2H), 7.62 (d, J = 8.2 Hz, 2H), 2.08–2.13 (m, 18H), 1.79–1.84 (m, 12H).

Synthesis of MA-TA, FA-TA and PA-TA:

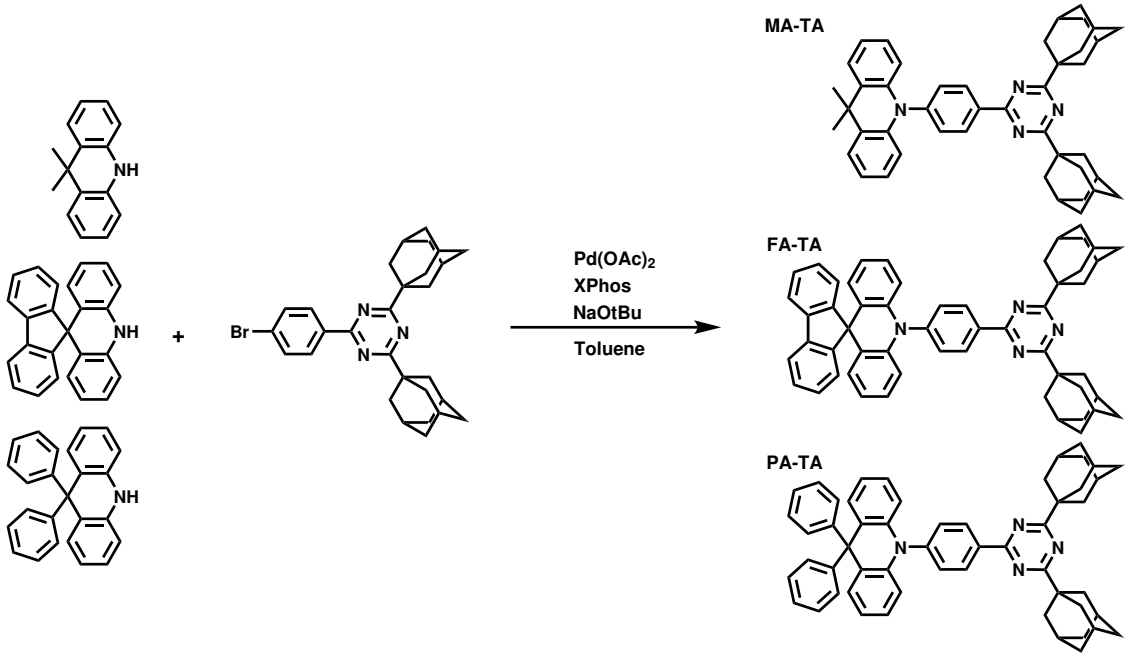

MA-TA: 9,9-Dimethyl-9,10-dihydroacridine (211 mg, 1.01 mmol), 2,4-di(adamantan-1-yl)-6-(4-bromophenyl)-1,3,5-triazine (456 mg, 0.90 mmol), sodium *tert*-butoxide (NaO*t*Bu, 255 mg, 2.66 mmol), 2-dicyclohexylphosphino-2′,4′,6′-triisopropylbiphenyl (XPhos, 26.0 mg, 54.5 μmol) and palladium(II) acetate ($Pd(OAc)_2$, 8.4 mg, 37.4 μmol) were dissolved in super-dehydrated toluene (10.0 mL) and stirred at 110 °C for 3.5 hours. After cooling to room temperature, the organic layer was extracted with chloroform/brine. The organic layer was then dried over Na_2SO_4, filtered and concentrated using a rotary evaporator. The crude product was then filtrated through silica gel with chloroform as eluent to remove residual catalyst. After removal of solvent, the crude product was distilled with the least amount of chloroform, and recrystallized by adding acetone as poor solvent to give the pure compound as a pale green-white solid in moderate yield (451 mg, 79%). Equivalent synthetic procedures to that of MA-TA were applied for **FA-TA** in yield of 82.1% and for **PA-TA** in yield of 82.0%.

Material Characterization

MA-TA: ^{1}H NMR (800 MHz, $CDCl_3$, δ): 8.84–8.86 (m, 2H), 7.46–748 (m, 4H), 6.93–6.97 (m, 4H), 6.33–6.34 (m, 2H) 2.16 (18H), 1.83 (12H) 1.72 (s, 6H). ^{13}C-NMR (201 MHz, $CDCl_3$, δ): 184.35, 169.70, 144.67, 140.64, 136.86, 131.38, 131.33, 130.11, 126.37, 125.29, 120.71, 114.13, 41.29, 40.67, 36.82, 36.01, 31.30, 28.55. APCI-MS (m/z): $[M+H]^+$ calcd. for $C_{44}H_{49}N_4$, 633.3957; found, 633.3976; Elemental analysis calcd. (%) for $C_{44}H_{48}N_4$: C, 83.50; H, 7.70; N, 8.89; found: C, 83.50; H, 7.64; N, 8.85.

FA-TA: ^{1}H NMR (800 MHz, CD_2Cl_2, δ): 8.93–8.95 (m, 2H), 7.85 (d, J = 7.6 Hz, 2H), 7.65–7.67 (m, 2H), 7.43 (d, J = 7.5 Hz, 2H) 7.41 (td, J = 7.4 Hz, 0.96 Hz, 2H), 7.30 (td, J = 7.4 Hz, 0.96 Hz, 2H) 6.93 (ddd, J = 8.5, 7.0, 1.5 Hz, 2H) 6.57–6.59 (m, 2H) 6.44 (dd, J = 8.6 Hz, 0.88 Hz, 2H) 6.38 (dd, J = 7.8 Hz, 0.80 Hz) 2.19 (d, J = 2.9 Hz, 12H), 2.16 (m, 6H) 1.84–1.88 (m, 12H). ^{13}C-NMR (201 MHz, CD_2Cl_2, δ): 184.14, 169.39, 156.25, 144.11, 140.80, 138.95, 136.95, 131.17, 131.04, 128.06, 127.41, 127.24, 126.99, 125.23, 124.51, 120.29, 119.74, 114.48, 56.48, 41.03, 40.36, 36.50, 28.43. APCI-MS (m/z): $[M+H]^+$ calcd. for $C_{54}H_{51}N_4$, 755.4114; found, 755.4103; Elemental analysis calcd. (%) for $C_{54}H_{50}N_4$: C, 86.07; H, 6.74; N, 7.35; found: C, 85.90; H, 6.68; N, 7.41.

PA-TA: ^{1}H NMR (800 MHz, CD_2Cl_2, δ): 8.74–8.76 (m, 2H), 7.25–7.30 (6H), 7.22–7.23 (m, 2H), 7.03–7.06 (m, 2H), 7.01–7.03 (m, 4H), 6.87–6.90 (m, 4H), 6.48 (m, 2H), 2.13–2.14 (18H), 1.81–1.85 (m, 12H). ^{13}C-NMR (201 MHz, CD_2Cl_2, δ): 184.04, 169.35, 146.21, 143.92, 141.61, 136.63, 130.96, 130.59, 130.03, 129.73, 129.33, 127.31, 126.57, 126.01, 120.01, 113.84, 56.43, 40.97, 40.32, 36.48, 28.40. APCI-MS (m/z): $[M+H]^+$ calcd. for $C_{54}H_{53}N_4$, 757.4270; found, 755.4280; Elemental analysis calcd. (%) for $C_{54}H_{52}N_4$: C, 85.77; H, 6.97; N, 7.33; found: C,

85.68; H, 6.92; N, 7.40.

161209_MA-TA
1H 1pluse
300K

```
Current Data Parameters
NAME        161209_MA-TA
EXPNO                  1
PROCNO                 1

F2 - Acquisition Parameters
Date_           20161209
Time                9.02
INSTRUM            spect
PROBHD   5 mm CPTCI 1H-
PULPROG             zg30
TD                131072
SOLVENT             CDCl3
NS                     8
DS                     2
SWH            12820.513 Hz
FIDRES          0.097813 Hz
AQ              5.1118078 sec
RG                  11.3
DW                 39.000 usec
DE                 16.00 usec
TE                 302.0 K
D1             1.00000000 sec
TD0                    1

======== CHANNEL f1 ========
NUC1                  1H
P1                 8.00 usec
PL1                1.50 dB
PL1W        16.89365387 W
SFO1         800.1548009 MHz

F2 - Processing parameters
SI                131072
SF          800.1500223 MHz
WDW                   EM
SSB       0
LB        0 Hz
GB        0
PC                  1.00
```

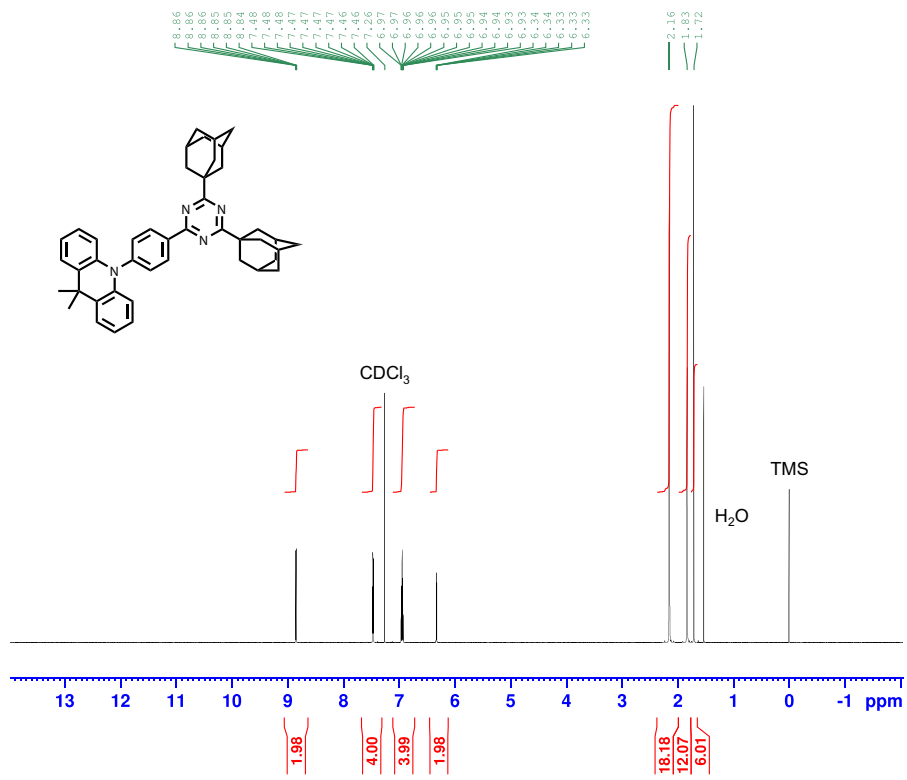

161209_MA-TA
13C
300K

```
Current Data Parameters
NAME        161209_MA-TA
EXPNO                 22
PROCNO                 1

F2 - Acquisition Parameters
Date_           20161209
Time               10.33
INSTRUM            spect
PROBHD   5 mm CPTCI 1H-
PULPROG          zgpg30
TD                262144
SOLVENT             CDCl3
NS                   256
DS                     0
SWH            52083.332 Hz
FIDRES          0.198682 Hz
AQ              2.5165825 sec
RG                  2050
DW                 9.600 usec
DE                 16.00 usec
TE                 302.0 K
D1             1.00000000 sec
D11            0.03000000 sec
TD0                    1

======== CHANNEL f1 ========
NUC1                 13C
P1                12.00 usec
PL1               -1.50 dB
SFO1        201.2179978 MHz

======== CHANNEL f2 ========
CPDPRG[2         waltz16
NUC2                 1H
PCPD2             80.00 usec
PL2                7.00 dB
PL12              21.50 dB
PL13              21.50 dB
PL2W         4.76127863 W
PL12W        0.16893655 W
PL13W        0.16893655 W
SFO2         800.1548009 MHz

F2 - Processing parameters
SI                131072
SF          201.1978818 MHz
WDW                   EM
SSB       0
LB                 0.10 Hz
GB        0
PC                  1.40
```

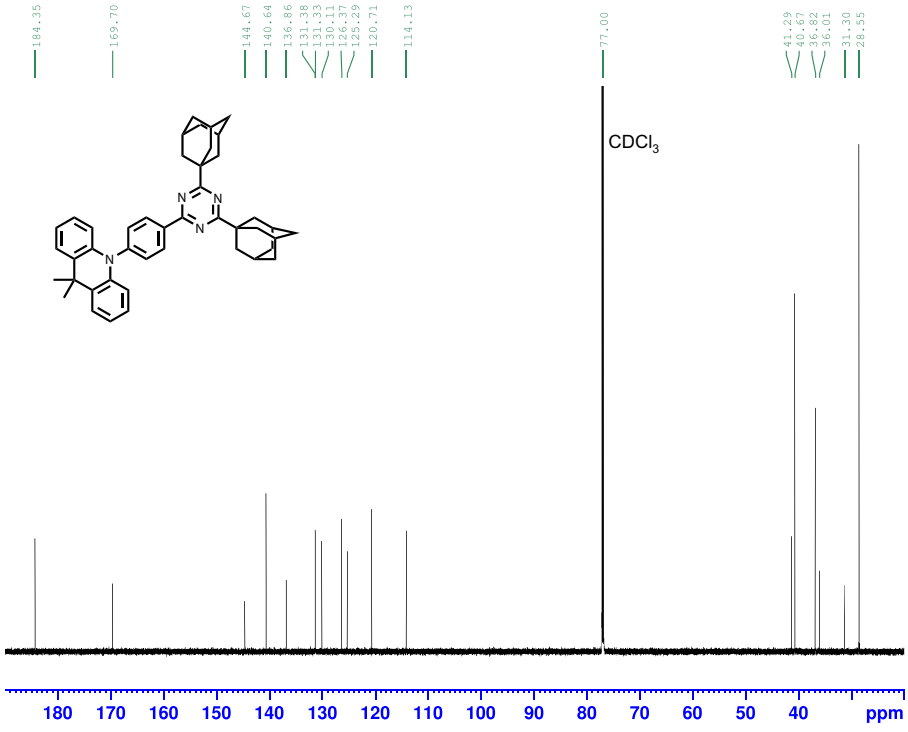

161209_FA-TA
1H 1pluse
300K

```
Current Data Parameters
NAME        161209_FA-TA
EXPNO                  1
PROCNO                 1

F2 - Acquisition Parameters
Date_           20161209
Time               11.14
INSTRUM             spect
PROBHD   5 mm CPTCI 1H-
PULPROG             zg30
TD                131072
SOLVENT           CD2Cl2
NS                     8
DS                     2
SWH            12820.513 Hz
FIDRES          0.097813 Hz
AQ              5.1118078 sec
RG                  11.3
DW                39.000 usec
DE                16.00 usec
TE                302.0 K
D1             1.00000000 sec
TD0                    1

======== CHANNEL f1 ========
NUC1                  1H
P1                  8.00 usec
PL1                 1.50 dB
PL1W         16.89365387 W
SFO1         800.1548009 MHz

F2 - Processing parameters
SI                131072
SF           800.1500346 MHz
WDW                 EM
SSB       0
LB        0 Hz
GB        0
PC                  1.00
```

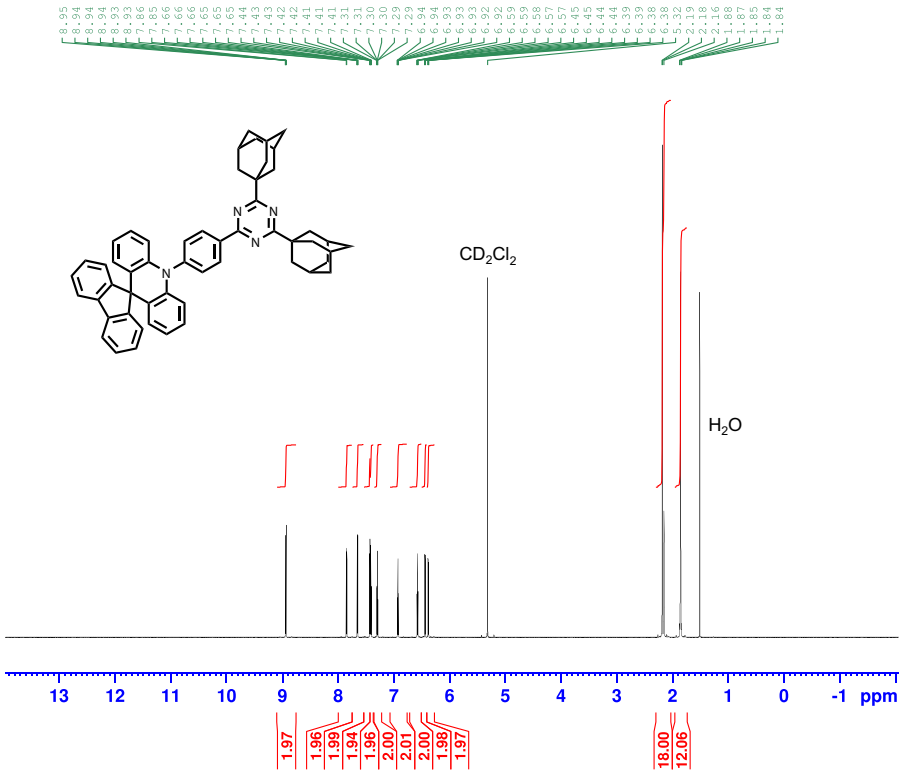

161209_FA-TA
13C
300K

```
Current Data Parameters
NAME        161209_FA-TA
EXPNO                  2
PROCNO                 1

F2 - Acquisition Parameters
Date_           20161209
Time               11.24
INSTRUM             spect
PROBHD   5 mm CPTCI 1H-
PULPROG          zgpg30
TD                262144
SOLVENT           CD2Cl2
NS                   512
DS                     0
SWH            52083.332 Hz
FIDRES          0.198682 Hz
AQ              2.5165825 sec
RG                  2050
DW                9.600 usec
DE                16.00 usec
TE                302.0 K
D1             1.00000000 sec
D11            0.03000000 sec
TD0                    1

======== CHANNEL f1 ========
NUC1                 13C
P1                12.00 usec
PL1               -1.50 dB
SFO1        201.2179978 MHz

======== CHANNEL f2 ========
CPDPRG[2         waltz16
NUC2                 1H
PCPD2             80.00 usec
PL2                7.00 dB
PL12              21.50 dB
PL13              21.50 dB
PL2W          4.76127863 W
PL12W         0.16893655 W
PL13W         0.16893655 W
SFO2         800.1548009 MHz

F2 - Processing parameters
SI                131072
SF           201.1979391 MHz
WDW                 EM
SSB       0
LB                0.10 Hz
GB        0
PC                  1.40
```

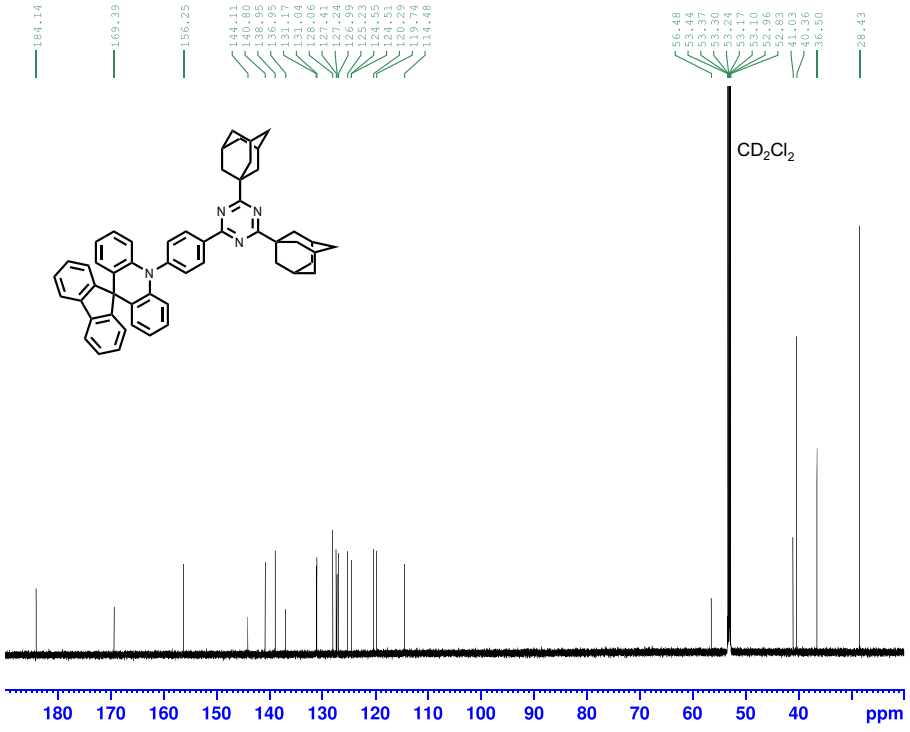

161209_PA-TA
1H 1pluse
300K

```
Current Data Parameters
NAME         161209_PA-TA
EXPNO                   1
PROCNO                  1

F2 - Acquisition Parameters
Date_           20161209
Time               12.09
INSTRUM             spect
PROBHD    5 mm CPTCI 1H-
PULPROG             zg30
TD                131072
SOLVENT           CD2Cl2
NS                     8
DS                     2
SWH            12820.513 Hz
FIDRES          0.097813 Hz
AQ              5.1118078 sec
RG                  11.3
DW                39.000 usec
DE                16.00 usec
TE                302.0 K
D1             1.00000000 sec
TD0                    1

======== CHANNEL f1 ========
NUC1                   1H
P1                  8.00 usec
PL1                 1.50 dB
PL1W         16.89365387 W
SFO1         800.1548009 MHz

F2 - Processing parameters
SI                131072
SF          800.1500346 MHz
WDW                   EM
SSB       0
LB        0 Hz
GB        0
PC                  1.00
```

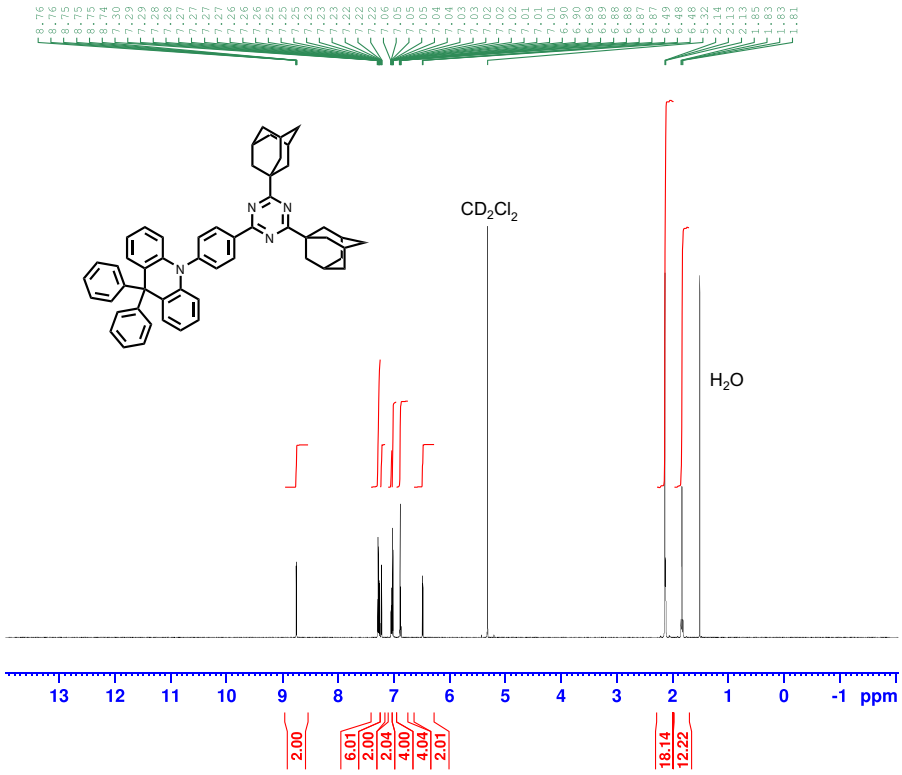

161209_PA-TA
13C
300K

```
Current Data Parameters
NAME         161209_PA-TA
EXPNO                   2
PROCNO                  1

F2 - Acquisition Parameters
Date_           20161209
Time               12.21
INSTRUM             spect
PROBHD    5 mm CPTCI 1H-
PULPROG          zgpg30
TD               262144
SOLVENT           CD2Cl2
NS                   256
DS                     0
SWH            52083.332 Hz
FIDRES          0.198682 Hz
AQ              2.5165825 sec
RG                  2050
DW                9.600 usec
DE                16.00 usec
TE                302.0 K
D1             1.00000000 sec
D11            0.03000000 sec
TD0                    1

======== CHANNEL f1 ========
NUC1                  13C
P1                 12.00 usec
PL1                -1.50 dB
SFO1         201.2179978 MHz

======== CHANNEL f2 ========
CPDPRG[2         waltz16
NUC2                   1H
PCPD2              80.00 usec
PL2                 7.00 dB
PL12               21.50 dB
PL13               21.50 dB
PL2W          4.76127863 W
PL12W         0.16893655 W
PL13W         0.16893655 W
SFO2         800.1548009 MHz

F2 - Processing parameters
SI                131072
SF          201.1979389 MHz
WDW                   EM
SSB       0
LB                 0.10 Hz
GB        0
PC                  1.40
```

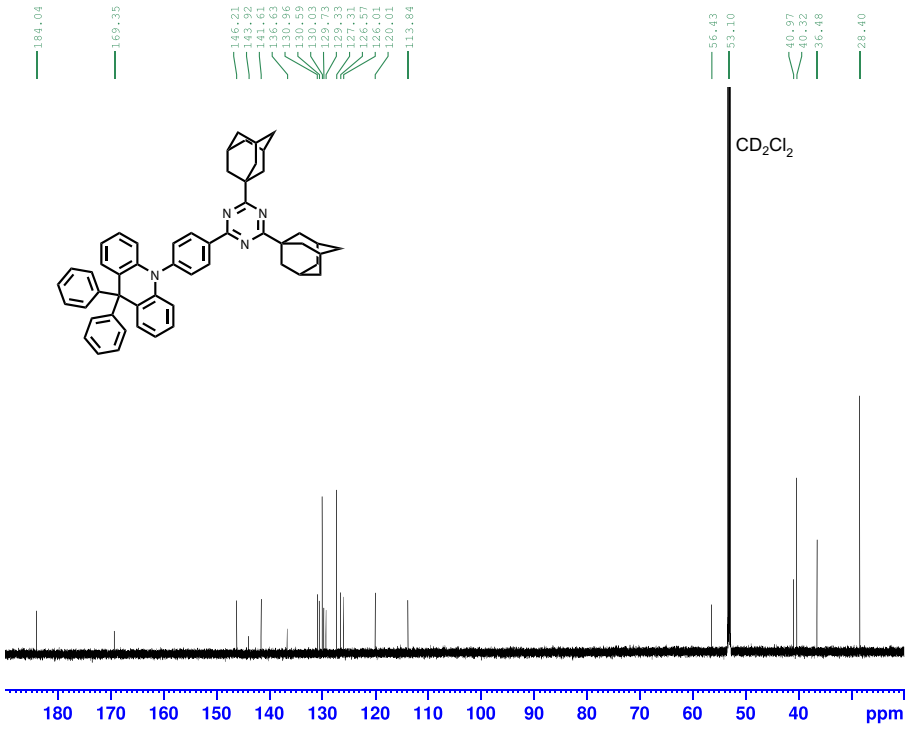

Physical and photophysical properties of the emitters

Thermal properties:

Differential scanning calorimetry (DSC1, METTLER TOLEDO) was performed to determine T_g, defined as the onset of the DSC curve. T_g values were obtained from the second heating scan of the samples after the first scan. For the first run, the samples were heated to above the melting point of each molecule and rapidly quenched on an Al plate to obtain amorphous samples. Differential thermal analysis (TG-DTA 2000SEα, NETZSCH Japan K.K.) was performed to determine the sublimation temperature (T_{sub}) and decomposition temperature (T_d), defined as the point of 50% and 5% weight loss of the thermogravimetric analysis (TGA) curve, respectively. Sample masses for all the experiments were ~10 mg.

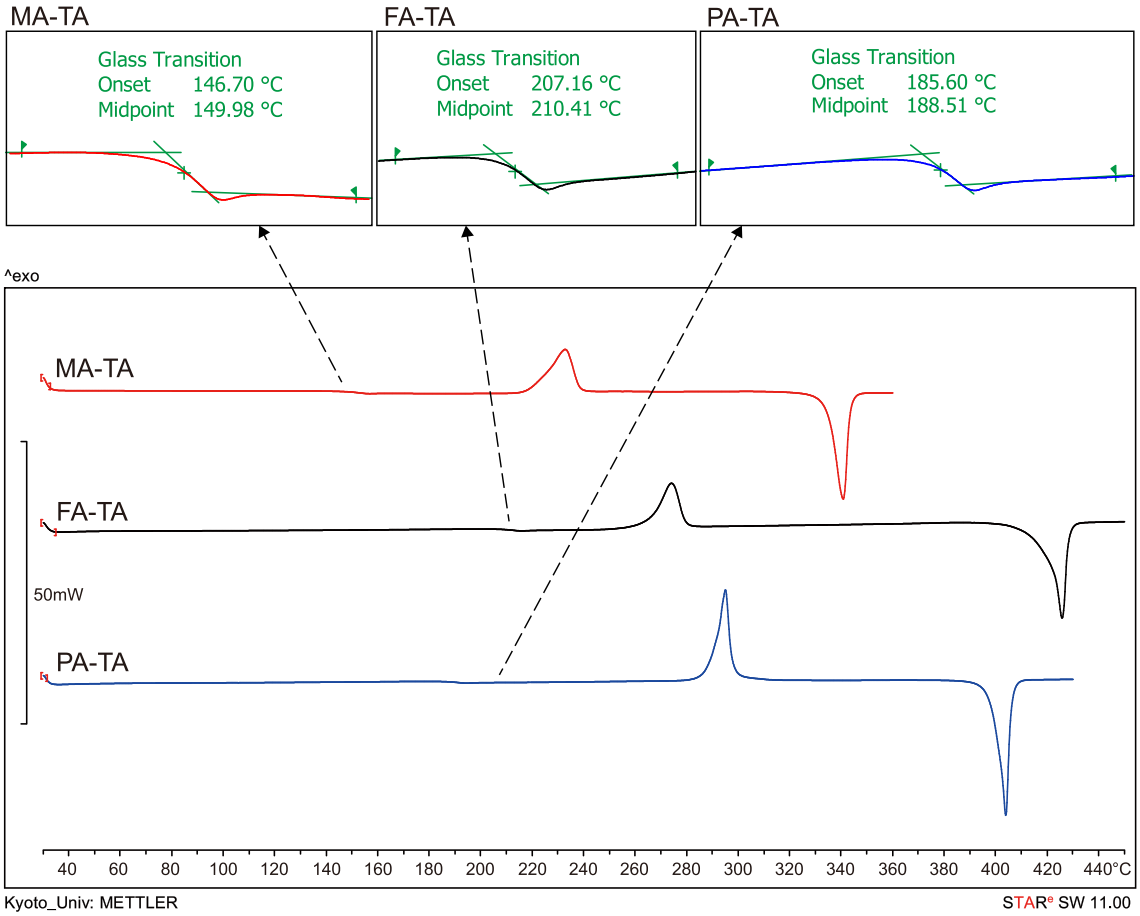

Supplementary Figure 3.3. DSC curve of MA-TA, FA-TA and PA-TA. The glass transition temperature (T_g) is determined from the onset of the DSC curve as shown in enlarged images (top). The midpoints of the DSC curves are also shown in the top images.

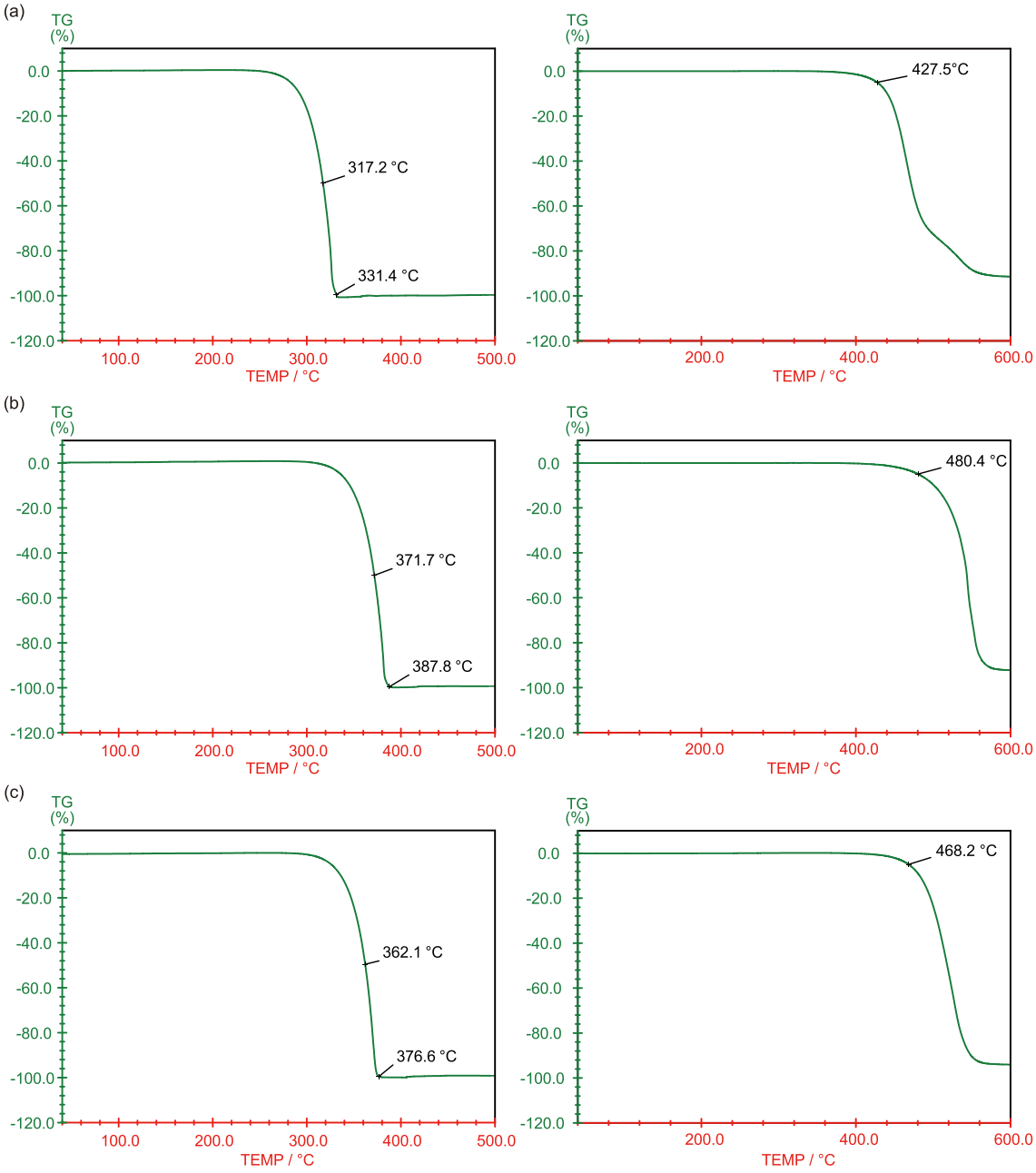

Supplementary Figure 3.4. TGA curve at 100 Pa (left side) and atmospheric pressure (right side) of (a) MA-TA, (b) FA-TA and (c) PA-TA. The points corresponding to 50% (sublimation temperature, T_{sub}) and 100% weight loss of the TGA curves are indicated on the left-side figures. The points corresponding to 5% weight loss of the TGA curves (decomposition temperature, T_d) are indicated on the right-side figures.

Photoelectron spectroscopy

Photoelectron yield spectroscopy in the air (AC-3, Riken Keiki) was conducted to determine the HOMO energy level of the materials. The HOMO energy level was obtained from the intersection point of the ground level with the approximate line of the square of photon counts per second.

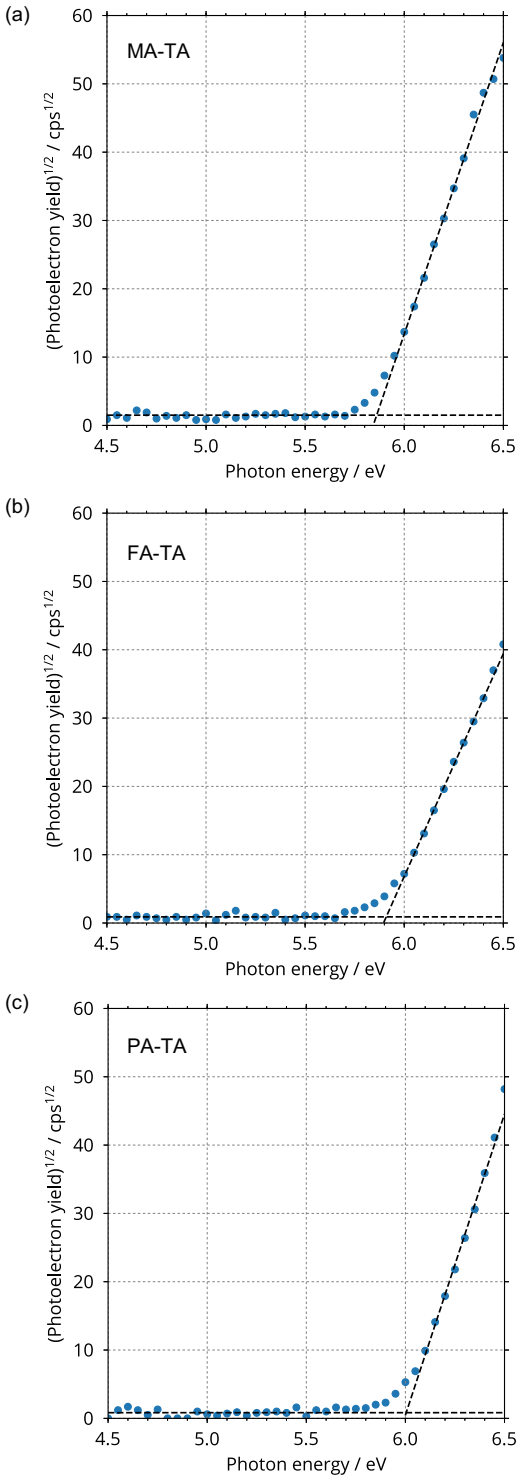

Supplementary Figure 3.5. The squares of the photoelectron yield measured in air atmosphere plotted as a function of photon energy for (a) MA-TA, (b) FA-TA and (c) PA-TA. Ionization potentials are determined from the onset of the plots.

Photophysical properties

General procedure for photophysical measurements

UV-vis absorption spectra were measured by a UV-vis spectrophotometer (V-750ST, JASCO, Japan) and photoluminescence (PL) spectra were measured by a spectrofluorometer (Fluoromax-4P, HORIBA, Japan). Photoluminescence quantum yields (Φ_{PL}) were measured by an absolute PLQY spectrometer (Quantaurus-QY C11347-01, Hamamatsu Photonics, Japan). Φ_{PL} in 10^{-5} M toluene solution were collected with and without > 15 minutes Ar gas bubbling. Φ_{PL} for films were collected with and without N_2 flow. The temperature-dependent transient PL decay measurements were conducted by a fluorescence lifetime measurement system (Quantaurus-Tau C11367-01, Hamamatsu Photonics, Japan) and a cryostat (Oxford Instruments, Optistat DN2, UK).

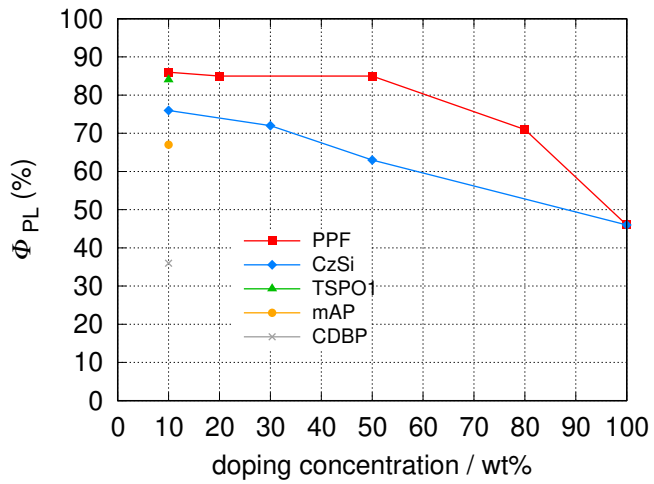

Supplementary Figure 3.6. Φ_{PL} of the films using different host materials as a function of the doping concentration of FA-TA.

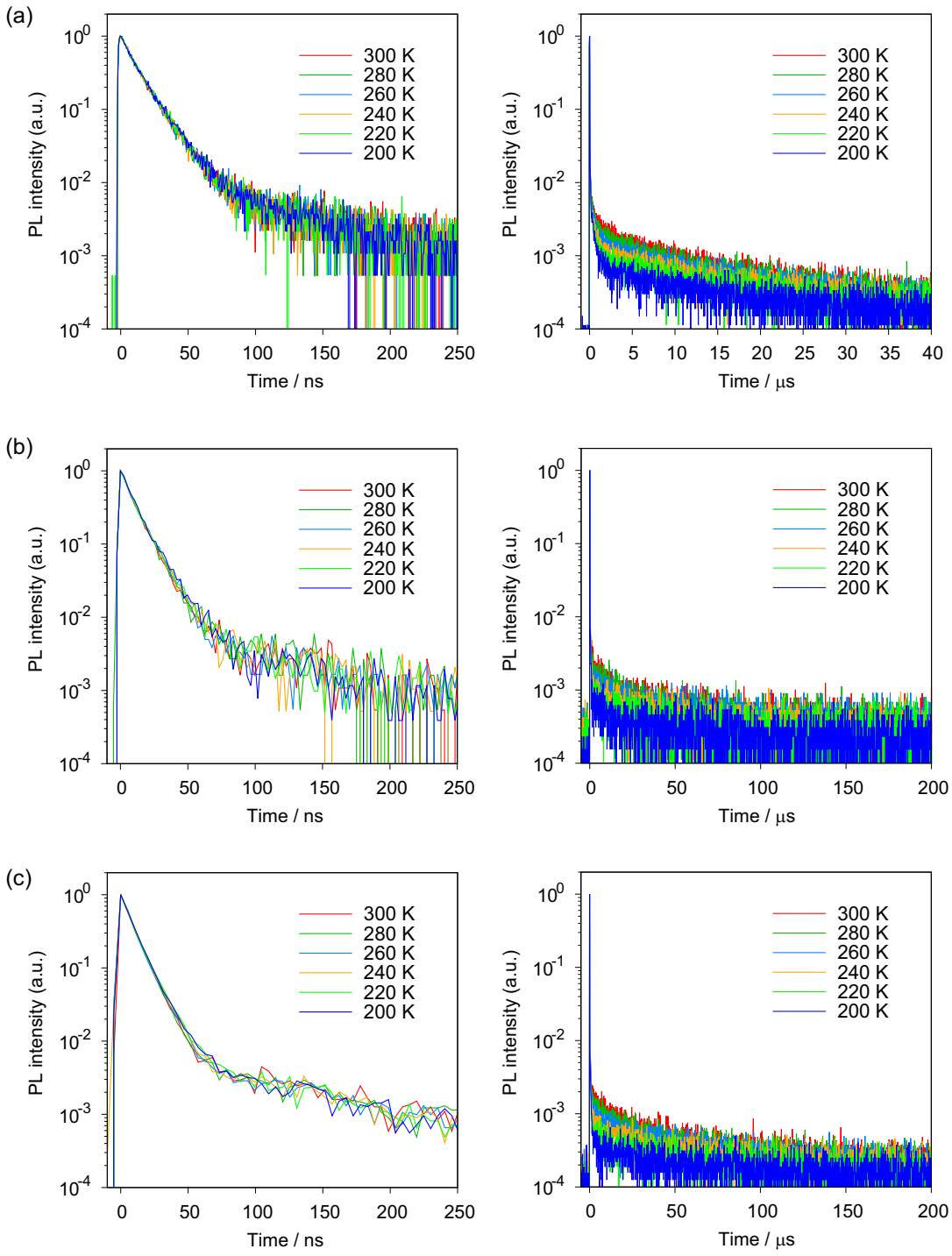

Supplementary Figure 3.7. PL decay spectra of short range (left) and long range (right) of 10 wt% Emitter:CzSi film where emitters are (a) MA-TA, (b) FA-TA and (c) PA-TA measured at every 20 K from 200 K to 300 K. Observed wavelength is PL peak maximum wavelength of corresponding film.

Supplementary Table 3.2. Fitting parameters of the 10 wt% Emitter:CzSi films.

Emitter	τ_1 / ns	τ_2 / ns	τ_3 / ns	A_1	A_2	A_3	τ_p [a] / ns	τ_d [a] / μs
MA-TA	14.4	4.32×10^3	2.33×10^3	3.59×10^4	23.5	12.0	14.4	18.3
FA-TA	12.0	8.18×10^3	5.49×10^3	1.10×10^5	45.5	23.3	12.0	44.4
PA-TA	10.6	1.21×10^4	8.84×10^3	5.51×10^4	18.1	7.54	10.6	69.5

[a] $\tau_p = \tau_1$, [b] average lifetime calculated by following equation: $\tau_d = \Sigma A_i\tau_i^2 / \Sigma A_i\tau_i$. A_i is pre-exponential factor of τ_i.

Supplementary Table 3.3. Φ_{PL} in 10^{-5} M toluene solution without and with Ar bubbling.

emitter	Φ_{PL} (%)	
	without Ar bubbling	with Ar bubbling
MA-TA	18	45
FA-TA	20	40
PA-TA	15	34

Device fabrication and characterization

General procedures for solution-processed OLEDs fabrication

All the spin-coating and baking processes were conducted in air atmosphere. Before the spin-coating, the ITO substrates were cleaned as follows: 10 minutes sonication in each of detergent, H_2O (twice), acetone and 2-propanol; 5 minutes exposure to hot steam of 2-propanol; UV-O_3 irradiation for over 30 minutes. PEDOT:PSS (CLEVIOS™ P VP CH 8000, Hereus) diluted in ultrapure H_2O at the ratio of 1:1 wt% was spin-coated on the cleaned ITO substrates at 4000 rpm for 30 s and baked at 150 °C for 10 minutes. After 5 minutes of N_2 flow for cooling, PVK (Mw ~ 1,100,000) was spin-coated at 2000 rpm for 30 s from 10 mg mL^{-1} 1,2-dichlorobenzene solution onto the PEDOT:PSS layer. After baking at 120 °C for 10 minutes and cooling with N_2 flow for 5 minutes, emitting layers were formed at 2200 rpm for 30 s from 10 mg mL^{-1} toluene solution upon the PVK layer. After baking at 100 °C for 10 minutes and cooling with N_2 flow for 5 minutes, upper layers of TSPO1, TPBi, Liq and Al were formed by vacuum deposition using a deposition apparatus (SE-4260, ALS Technology, Japan) at the pressure of < 10^{-4} Pa, by which were obtained OLEDs with active areas of 4 mm^{-2}. The OLEDs were finally encapsulated with glass caps, and getter films were attached to remove oxygen and moisture.

General procedure for device characterization

The OLEDs' characteristics were measured using an integrating sphere (C9920-12, Hamamatsu Photonics, Japan) with a source meter (2400, Keithley, Japan).

Chapter 4

Molecular Design Realizing Very Fast Reverse Intersystem Crossing in Purely Organic Emitter

4.1. Introduction

Highly efficient emission in organic light emitting diodes (OLEDs) requires conversion of triplet excitons into light because triplet excitons account for 75% of all excitons generated by charge recombination of holes and electrons in OLEDs. One strategy for making use of triplets is to use transition-metal-based phosphorescent materials, mediated by the heavy atom effect [1], and this strategy has realized high performance OLEDs [2]. Recently, an alternative approach was demonstrated whereby emitters fluoresce from triplet states via thermal up-conversion to the singlet state [3]. The system, named thermally activated delayed fluorescence (TADF) [4], has since been vigorously investigated [5-7]. Although TADF materials containing heavy-metals (e.g. Cu, Pd, Ag, Sn and Au) have been shown excellent performances [8-13], even non-metal TADF systems have achieved internal quantum efficiencies of 100% in experimental OLEDs [3, 14, 15]. In both metal-containing and non-metal cases, the energy gap between the lowest excited singlet (S_1) and the lowest triplet (T_1) states, termed ΔE_{ST}, should be small, typically < 0.1 eV, to accomplish spin up-conversion from T_1 to S_1 by reverse intersystem crossing (RISC). A small ΔE_{ST} can be achieved simply by separating the highest occupied molecular orbital (HOMO) and lowest unoccupied molecular orbital (LUMO) of the emitter molecule or those of different donor and acceptor molecules. At the initial stage of TADF research, and even now, HOMO-LUMO separation has been typically realized by covalently-bonding electron donor and acceptor units.

However, in terms of conservation of angular momentum, intersystem crossing (ISC) and

RISC between S_1 and T_1 states having the same configuration character are theoretically spin-forbidden, known as El-Sayed rule [16]. Therefore, the rate constants of RISC (k_{RISC}) cannot be great in TADF systems having similar CT-type S_1 and T_1 states (^{1}CT and ^{3}CT, respectively). Recently, inclusion of locally excited triplet (^{3}LE) states has been reported to accelerates RISC [17-24]; the inherently forbidden ^{3}CT to ^{1}CT transition (^{3}CT$\nrightarrow{}^1$CT) becomes effective by intervening ^{3}LE (^{3}CT$\rightarrow{}^3$LE$\rightarrow{}^1$CT). Hence, the best performance can be expected when we realize energy level matching of these three states, i.e., $E(^1\text{CT}) \approx E(^3\text{CT}) \approx E(^3\text{LE})$, where E(X) means the energy level of X state. Here, we propose a systematic design principle to realize the ideal TADF system.

4.2. Results and discussion

Concept of molecular design. In designing ideal TADF molecules, we conceptually consider *"tilted"* face-to-face (tFF) alignment of donor and acceptor segments. Figure 4.1a shows an example, composed of 9,9-dimethyl-9,10-dihydro**A**cridine (abbreviated as **A** and coloured red) and 2,4-diphenyl-1,3,5-**T**riazine (abbreviated as **T** and coloured blue) as donor and acceptor components, respectively. The HOMO on the **A** segment and the LUMO on the **T** segment spatially overlap when they are in close proximity, resulting in both S_1 and T_1 being through-space CT states [25-27] (^{1}CT and ^{3}CT, respectively). As calculated by density functional theory (DFT) and time dependent DFT (TD-DFT) with Gaussian16 (LC-ωPBE/6-31+G(d) level of theory), both energy levels, $E(^1\text{CT})$ and $E(^3\text{CT})$, increased as the distance between the donor and acceptor (d_{DA}) increased, as shown at the top of Figure 4.1b. Here, d_{DA} is defined as the distance between the nitrogen in **A** and the carbon in **T**, emphasized by black boldface at the top of Figure 4.1a. The energy difference between ^{3}CT and ^{1}CT, $\Delta E(^3\text{CT}\rightarrow{}^1\text{CT})$, decreases with increasing d_{DA} (Figure 4.1b top and middle). Here, $\Delta E(\text{X}\rightarrow\text{Y})$ indicates the energy change from the X to Y states. This value is defined as positive for an uphill transition and negative for a downhill transition. When d_{DA} is greater than 3.5 Å, a value of $\Delta E(^3\text{CT}\rightarrow{}^1\text{CT})$ less than 0.1 eV is realized and a sufficiently small $\Delta E(^3\text{CT}\rightarrow{}^1\text{CT})$ is obtained at $d_{\text{DA}} > 4.0$ Å. Unlike the d_{DA} dependence of $E(^1\text{CT})$ and $E(^3\text{CT})$, $E(^3\text{LE})$ only weakly depends on d_{DA} (at the top of Figure 4.1b). Therefore, both $E(^1\text{CT})$ and $E(^3\text{CT})$ approach the originally higher lying $E(^3\text{LE})$ as d_{DA} increases. Finally, the energy level matching of the three states occurs at approximately $d_{\text{DA}} \approx 4.7$ Å.

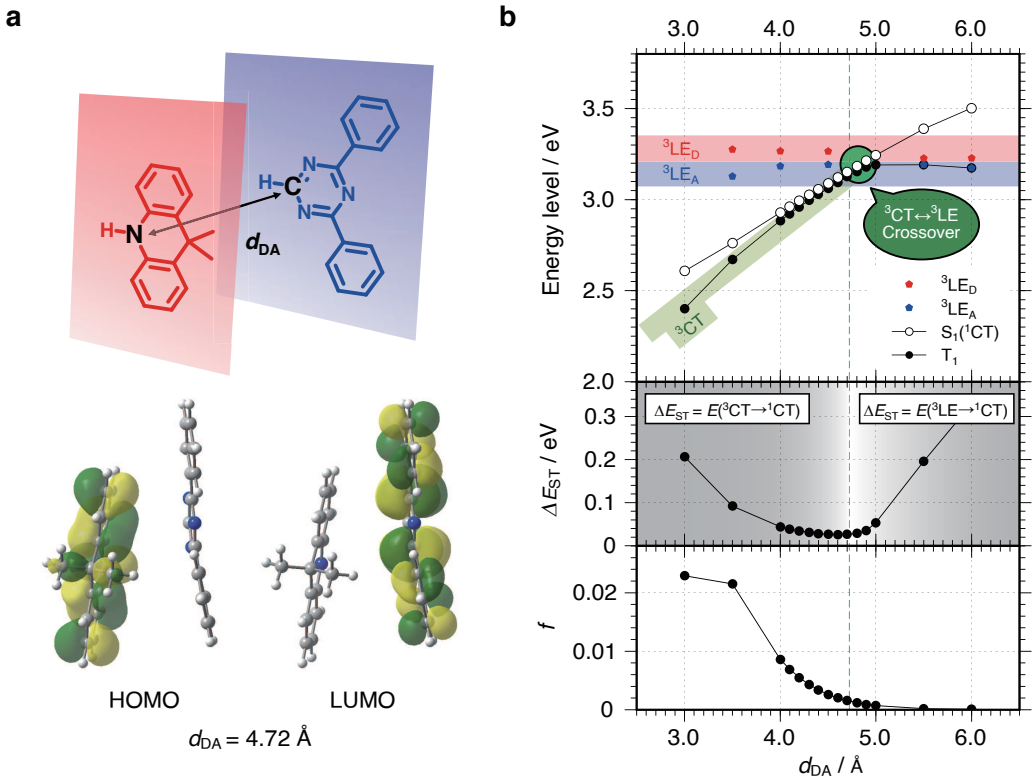

Figure 4.1 | Conceptual molecular design. a, Fragment structures of donor (red) and acceptor (blue) are shown. Donor and acceptor pair is tilted (~10°) face-to-face alignment spatially separated with certain distance (d_{DA}). HOMO and LUMO with d_{DA} of 4.72 Å are also shown. **b**, DFT-calculated energy levels of S_1, T_1, ^3LE_D, ^3LE_A (top), ΔE_{ST} (middle) and f (bottom) as a function of d_{DA}, where ^3LE_D and ^3LE_A denote the ^3LE states on donor and acceptor fragments, respectively. Green dashed line indicates d_{DA} = 4.72 Å, which corresponds to the d_{DA} of DFT optimized structure for TpAT-tFFO at the ground state.

This example demonstrates that the above-mentioned ideal situation, $E(^1\mathrm{CT}) \approx E(^3\mathrm{CT}) \approx E(^3\mathrm{LE})$, can be intentionally realized by optimizing the d_{DA}. However, an additional requirement should be satisfied to realize very fast RISC. As shown later, spin-orbit coupling matrix element values (SOCMEVs) are negligibly small, not only between ^{1}CT and ^{3}CT but also between ^{1}CT and ^{3}LE, when **A** and **T** segments are in a **c**ompletely parallel **F**ace-to-**F**ace (**cFF**) alignment with each other. Thus, the transition is still spin-forbidden even between ^{1}CT and ^{3}LE for the cFF alignment. This problem can be solved by simply *"tilting"* the face-to-face alignment. Although the SOCMEV remains negligible between ^{1}CT and ^{3}CT irrespective of the alignment, the SOCMEV between ^{1}CT and ^{3}LE becomes notable for the *"**t**ilted **F**ace-to-**F**ace"* (**tFF**) alignment.

Here, we selected triptycene (**Tp**) as the scaffold for realizing **tFF** donor-acceptor alignment with an *"**O**ptimized"* distance (**tFFO**). The new molecule, composed of **Tp**, **A** and **T** segments with **tFFO** structure, is named "**TpAT-tFFO**". The **A** and **T** segments are introduced at the 1st and 8th positions of **Tp** (Figure 4.2a). The d_{DA} of 4.72 Å and tilted face-to-face donor-acceptor alignment are expected from the DFT optimized structure (Figure 4.2b). The calculated $\Delta E_{\mathrm{ST}} = \Delta E(^3\mathrm{CT}\rightarrow{}^1\mathrm{CT})$ of 0.019 eV (Supplementary Table 4.1) is satisfactory small, and $\Delta E(^3\mathrm{CT}\rightarrow{}^3\mathrm{LE})$ and $\Delta E(^3\mathrm{LE}\rightarrow{}^1\mathrm{CT})$ were also small. The tilted face-to-face donor-acceptor alignment provides a much greater SOCMEV than that of the case of completely parallel face-to-face alignment. The oscillator strength, f, decreases with increasing d_{DA} (Figure 4.1b, at the bottom), but the experimentally-obtained photoluminescence (PL) quantum yields (PLQY) of TpAT-tFFO were satisfactory at 84% and 76% in toluene solution and a doped film, respectively. The PLQY was as high as 71% even for a neat film. A k_{RISC} exceeding 10^7 s^{-1} was realized from our newly designed molecule, TpAT-tFFO.

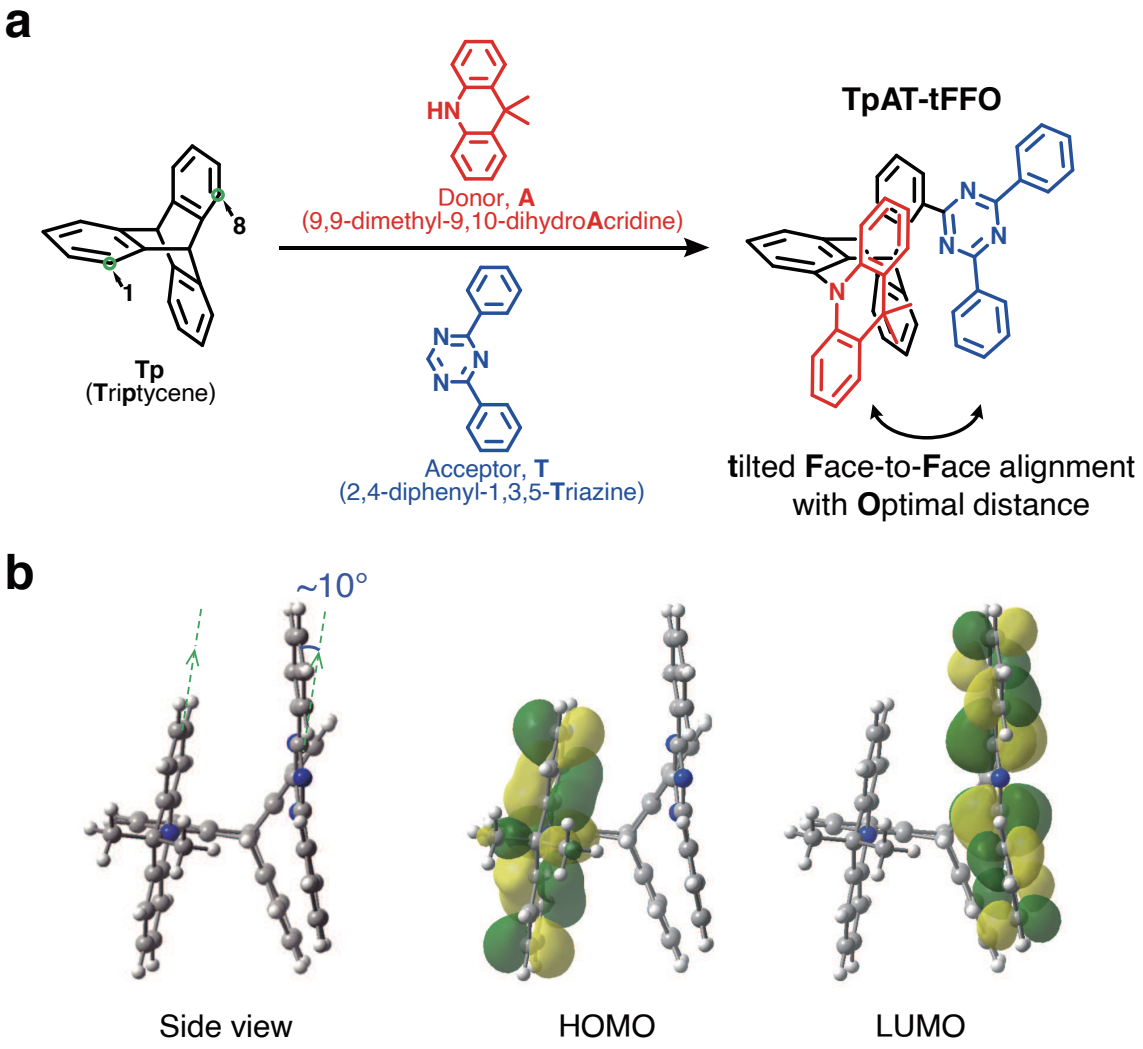

Figure 4.2 | Molecular structure and its frontier molecular orbitals. a, Schematic molecular structure of TpAT-tFFO. **b**, DFT-optimized structure of TpAT-tFFO (side view, HOMO and LUMO)

Theoretical calculation of TpAT-tFFO. Figure 4.2a shows the molecular structure of TpAT-tFFO, where **A** (red) and **T** (blue) are intended to serve as donor and acceptor fragments, respectively. The DFT-optimized structure in Figure 4.2b was obtained at the B3LYP/6-31G(d) level of theory with a polarizable continuum model (PCM) in toluene implemented in Gaussian 16 program package [28]. By introducing **A** and **T** at the 1st and 8th positions of **Tp**, a *tilted* face-to-face donor-acceptor alignment with mostly optimized d_{DA} was realized, as we had designed for. For the TD-DFT calculations, Brédas and co-workers have previously reported that a long-range corrected density functional, LC-ωPBE with the optimized range-separation parameter ω for the target molecules, accurately describes the excited state energy of TADF system [23, 29]. Therefore, for the excited state calculation, we used a combination of the LC-ωPBE functional and 6-31+G(d) basis set, the same combination with Brédas' calculations. The results of the TD-DFT calculations are summarized in Supplementary Table 4.1. The optimized value of ω for TpAT-tFFO was 0.1664 $Bohr^{-1}$ (Supplementary Figure 4.1a). A small value of $\Delta E(^3CT \rightarrow ^1CT)$ of 0.019 eV was achieved owing to the spatially separated HOMO and LUMO (Figure 4.2b). Moreover, the ^3LE state is also close-lying as we designed; $\Delta E(^3CT \rightarrow ^3LE)$ and $\Delta E(^3LE \rightarrow ^1CT)$ were 0.075 and −0.057 eV, respectively.

The **Tp** scaffold created a tilted donor-acceptor alignment as described above. The tilt angle (i.e. the angle between the normal vectors of **A** and **T** segments) of TpAT-tFFO was ~10° (Figure 4.2b, shown as the angle between the intersegment planes in the figure for clarity). We calculated the SOCMEV for TpAT-tFFO. We also calculated it for the donor-acceptor (**A**-**T**) pair without **Tp** in the cFF alignment with d_{DA} of 4.72 Å (AT-cFFO), where the π-planes of the **A** and **T** segments were in a completely parallel alignment, as shown in Supplementary Figure 4.2b. Similar to Brédas' calculations [23], we calculated SOCMEV with the ADF2018 package [30]. The LCY-ωPBE functional and Slater-type all-electron TZP were used for the calculation,

where the range parameter, γ [31], was optimized to be 0.213 (details of the optimization are provided in the Supplementary Information). When the **A** and **T** segments were in the completely parallel alignment, an SOCMEV of 0.00 cm^{-1} was obtained between ^{1}CT and ^{3}CT. Furthermore, the SOCMEV was small, 0.05 cm^{-1}, even between ^{1}CT and ^{3}LE. This result provides crucial insight that transitions between ^{1}CT and ^{3}LE are not always allowed. On the contrary, TpAT-tFFO exhibited a markedly enhanced SOCMEV of 0.61 cm^{-1} between ^{1}CT and ^{3}LE owing to the tilting of the donor-acceptor alignment. The SOCMEV was still zero between ^{1}CT and ^{3}CT even for the tilted alignment.

These calculations demonstrate that effective RISC is expected for our tFFO molecular design strategy, which simultaneously achieves a very close energy level alignment, i.e. $E(^1\text{CT}) \approx E(^3\text{CT}) \approx E(^3\text{LE})$, and significant SOCMEV between ^{1}CT and ^{3}LE. We successfully synthesized TpAT-tFFO and performed photophysical measurements after train sublimation. Details of the synthesis and characterization of TpAT-tFFO are provided in the Supplementary Information.

Photophysical properties. One interesting feature of TpAT-tFFO is a weak CT absorption observed in the visible wavelength region, despite the very efficient emission. Figure 4.3a shows UV-vis absorption and emission spectra of TpAT-tFFO in toluene solution at a concentration of 10^{-4} M. We used a concentration an order of magnitude larger than our standard to detect the weak CT absorption clearly. Intense ππ*-type absorption [32] was observed in the ultraviolet region around ~300 nm with a molar absorption coefficient ε around 2×10^4 cm^{-1} M^{-1}, whereas absorption from 350 to 450 nm was two orders of magnitude smaller ($\varepsilon \sim 2\times10^2$ cm^{-1} M^{-1}). The absorption in this region can be assigned as CT-type by TD-DFT calculations. Our natural transition orbital (NTO) analysis confirmed that the highest occupied NTO (HONTO) was mainly distributed on **A** and the lowest unoccupied NTO (LUNTO) on **T** of TpAT-tFFO (Supplementary Figure 4.1b). The absorption can be attributed to a CT transition through the space between **A** and **T** rather than through the bond. In sharp contrast to the weak absorption, TpAT-tFFO exhibited strong sky-blue emission with a peak maximum wavelength of 485 nm. The PL quantum yield (PLQY or Φ_{PL}) markedly increased from 1.8% to 84% after 30 min of Ar bubbling to remove dissolving oxygen (O_2) molecules, which act as a quencher for the triplet excited state of emitters. The excitation wavelength of 365 nm corresponds to the CT absorption. 98% of the total PLQY originated from delayed fluorescence, which experiences the process of $S_1 \rightarrow T_1 \rightarrow S_1$ or cycles of the process. The significantly large jump of the PLQYs indicates that ***"both the ISC and RISC are rapid"*** compared with radiative and non-radiative decays. Transient PL decay curves before and after Ar bubbling and the detailed analyses are provided in Figure 4.3b and Supplementary Table 4.2. The values of k_{ISC} and k_{RISC} were determined to be 5.2×10^7 and 1.2×10^7 s^{-1}, respectively (Table 4.1, see Supplementary Information for the derivation of the rate constants). The k_{RISC} value, on the order of 10^7 s^{-1}, is very large and is the same order of k_{ISC}. To the best of our knowledge, the k_{RISC} of TpAT-tFFO is

the fastest, not only among all TADF systems but also among all organic systems composed only of H, C and N. Purely organic materials (materials composed only of non-metal elements) having $k_{RISC} \geq 10^6$ s^{-1} are summarized in Supplementary Table 4.3. Using our tFFO strategy, we can expect larger k_{RISC} values for materials including heavier atoms, such as P, S, Cl, Br, I, Cu, Pd, Ag, Sn and/or Au.

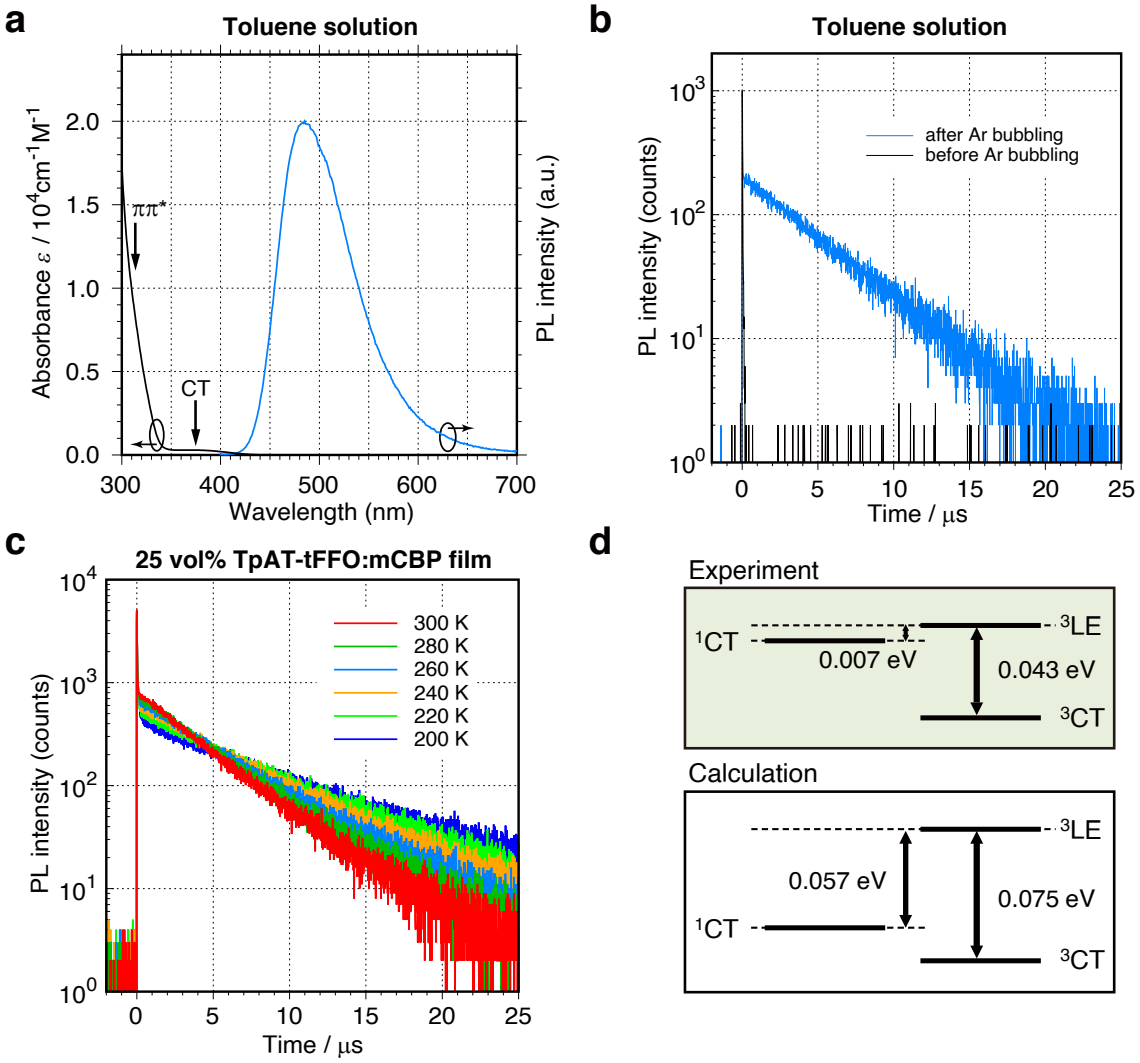

Figure 4.3 | Photoluminescent characteristics. a, UV-vis absorption and PL spectra of TpAT-tFFO in toluene solution. **b,** Transient PL decay curves of TpAT-tFFO in toluene solution before (black) and after (blue) Argon gas bubbling for 30 min. **c,** Transient PL decay curves of 25 vol% TpAT-tFFO:mCBP film from 200 to 300 K. **d,** Experimental energy level diagram of TpAT-tFFO in the 25 vol% TpAT-tFFO:mCBP film. Corresponding diagram by DFT calculations is also shown.

Table 4.1 | Values of rate constants, k_r^S, k_{nr}^S, k_{ISC}, and k_{RISC}, of TpAT-tFFO (s^{-1}). Both the ISC and RISC are rapid compared with radiative and non-radiative decays.

k_r^S	k_{nr}^S	k_{ISC}	k_{RISC}
1.1×10^6	2.0×10^5	5.2×10^7	1.2×10^7

In most TADF materials, the lifetime of delayed fluorescence in transient PL experiments is distributed in amorphous films, indicating a distribution of k_{RISC} values. Some molecules exhibit fast RISC, but some do not. Conversely, the TpAT-tFFO doped film showed a single lifetime in the delayed fluorescence (Figure 4.3c) as discussed later; all the TpAT-tFFO molecules in the system had very high k_{RISC} values. These results indicate that effective electron spin inversion occurs in all the TpAT-tFFO molecules as expected from the above design concept, although the heavy atom effect cannot be expected for molecules composed only of H, C and N.

We fabricated thin films of TpAT-tFFO both neat and doped into 3,3'-di(9*H*-carbazol-9-yl)-1,1'-biphenyl (mCBP) host and conducted transient PL and PLQY measurements at room temperature (~300 K). The PL decay curves of delayed fluorescence in the films were fitted with a single exponential with the lifetime, τ_d, of 3.2 μs for the neat film and 4.1 μs for the doped film, where the rate-limiting process was radiative decay after RISC. In normal donor-acceptor bonded TADF molecules, the torsion angle, which is flexible in most cases, varies from molecule to molecule in the amorphous aggregates as mentioned in our previous work [33]. The torsion angle distribution induces a distribution of ΔE_{ST} [34], which results in multi-exponential decay of delayed emission rather than single-exponential. Therefore, TADF performance depends on the molecules having various torsion angles. Our observation of a single exponential decay of the delayed fluorescence for TpAT-tFFO systems indicates a uniform ΔE_{ST} even in the amorphous state, which suggests that all emitters exhibit excellent performances when the molecule is appropriately designed. We performed temperature dependent transient PL measurements for a 25 vol% TpAT-tFFO:mCBP film (Figure 4.3c). From the Arrhenius analysis, both the ISC and RISC processes were found to have positive activation energies. The activation energies for ISC and RISC, E_a(ISC) and E_a(RISC), were determined to be 0.007 and 0.043 eV, respectively. The energy level diagram is shown in Figure

4.3d, where the assignments of ^{1}CT, ^{3}CT and ^{3}LE were performed based on computational calculations (at the bottom of Figure 4.3d). A further additional feature of TpAT-tFFO is suppression of concentration quenching: Φ_{PL} of 76% in the 25 vol% TpAT-tFFO:mCBP film and Φ_{PL} of 71% even in the neat film. Such insensitivity to concentration is beneficial for device optimization, particularly for controlling charge balance in OLEDs. This further suggests great potential of TpAT-tFFO as an excellent emitter for OLEDs.

Organic light-emitting diodes. Figure 4.4 and Table 4.2 shows the device performances of a TpAT-tFFO-based OLED with the device structure, indium-tin-oxide (ITO) (50 nm)/4,4′-cyclohexylidenebis[*N*,*N*-bis(4-methylphenyl)benzenamine] (TAPC) (60 nm)/1,3-bis(9,9-dimethylacridin-10(9*H*)-yl)benzene (mAP) [35] (10 nm)/25 vol% TpAT-tFFO:mCBP (30 nm)/2,8-bis(diphenylphosphoryl)dibenzo[b,d]furan (PPF) (10 nm)/1,3-bis[3,5-di(pyridin-3-yl)phenyl]benzene (BmPyPhB) (35 nm)/lithium quinolin-8-olate (Liq) (1 nm)/Al (80 nm). A device with an optimized doping concentration of 25 vol% provided a maximum external quantum efficiency (EQE_{MAX}) of 19.2% (see Supplementary Figure 4.3 and Supplementary Table 4.4 for the doping concentration dependence). We obtained EQEs of 19.1 and 18.1% at 100 and 1,000 cd m^{-2}, respectively with sky-blue emission. Moreover, EQEs of 14.4 and 11.6% were retained even at high luminance of 10,000 and 20,000 cd m^{-2}, respectively. When an out-coupling sheet was attached to the OLED, EQE_{MAX} of 29.0% and EQE of 19.7% at 20,000 cd m^{-2} were realized.

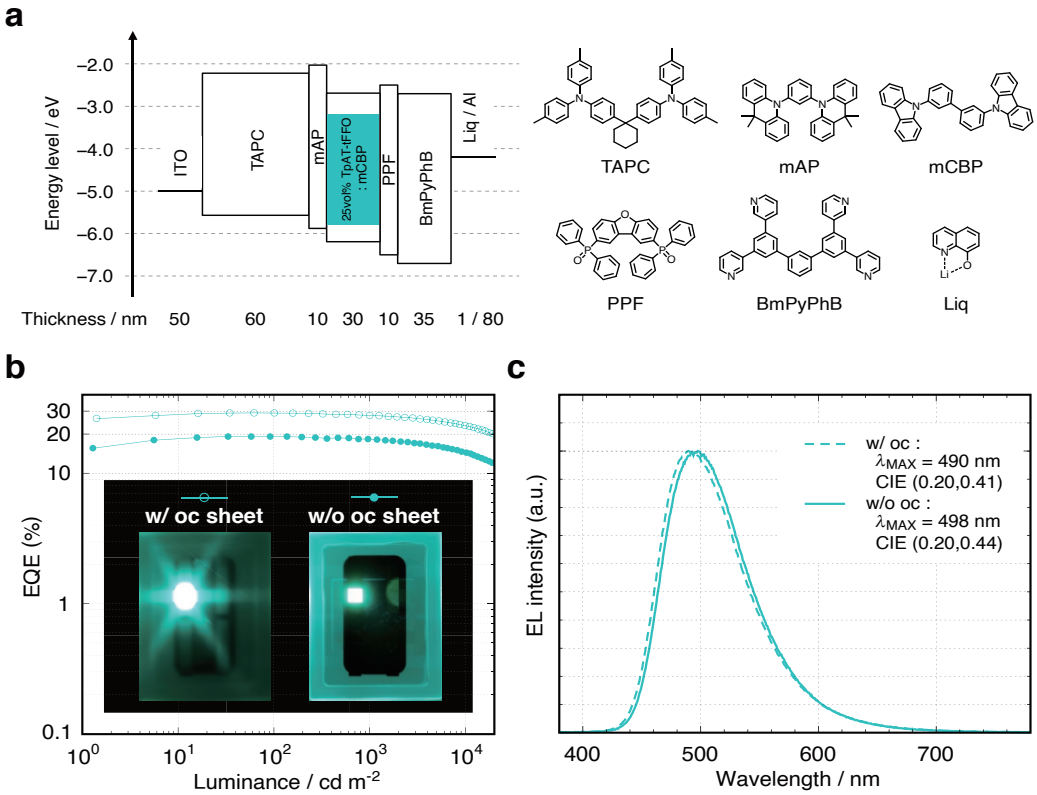

Figure 4.4 | Electroluminescencent device characteristics of TpAT-tFFO-based OLEDs with doping concentration of 25 vol% w/ and w/o out coupling sheet. a, Device structure and the chemical structures used for respective layers. **b**, EQE-luminance characteristics. **c**, EL spectra at 10 mA cm^{-2}. Filled circles in **b** and solid line in **c** indicate results from the device without out-coupling sheet, whereas open circles in **b** and broken line in **c** are results from that with an out-coupling sheet. λ_{MAX} and CIE(x,y) denote EL peak maximum wavelength and Commission Internationale de l'Eclairage (CIE) coordinates, respectively.

Table 4.2 | Device performances of TpAT-tFFO-based OLEDs with doping concentration of 25 vol% w/ and w/o out-coupling sheet.

Emitter	EQE_{MAX}	EQE_{100}[a]	$EQE_{1,000}$	$EQE_{10,000}$	$EQE_{20,000}$	L_{MAX} / cd m^{-2}	CIE(x,y)[c]
TpAT-tFFO (w/ oc sheet)	29.0	29.0 (0.3%)[b]	27.6 (4.8%)	22.8 (21.4%)	19.7 (32.1%)	48,930	(0.20, 0.41)
TpAT-tFFO (w/o oc sheet)	19.2	19.1 (0.4%)	18.1 (5.4%)	14.4 (24.7%)	11.6 % (38.9%)	33,870	(0.20, 0.44)

(a) EQE_Y denotes EQE value at Y = cd m^{-2}.

(b) EQE roll-off (%) was shown in parentheses, where EQE roll-off (%) = (EQE_{MAX}−EQE) / EQE_{MAX} × 100.

(c) Colour coordinates of Commission Internationale de l'Eclairage (CIE).

Considering the fast triplet-to-singlet conversion ability of TpAT-tFFO, we further investigated TADF assisted fluorescence (TAF)-OLED [36] using TpAT-tFFO as the assist dopant. For easy comparison of performances with preceding TAF studies, we used a frequently used conventional blue fluorescent dye, 2,5,8,11-Tetrakis(1,1-dimethylethyl)perylene (TBPe), as the emitter and 9-(4-tert-Butylphenyl)-3,6-bis(triphenylsilyl)-9H-carbazole (CzSi) as the host (4 vol%TBPe:26 vol%TpAT-tFFO:CzSi). From the PL measurement, emission from TBPe was clearly observed in the TpAT-tFFO based TAF system (Supplementary Figure 4.4a), indicating Förster resonance energy transfer successfully occurs. It should be noted that the PL (and EL, see below) spectrum of the TAF system is blue-shifted compared with that of the TADF emitter system. The Φ_{PL} resulted in 87%. Reflecting the large k_{RISC} value of TpAT-tFFO, the transient PL experiment provided a very fast lifetime of the delayed component, τ_d = 0.36 μs (Supplementary Figure 4.4b). Figure 4.5 and Table 4.3 show the device performances for the TAF-OLED; ITO (50 nm)/TAPC (60 nm)/mAP (10 nm)/1 vol%TBPe:24 vol%TpAT-tFFO:CzSi (20 nm)/PPF (10 nm)/BmPyPhB (35 nm)/Liq (1 nm)/Al (80 nm). The device exhibited blue emission of CIE(0.15, 0.23) with EQE_{MAX} = 18.7%. The device reached very high luminance up to 18,000 cd m^{-2} (see also Supplementary Figure 4.5) and exhibited alleviated roll-off with EQE of 11.8% even at high brightness of 10,000 cd m^{-2}, which are the best performance among blue TAF-OLEDs reported using TBPe as fluorescence dye (Table 4.3) [36-40]. We believe that the great device performance is attributed to the large k_{RISC} of TpAT-tFFO. Our tFFO-based TADF materials are found to be also useful for assist dopant of TAF systems, which will realize highly efficient deep-blue OLEDs with narrow EL spactra even at high brightness.

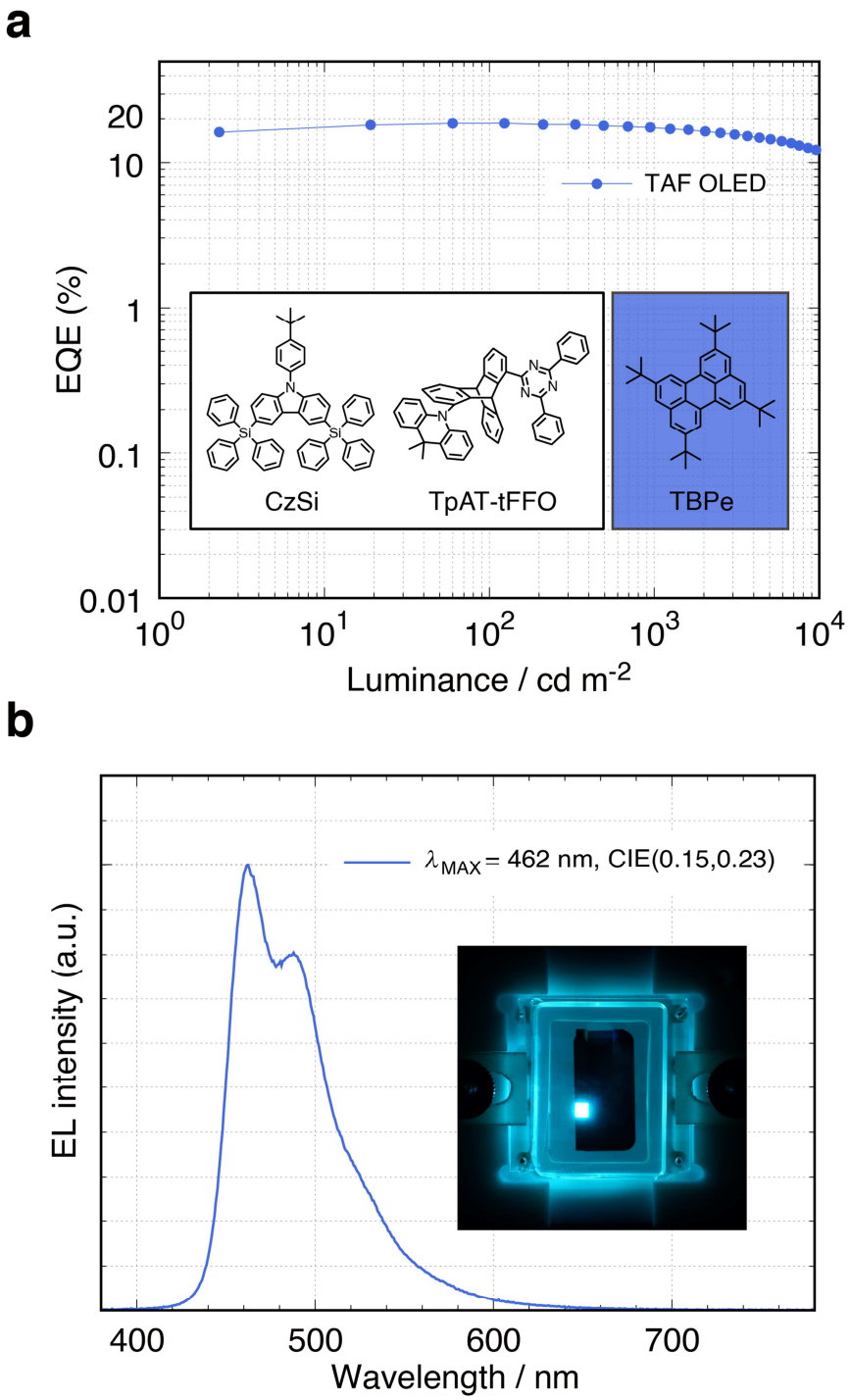

Figure 4.5 | Electroluminescent device characteristics of TpAT-tFFO-based TAF OLED. a, EQE-luminance characteristics the OLED. **b,** EL spectra at 10 mA cm^{-2} together with the photograph of the EL emission.

Table 4.3 | Device performances of TpAT-tFFO-based TAF OLEDs. Preceding performances of TAF-OLEDs are also shown for comparison.

Reference	Emitting layer	EQE (%)				CIE(x,y)
		EQE_{MAX}	$EQE_{1,000}$[a]	$EQE_{5,000}$	$EQE_{10,000}$	
This work	1vol%TBPe:24vol %TpAT-tFFO:CzSi	18.7	17.1	14.4	11.8	(0.15, 0.23)
Ref. [36]	1wt%TBPe:15wt% ACRSA:DPEPO	13.4	8.7	N.A.	—	(0.17, 0.30)
Ref. [37]	0.1wt%TBPe:50wt %CzAcSF:DPEPO	18.1	N.A.[b]	N.A.	—	(0.15, 0.22)
Ref. [38]	TBPe:CzAcSF:DPE PO	18	N.A.	N.A.	N.A.	N.A.
Ref. [39]	TBPe:DMAC-DPS: DPEPO	18.8	13.5	N.A.	—	(0.14, 0.25)
Ref. [40]	0.5wt%TBPe:5CzC N:DPOBBPE	19.5	N.A.	—[c]	—	(0.15, 0.23)

(a) EQE_Y denotes EQE value at Y cd m^{-2}.

(b) N.A. denotes that data was not assigned.

(c) — denotes that the device do not reach the luminance.

4.3. Conclusion

In this study, we show a novel molecular design concept to achieve very fast RISC in organic molecules. Our molecular design strategy, tFFO, realizes both energy matching of the three states, $E(^1\mathrm{CT}) \approx E(^3\mathrm{CT}) \approx E(^3\mathrm{LE})$, and significant SOCMEV. This strategy enables and promotes RISC processes even in purely organic molecules. Our example molecule, named TpAT-tFFO, realized a very fast k_{RISC} exceeding 10^7 s^{-1}, which is the fastest k_{RISC} reported to date among all organic molecules including TADF ones, and finally achieved great device performance in its application to OLEDs

TpAT-tFFO yields additional features; 1) negligible CT absorption, 2) large O_2 sensitivity of PLQY in solution, 3) uniform ΔE_{ST} in amorphous films at various temperatures, and 4) negligible concentration quenching. To develop the much sought after deep-blue TADF-based OLEDs, stable host materials with high T_1 energies are required; however, the development has been difficult. The use of a *neat* emitter layer is one way to avoid the host problem. As for emitters, a small Stokes shift is favourable for avoiding red shifting and making the blue emission deeper. However, in that case, exciton self-quenching occurs owing to the inevitable overlap of absorption and emission spectra. The negligible absorption and negligible concentration quenching are considerable advantages for future developments of such deep-blue emitters and devices. The transparency in the visible light region is particularly advantageous for multi-colour systems where absorption of long wavelength emitters tends to overlap with emission of short wavelength emitters. We also expect that the great O_2 sensitivity of TpAT-tFFO in solution will give excellent performance in applications to O_2 sensors. The tFFO design can be expanded to various types, various numbers, and various combinations of donors, acceptors and scaffolds. Furthermore, other kinds of functional segments might also be introduced into the scaffolds. Such expansion of tFFO designs will provide novel materials with

further improved performances and give insights into fundamental photophysical properties of these materials.

(Chapter 4 is the unedited Author's version of a Submitted Work)

4.4. References

[1] M. A. Baldo, S. Lamansky, P. E. Burrows, M. E. Thompson and S. R. Forrest, *Appl. Phys. Lett.* **1999**, *75*, 4.

[2] H. Sasabe and J. Kido, *Eur. J. Org. Chem.* **2013**, *2013*, 7653.

[3] H. Uoyama, K. Goushi, K. Shizu, H. Nomura and C. Adachi, *Nature* **2012**, *492*, 234.

[4] Y. Onoue, K. Hiraki and Y. Nishikawa, *Anal. Sci.* **1987**, *3*, 509.

[5] Z. Yang, Z. Mao, Z. Xie, Y. Zhang, S. Liu, J. Zhao, J. Xu, Z. Chi and M. P. Aldred, *Chem. Soc. Rev.* **2017**, *46*, 915.

[6] M. Y. Wong and E. Zysman-Colman, *Adv. Mater.* **2017**, *29*, 1605444.

[7] T. Huang, W. Jiang and L. Duan, *J. Mater. Chem. C* **2018**, *6*, 5577.

[8] A. Endo, M. Ogasawara, A. Takahashi, D. Yokoyama, Y. Kato and C. Adachi, *Adv. Mater.* **2009**, *21*, 4802.

[9] Z. Q. Zhu, T. Fleetham, E. Turner and J. Li, *Adv. Mater.* **2015**, *27*, 2533.

[10] H. Yersin, R. Czerwieniec, M. Z. Shafikov and A. F. Suleymanova, *Chemphyschem* **2017**, *18*, 3508.

[11] D. Di, A. S. Romanov, L. Yang, J. M. Richter, J. P. Rivett, S. Jones, T. H. Thomas, M. Abdi Jalebi, R. H. Friend, M. Linnolahti, M. Bochmann and D. Credgington, *Science* **2017**, *356*, 159.

[12] W. P. To, D. Zhou, G. S. M. Tong, G. Cheng, C. Yang and C. M. Che, *Angew. Chem. Int. Ed.* **2017**, *56*, 14036.

[13] R. Hamze, J. L. Peltier, D. Sylvinson, M. Jung, J. Cardenas, R. Haiges, M. Soleilhavoup, R. Jazzar, P. I. Djurovich, G. Bertrand and M. E. Thompson, *Science* **2019**, *363*, 601.

[14] H. Kaji, H. Suzuki, T. Fukushima, K. Shizu, K. Suzuki, S. Kubo, T. Komino, H. Oiwa, F. Suzuki, A. Wakamiya, Y. Murata and C. Adachi, *Nat. Commun.* **2015**, *6*, 8476.

[15] T.-A. Lin, T. Chatterjee, W.-L. Tsai, W.-K. Lee, M.-J. Wu, M. Jiao, K.-C. Pan, C.-L. Yi,

C.-L. Chung, K.-T. Wong and C.-C. Wu, *Adv. Mater.* **2016**, *28*, 6976.

[16] M. A. El-Sayed, *J. Chem. Phys.* **1963**, *38*, 2834.

[17] C. M. Marian, *J. Phys. Chem. C* **2016**, *120*, 3715.

[18] F. B. Dias, J. Santos, D. R. Graves, P. Data, R. S. Nobuyasu, M. A. Fox, A. S. Batsanov, T. Palmeira, M. N. Berberan-Santos, M. R. Bryce and A. P. Monkman, *Adv. Sci.* **2016**, *3*, 1600080.

[19] J. Gibson, A. P. Monkman and T. J. Penfold, *Chemphyschem* **2016**, *17*, 2956.

[20] M. K. Etherington, J. Gibson, H. F. Higginbotham, T. J. Penfold and A. P. Monkman, *Nat. Commun.* **2016**, *7*, 13680.

[21] I. Lyskov and C. M. Marian, *J. Phys. Chem. C* **2017**, *121*, 21145.

[22] T. Hosokai, H. Matsuzaki, H. Nakanotani, K. Tokumaru, T. Tsutsui, A. Furube, K. Nasu, H. Nomura, M. Yahiro and C. Adachi, *Sci. Adv.* **2017**, *3*, e1603282.

[23] P. K. Samanta, D. Kim, V. Coropceanu and J. L. Brédas, *J. Am. Chem. Soc.* **2017**, *139*, 4042.

[24] H. Noda, H. Nakanotani and C. Adachi, *Sci. Adv.* **2018**, *4*, eaao6910.

[25] K. Kawasumi, T. Wu, T. Zhu, H. S. Chae, T. Van Voorhis, M. A. Baldo and T. M. Swager, *J. Am. Chem. Soc.* **2015**, *137*, 11908.

[26] S. Shao, J. Hu, X. Wang, L. Wang, X. Jing and F. Wang, *J. Am. Chem. Soc.* **2017**, *139*, 17739.

[27] H. Tsujimoto, D. G. Ha, G. Markopoulos, H. S. Chae, M. A. Baldo and T. M. Swager, *J. Am. Chem. Soc.* **2017**, *139*, 4894.

[28] M. J. Frisch, G. W. Trucks, H. B. Schlegel, G. E. Scuseria, M. A. Robb, J. R. Cheeseman, G. Scalmani, V. Barone, G. A. Petersson, H. Nakatsuji, X. Li, M. Caricato, A. V. Marenich, J. Bloino, B. G. Janesko, R. Gomperts, B. Mennucci, H. P. Hratchian, J. V. Ortiz, A. F. Izmaylov, J. L. Sonnenberg, Williams, F. Ding, F. Lipparini, F. Egidi, J. Goings, B. Peng, A. Petrone, T.

Henderson, D. Ranasinghe, V. G. Zakrzewski, J. Gao, N. Rega, G. Zheng, W. Liang, M. Hada, M. Ehara, K. Toyota, R. Fukuda, J. Hasegawa, M. Ishida, T. Nakajima, Y. Honda, O. Kitao, H. Nakai, T. Vreven, K. Throssell, J. A. Montgomery Jr., J. E. Peralta, F. Ogliaro, M. J. Bearpark, J. J. Heyd, E. N. Brothers, K. N. Kudin, V. N. Staroverov, T. A. Keith, R. Kobayashi, J. Normand, K. Raghavachari, A. P. Rendell, J. C. Burant, S. S. Iyengar, J. Tomasi, M. Cossi, J. M. Millam, M. Klene, C. Adamo, R. Cammi, J. W. Ochterski, R. L. Martin, K. Morokuma, O. Farkas, J. B. Foresman and D. J. Fox, Wallingford, CT, **2016**.

[29] H. Sun, C. Zhong and J. L. Brédas, *J. Chem. Theory. Comput.* **2015**, *11*, 3851.

[30] G. te Velde, F. M. Bickelhaupt, E. J. Baerends, C. Fonseca Guerra, S. J. A. van Gisbergen, J. G. Snijders and T. Ziegler, *J. Comput. Chem.* **2001**, *22*, 931.

[31] Y. Akinaga and S. Ten-no, *Chem. Phys. Lett.* **2008**, *462*, 348.

[32] W.-L. Tsai, M.-H. Huang, W.-K. Lee, Y.-J. Hsu, K.-C. Pan, Y.-H. Huang, H.-C. Ting, M. Sarma, Y.-Y. Ho, H.-C. Hu, C.-C. Chen, M.-T. Lee, K.-T. Wong and C.-C. Wu, *Chem. Commun.* **2015**, *51*, 13662.

[33] Y. Wada, S. Kubo and H. Kaji, *Adv. Mater.* **2018**, *30*, 1705641.

[34] Y. Olivier, B. Yurash, L. Muccioli, G. D'Avino, O. Mikhnenko, J. C. Sancho-Garcia, C. Adachi, T. Q. Nguyen and D. Beljonne, *Phys. Rev. Mater.* **2017**, *1*, 075602.

[35] J.-A. Seo, M. S. Gong, S. K. Jeon, J. Y. Lee, C. H. Noh and S. H. Kim, *Dyes and Pigments* **2015**, *123*, 254.

[36] H. Nakanotani, T. Higuchi, T. Furukawa, K. Masui, K. Morimoto, M. Numata, H. Tanaka, Y. Sagara, T. Yasuda and C. Adachi, *Nat. Commun.* **2014**, *5*, 4016.

[37] I. H. Lee, W. Song, J. Y. Lee and S.-H. Hwang, *J. Mater. Chem. C* **2015**, *3*, 8834.

[38] W. Song, I. Lee and J. Y. Lee, *Adv. Mater.* **2015**, *27*, 4358.

[39] S. H. Han and J. Y. Lee, *J. Mater. Chem. C* **2018**, *6*, 1504.

[40] S. K. Jeon, H. J. Park and J. Y. Lee, *ACS Appl. Mater. Interfaces* **2018**, *10*, 5700.

4.5. Supplementary Information

Supplementary Text

Material Synthesis and Characterization

General procedure for material characterization

^{1}H and ^{13}C NMR spectra were recorded with a JEOL ECA-600 spectrometer (600 MHz for ^{1}H) or Bruker Avance-III (800 MHz for ^{1}H and 201 MHz for ^{13}C). Chemical shifts are reported in δ ppm, using residual protons in deuterated solvents for ^{1}H NMR experiments and solvent peaks for ^{13}C NMR spectra as internal standards. Atmospheric pressure chemical ionization (APCI) mass spectra were measured with a Bruker micrOTOF-Q II (Bruker, Germany). Elemental analysis was conducted with a CHN analyser, MICRO CORDER JM10 (J-Science Lab Co., Ltd., Japan).

The synthesis scheme is summarized in Supplementary Scheme 5.1. A starting material, 1,8-dibromotriptycene, was prepared according to ref.[1].

Compound S1

A 60 mL portion of deoxidized toluene was added to a 100-mL round bottom Schlenk flask under Ar atmosphere, containing 1,8-dibromotriptycene (6.18 g, 15.1 mmol), 9,9-dimethyl-9,10-dihydroacridine (1.26 g, 6.03 mmol), $Pd_2(dba)_3{\cdot}CHCl_3$ (186 mg, 0.18 mmol), XPhos (172 mg, 0.36 mmol), and NaOtBu (1.15 g, 12.0 mmol). The mixture was stirred overnight at 120 °C. After the reaction mixture was cooled to ambient temperature, 20 mL of distilled water was added and the organic layer was extracted with 100 mL of ethyl acetate three times. The combined organics were dried over sodium sulfate, the crude mixture was concentrated under reduced pressure and then purified by silica gel column chromatography using hexane/dichloromethane = 4/1 as eluent. 2.37 g (4.40 mmol) of **Compound S1**

(Supplementary Scheme 5.1) was obtained in 73% yield.

Material Characterization

^{1}H NMR (600 MHz, $CDCl_3$, δ): 7.56–7.52 (m, 2H), 7.49 (d, J = 6.0 Hz, 1H), 7.41 (d, J = 6.0 Hz, 1H), 7.34 (d, J = 6.0 Hz, 1H) 7.24 (t, J = 6.0 Hz, 1H), 7.05 (d, J = 6.0 Hz, 1H), 7.02 (t, J =6.0 Hz, 1H), 6.98–6.90 (m, 5H), 6.85–6.76 (m, 3H), 5.87 (d, J =12.0 Hz, 1H), 5.76 (d, J = 12.0 Hz, 1H), 5.72 (s, 1H), 5.55 (s, 1H), 1.93 (s, 3H), 1.70 (s, 3H). APCI-MS (m/z): [M+H]+ calcd. for $C_{35}H_{27}BrN$, 540.1327; found, 540.1325.

Compound S2

In a 50-mL two-neck round bottom flask, **Compound S1** (1.77 g, 3.27 mmol) was dissolved in 25 mL of dehydrated THF under an Ar atmosphere and the solution was cooled to −78 °C. Therein, 3 mL (4.80 mmol) of *n*-BuLi solution 1.6 M in hexane was slowly added with stirring. After 2 h stirring at −78 °C, 0.78 mL (3.87 mmol) of 2-isopropoxy-4,4,5,5-tetramethyl-1,3,2-dioxaborolane was added to the solution, and the reaction mixture was slowly warmed up to ambient temperature. The crude solution was quenched with 1 M HCl aqueous solution and the resulting mixture layer was extracted with 50 mL of ethyl acetate three times. The combined organic layers were further washed with brine and distilled water, and dried over sodium sulfate. The crude mixture was concentrated under reduced pressure and then purified by silica gel column chromatography using hexane/dichloromethane = 7/3 as eluent. 0.864 g (1.47 mmol) of **Compound S2** (Supplementary Scheme 5.1) was obtained in 45% yield.

Material Characterization

^{1}H NMR (600 MHz, $CDCl_3$, δ): 7.51–7.49 (m, 3H), 7.43 (d, J = 6.0 Hz, 2H), 7.35 (d, J = 6.0 Hz, 1H), 7.18–7.14 (m, 2H) 7.04–6.96 (m, 4H), 6.91 (t, J = 6.0 Hz, 1H), 6.87–6.84 (m, 2H),

6.72 (t, J = 6.0 Hz, 1H), 6.31 (s, 1H), 6.04 (d, J = 6.0 Hz, 1H), 5.67 (d, J = 6.0 Hz, 1H), 5.57 (s, 1H), 1.95 (s, 3H), 1.43 (s, 3H), 0.94 (s, 6H), 0.81 (s, 6H). APCI-MS (m/z): [M+H]+ calcd. for $C_{41}H_{39}BNO_2$, 588.3074; found, 588.3094.

TpAT-tFFO

A 60-mL portion of deoxidized toluene and 6.0 mL of 2 M aqueous potassium carbonate (12.0 mmol) were added to a 100-mL round bottom Schlenk flask containing **Compound S2** (0.85 g, 1.45 mmol), 2-chloro-4,6-diphenyl-1,3,5-triazine (0.58 g, 2.17 mmol), and $Pd(PPh_3)_4$ (168 mg, 0.15 mmol). After three freeze-pump-thaw cycles under an Ar atmosphere, the mixture was stirred at 120 °C for 24 h. After the reaction mixture was cooled to ambient temperature, 40 mL of distilled water was added and the organic layer was extracted with 50 mL of ethyl acetate three times. The combined organics were dried over sodium sulfate, concentrated under reduced pressure and then purified by column chromatography using hexane/dichloromethane = 4/1. 0.679 g (0.98 mmol) of **TpAT-tFFO** was obtained in 68% yield.

Material Characterization

^{1}H NMR (800 MHz, CD_2Cl_2, δ): 8.47 (d, J = 7.5 Hz, 4H), 8.25 (dd, J = 7.8, 1.2 Hz, 1H), 7.70 (d, J = 7.2, 1.2 Hz, 1H), 7.62−7.59 (3H) 7.55 (d, J = 7.3 Hz, 1H), 7.47 (t, J = 7.7 Hz, 4H), 7.28−7.25 (4H), 7.20 (s, 1H), 7.15 (dd, J = 7.7, 1.5 Hz, 1H), 7.11 (dt, J = 7.3, 1.2 Hz, 1H), 7.05 (t, J = 7.3, 1.2 Hz, 1H), 6.96 (m, 1H), 6.90 (dd, 7.7, 1.4 Hz, 1H), 6.87 (dd, 7.6, 1.1 Hz, 1H), 6.83 (m, 1H), 6.27 (m, 1H), 6.10 (m, 1H), 5.76 (dd, J = 8.0, 1.1 Hz, 1H), 5.74 (s, 1H), 5.54 (d, J = 8.0, 1.1 Hz, 1H), 1.24 (s, 3H), 1.09 (s, 3H). ^{13}C NMR (201 MHz, CD_2Cl_2, δ): 172.43, 170.59, 148.27, 147.14, 145.70, 145.56, 144.61, 143.30, 140.34, 140.06, 135.95, 135.83, 132.45, 131.67, 129.67, 128.79, 128.32, 128.31, 127.69, 127.67, 126.60, 126.41, 125.82, 125.78, 125.20, 125.09, 124.96, 124.90, 124.38, 123.31, 123.25, 123.22, 120.45, 119.85, 113.69, 112.05, 54.28, 45.25,

35.33, 32.75, 23.23. APCI-MS (m/z): [M+H]+ calcd. for $C_{50}H_{37}N_4$, 693.3018; found, 693.3061; Elemental analysis calcd. (%) for $C_{50}H_{36}N_4$: C, 86.68; H, 5.24; N, 8.09; found: C, 86.93; H, 5.38; N, 8.04. Thermal stability: glass transition temperature (T_g) = 136.1 °C.

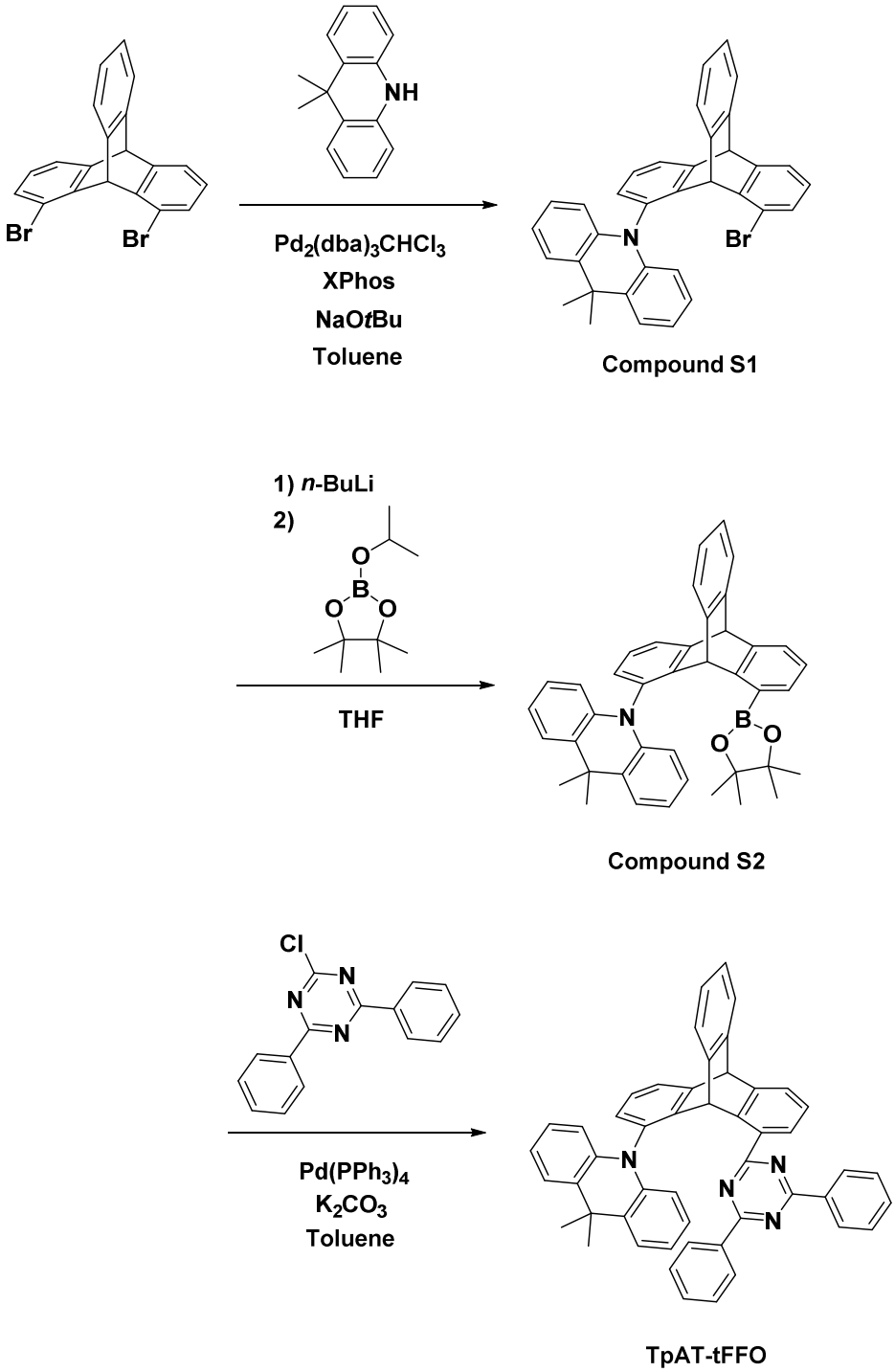

Supplementary Scheme 5.1 | Synthesis scheme for TpAT-tFFO.

Theoretical calculation

Optimization of parameters, ω for LC-ωPBE functional and γ for LCY-ωPBE functional

Optimization of the range-separation parameter, ω, for LC-ωPBE functional was performed according to ref.[2]. As shown in Supplementary Figure 4.1a, the optimal value of ω was determined from the point exhibiting minimum J^2, where $J^2 = \sum_{i=0}^{1}[\varepsilon_H(N+i) + IP(N+i)]^2$. Here, N, $\varepsilon_H(N)$, and $IP(N)$ denote the electron number of the target molecule, its HOMO energy, and vertical ionization potential, respectively. Optimization of the range parameter γ for LCY-ωPBE functional was performed by the same procedure and the results were summarized in Supplementary Figure 4.6.

Thermal and photophysical properties

General procedure for thermal measurements

Glass transition temperature (T_g) was determined from the onset of the differential scanning calorimetry (DSC) curve of the 2nd heating scan using a DSC1 (METTLER TOLEDO) at a heating rate of 10 °C min^{-1}. The 1st heating scan was conducted up to 300 °C, which is approximately 40 °C higher than the melting point of the powder sample, and the melted sample was quenched rapidly on an Al plate to form an amorphous sample.

General procedure for photophysical measurements

UV-vis absorption spectra and photoluminescence (PL) spectra were measured by a UV-vis spectrophotometer (V-750ST, JASCO, Japan) and a spectrofluorometer (FluoroMax Plus, HORIBA, Japan), respectively. Photoluminescence quantum yield (PLQY or Φ_{PL}) was measured with an absolute PLQY spectrometer (C9920-02, Hamamatsu Photonics, Japan). The PLQY values in 10^{-4} M toluene solution were collected with and without 30 min of Ar gas bubbling with an excitation wavelength of 365 nm. Here we used a toluene solvent of spectrochemical analysis grade purchased from FUJIFILM Wako Pure Chemical Corporation. The PLQYs for films were measured under a N_2 flow. The temperature-dependent transient PL decay measurements were conducted with a fluorescence lifetime measurement system (Quantaurus-Tau C11367-01, Hamamatsu Photonics, Japan) equipped with a cryostat (Oxford Instruments, Optistat DN2, UK).

Device fabrication and characterization

General procedures for OLEDs fabrication

Patterned indium-tin-oxide (ITO) substrates were cleaned by 10 min of sonication in detergent and H_2O (twice), 5 min exposure to hot steam of 2-propanol, and UV-O_3 irradiation for 30 min. Organic layers and Al cathode were deposited on the ITO substrates with a deposition apparatus (SE-4260, ALS Technology, Japan) in different chambers both at ~10^{-4} Pa. The OLEDs with active areas of 4 mm^2 were finally encapsulated with glass caps containing getter films to remove oxygen and moisture.

General procedure for device characterization

The performance of the OLEDs was characterized with an integrating sphere (C9920-12, Hamamatsu Photonics, Japan) equipped with a source meter (2400, Keithley, Japan). The device performances were measured in the forward direction in 200-meV steps.

Analysis of rate constants

In ref.[3] and subsequent publications on the analysis of TADF emitters, the value of k_{RISC} is frequently derived under the assumption that a) $k_r^T = 0$, b) $k_{nr}^T \approx 0$, c) $k_r^S \gg k_{RISC}$, and d) $k_{ISC} \gg k_{RISC}$. However, k_{RISC} in this study is very large compared to those in these preceding papers. Therefore, the assumptions c) and d) do not necessarily hold. The rate constants of TpAT-tFFO listed in the manuscript were determined without using the assumptions c) and d) as follows. Purely organic materials showing $k_{\mathrm{RISC}} \geq 10^6\ \mathrm{s}^{-1}$ are summarized in the Supplementary Table 4.3.

The time dependence of the singlet concentration $[S_1]$ and triplet concentration $[T_1]$ is described by

$$\frac{d}{dt}\begin{pmatrix}[S_1]\\ [T_1]\end{pmatrix} = \begin{pmatrix}-(k_r^S + k_{nr}^S + k_{ISC}) & k_{RISC}\\ k_{ISC} & -(k_r^T + k_{nr}^T + k_{RISC})\end{pmatrix}\begin{pmatrix}[S_1]\\ [T_1]\end{pmatrix} \qquad (1)$$

where k_r^S and k_{nr}^S are the rate constants for radiative and non-radiative decay from S_1, respectively, k_r^T and k_{nr}^T are the rate constants of radiative and non-radiative decay from T_1, respectively, and k_{ISC} and k_{RISC} are the rate constants for ISC and RISC, respectively. By solving the equations, we obtained the following equations (see ref.[4] in detail)

$$\{(k_r^S + k_{nr}^S + k_{ISC}) - k_p\}\{(k_r^T + k_{nr}^T + k_{RISC}) - k_p\} - k_{ISC}k_{RISC} = 0, \qquad (2)$$

$$\{(k_r^S + k_{nr}^S + k_{ISC}) - k_d\}\{(k_r^T + k_{nr}^T + k_{RISC}) - k_d\} - k_{ISC}k_{RISC} = 0, \qquad (3)$$

where k_p and k_d are the rate constants of the prompt and the delayed emission components, respectively. When $k_p \neq k_d$, the following equations are obtained by subtracting and adding

equations (2) and (3):

$$k_p + k_d = k_r^S + k_{nr}^S + k_{ISC} + k_r^T + k_{nr}^T + k_{RISC}, \tag{4}$$

$$k_p k_d = (k_r^S + k_{nr}^S + k_{ISC})(k_r^T + k_{nr}^T + k_{RISC}) - k_{ISC}k_{RISC}. \tag{5}$$

The total PLQY (Φ_{PL}) is the sum of the prompt ($\Phi_{\mathrm{PL}}{}^{\mathrm{p}}$) and delayed ($\Phi_{\mathrm{PL}}{}^{\mathrm{d}}$) components, and $\Phi_{\mathrm{PL}}{}^{\mathrm{d}}$ in PL experiments is given as

$$\Phi_{\mathrm{PL}}{}^{\mathrm{d}} = (\Phi_{ISC}\Phi_{RISC})\Phi_{\mathrm{PL}}{}^{\mathrm{p}} + (\Phi_{ISC}\Phi_{RISC})^2\Phi_{\mathrm{PL}}{}^{\mathrm{p}} + (\Phi_{ISC}\Phi_{RISC})^3\Phi_{\mathrm{PL}}{}^{\mathrm{p}} + \cdots$$

$$= \Phi_{\mathrm{PL}}{}^{\mathrm{p}} \sum_{k=1}^{\infty} (\Phi_{ISC}\Phi_{RISC})^k = \Phi_{\mathrm{PL}}{}^{\mathrm{p}} \frac{\Phi_{ISC}\Phi_{RISC}}{1 - \Phi_{ISC}\Phi_{RISC}}. \tag{6}$$

From equations (5) and (6),

$$\frac{k_p k_d}{k_{ISC}k_{RISC}} = \frac{(k_r^S + k_{nr}^S + k_{ISC})(k_r^T + k_{nr}^T + k_{RISC})}{k_{ISC}k_{RISC}} - 1$$

$$= \frac{1}{\Phi_{ISC}\Phi_{RISC}} - 1 = \frac{\Phi_{\mathrm{PL}}{}^{\mathrm{p}}}{\Phi_{\mathrm{PL}}{}^{\mathrm{d}}}. \tag{7}$$

Under the assumptions of a) and b), equations (4) and (5) can be reduced to

$$k_p + k_d \approx k_r^S + k_{nr}^S + k_{ISC} + k_{RISC}, \tag{8}$$

$$k_p k_d \approx (k_r^S + k_{nr}^S)k_{RISC}. \tag{9}$$

From equations (7) – (9), k_{RISC} can be expressed as follows.

$$k_{RISC}{}^2 - (k_p + k_d)k_{RISC} + k_p k_d \left(1 + \frac{\Phi_{\mathrm{PL}}{}^{\mathrm{d}}}{\Phi_{\mathrm{PL}}{}^{\mathrm{p}}}\right) \approx 0 \tag{10}$$

$$k_{RISC} \approx \frac{(k_p + k_d)}{2} \pm \sqrt{\left(\frac{k_p + k_d}{2}\right)^2 - k_p k_d \left(1 + \frac{\Phi_{\mathrm{PL}}{}^{\mathrm{d}}}{\Phi_{\mathrm{PL}}{}^{\mathrm{p}}}\right)} \tag{11}$$

All the values in the right side of equation (11), k_p, k_d, $\Phi_{\mathrm{PL}}{}^{\mathrm{p}}$, and $\Phi_{\mathrm{PL}}{}^{\mathrm{d}}$, are obtained from transient PL experiments and PLQY measurements (see Supplementary Table 4.2). The value of k_{ISC} is obtained from equation (7) using experimental data and the calculated k_{RISC} from equation (11). The value of $k_r^S + k_{nr}^S$ is obtained from equation (9), experimental data, and the calculated k_{RISC}. Finally, the values of k_r^S and k_{nr}^S are obtained using total PLQY, Φ_{PL}.

Results

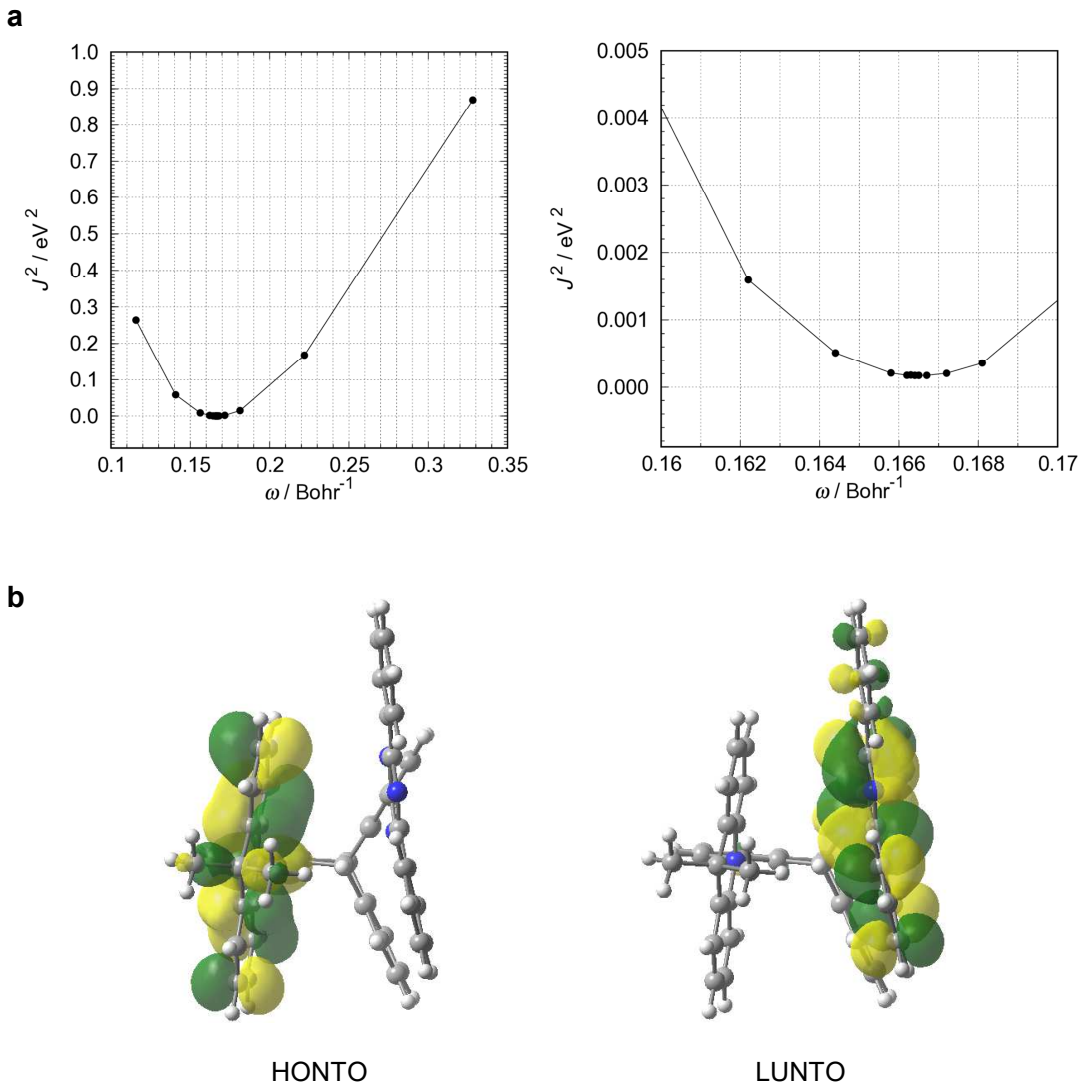

Supplementary Figure 4.1 | Theoretical calculation of TpAT-tFFO. a, J^2-ω plot of TpAT-tFFO for LC-ωPBE functional with 6-31+G(d) basis set. The minimum region of the left figure is enlarged in the right. **b,** Natural transition orbitals (NTO) of S_1 state of TpAT-tFFO. The spatial distributions of the highest occupied NTO (HONTO) and lowest unoccupied NTO (LUNTO) indicate a through-space interaction of the donor and acceptor.

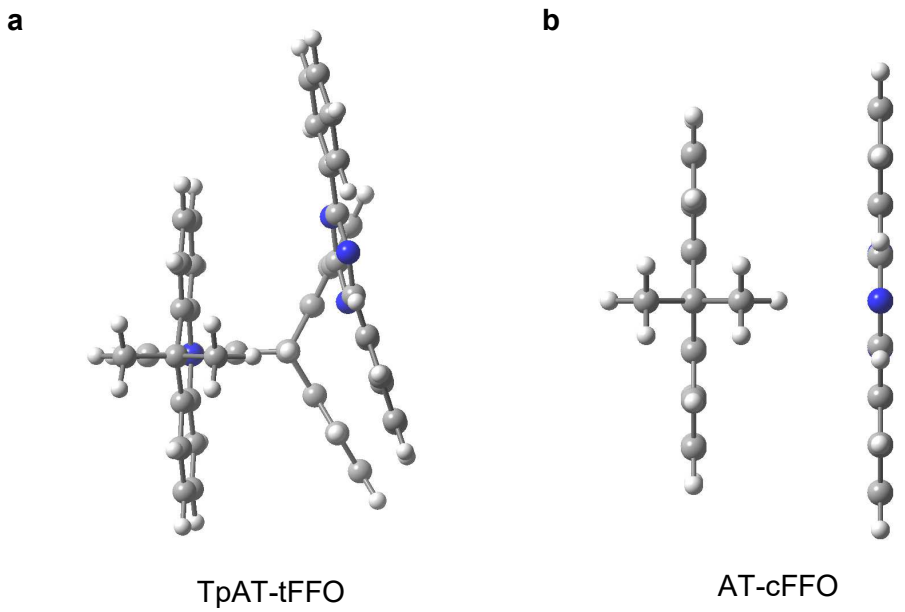

Supplementary Figure 4.2 | Geometric structures. a, TpAT-tFFO and **b**, AT-cFFO (in **b**, π-planes of A and T segments are in a completely parallel alignment with d_{DA} of 4.72 Å).

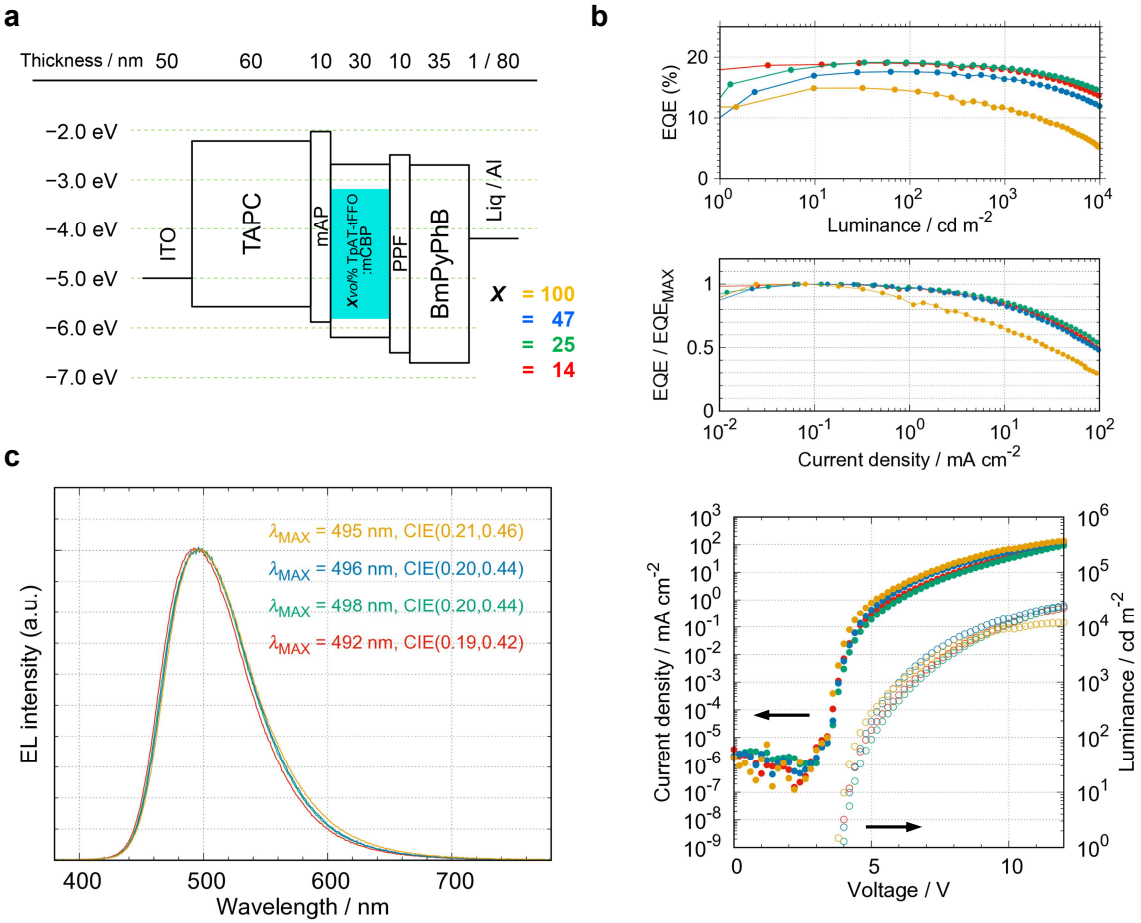

Supplementary Figure 4.3 | TpAT-tFFO based TADF-OLEDs. a, Device structure of the OLEDs. **b**, Device performances of EQE-luminance (top), normalized EQE-current density (middle), and current density-voltage-luminance characteristics (bottom). Normalized EQE is EQE/EQE_{MAX}. **c,** EL spectra of the OLEDs at 10 mA cm^{-2}. The results of OLEDs with doping concentrations of 14, 25, 47 and 100 vol% were represented by red, green, blue and yellow, respectively.

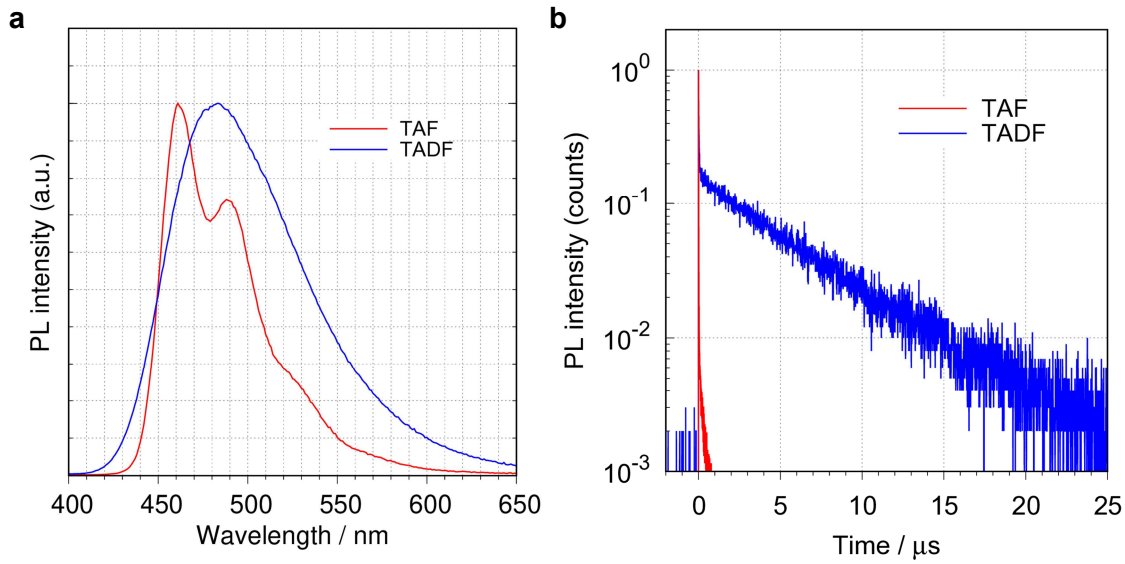

Supplementary Figure 4.4 | Photophysical propety. a, PL spectra and **b,** transient PL decay curves of 4 vol%TBPe:26 vol%TpAT-tFFO:CzSi film (TAF) and 25 vol%TpAT-tFFO:CzSi film (TADF). The PL intensities of the transient PL decay curves were monitored at 460 nm and 478 nm, respectively.

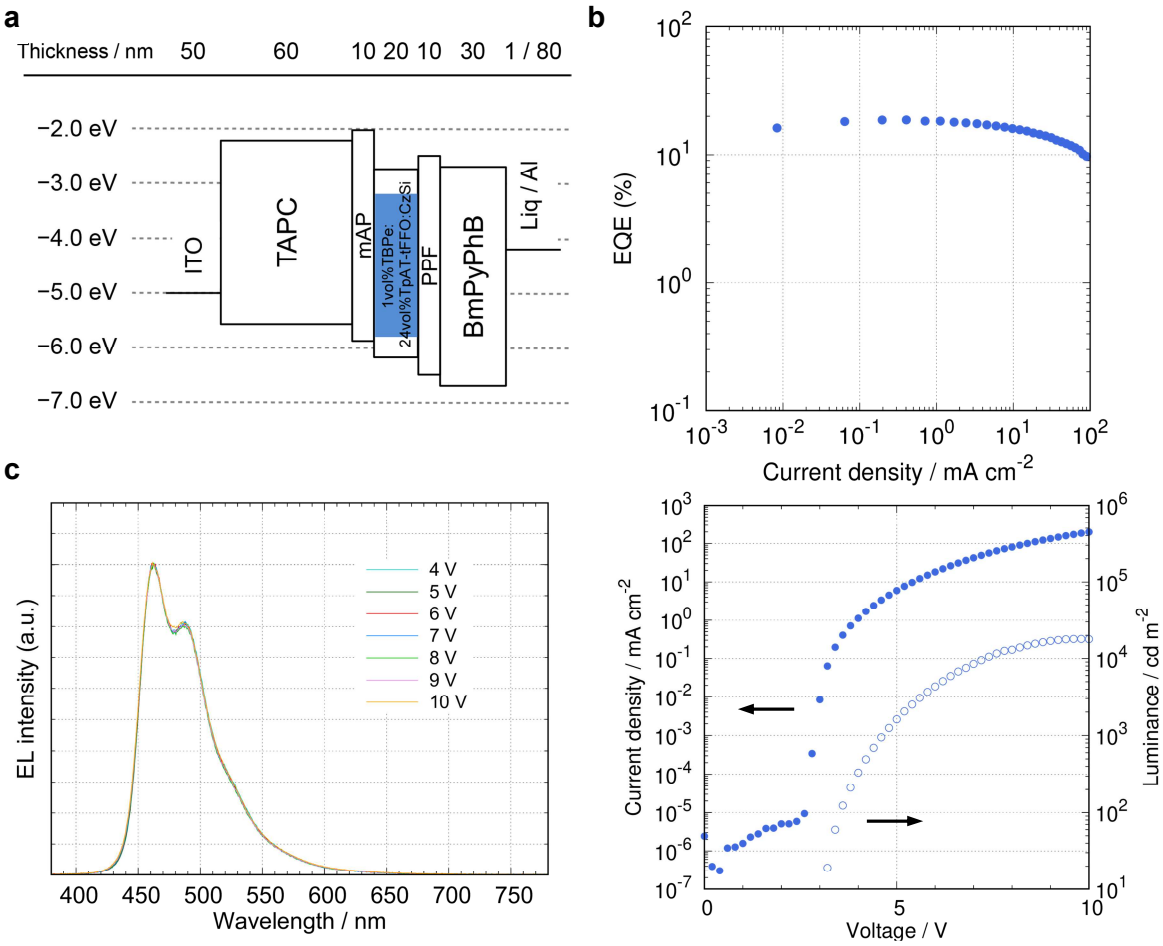

Supplementary Figure 4.5 | TpAT-tFFO based TAF-OLED using 1 vol%TBPe:24 vol%TpAT-tFFO:CzSi as an emitting layer. a, Device structure of the TAF-OLED. **b,** Device performances of EQE-current density (top) and current density-voltage-luminance characteristics (bottom). **c,** EL spectra of the TAF-OLEDs at different voltages.

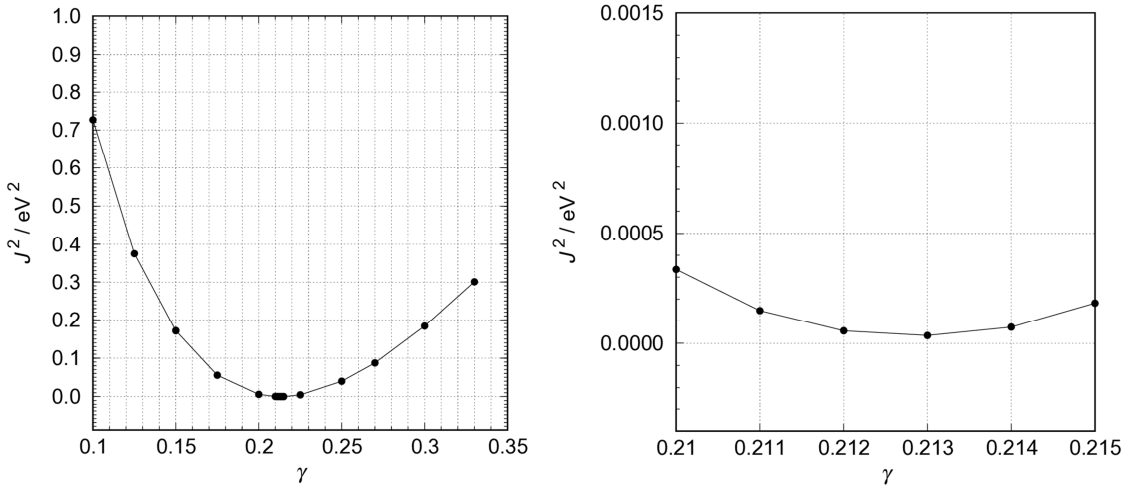

Supplementary Figure 4.6 | J^2-γ plot of TpAT-tFFO for LCY-ωPBE functional with TZP basis set. Region near the minimum J^2 in the left figure is enlarged on the right.

Supplementary Table 4.1 | Results of TD-DFT calculation of TpAT-tFFO (LC-ωPBE functional with 6-31+G(d) basis set with the optimal ω of 0.1664 Bohr^{-1}).

HOMO / eV	LUMO / eV	T_1 / eV	S_1 / eV	ΔE_{ST} / eV	$f(S_0 \rightarrow S_1)$	$\Delta E(^3CT \rightarrow ^3LE)$ / eV	$\Delta E(^3LE \rightarrow ^1CT)$ / eV
−6.47	−0.90	3.10	3.12	0.0186	0.004	0.0751	−0.0565

Supplementary Table 4.2 | Fitting data for transient PL decay curves and PLQYs of the 10^{-4} M toluene solution of TpAT-tFFO without and with 30-min Ar gas bubbling. PL decay curves were fitted by the equation, $[\text{PL intensity}] = A_p \exp\left(-\frac{t}{\tau_p}\right) + A_d \exp\left(-\frac{t}{\tau_d}\right)$. Here, A and τ denote the prefactor and lifetime, respectively. Subscripts p and d correspond to prompt and delayed components, respectively. Φ_{total}, Φ_p and Φ_d denote the PLQY of total, prompt and delayed components, respectively.

Ar bubbling	τ_p / ns	τ_d / μs	A_p	A_d	Φ_{total}	Φ_p	Φ_d
Without (w/o)	9.93	—	78.3	—	1.8	1.8 (100%)[a]	—
With (w/)	15.3	4.42	60.2	8.70	84	2.0 (2.33%)	82.0 (97.7%)

[a]Percentages in relation to the total PLQY was shown in parentheses.

Supplementary Table 4.3 | Summary of the purely organic materials with $k_{RISC} \geq 10^6$ s^{-1}. Data are collected from journal articles where the respective materials were first reported. Materials composed only of H, C, and N are highlighted in sky-blue. Inclusion of sulphur in our tFFO-based materials will provide much larger k_{RISC} values.

Emitter	Composed of	k_{RISC} ($\times 10^6$ s^{-1})	References
TpAT-tFFO	H, C, N	**12**	**This work**
Ac3TRZ3	H, C, N	1.0	Wang *et al.*, *Chem. Sci.* (2019)[5]
TAc3TRZ3	H, C, N	2.1	
2Cz3DPhCzBN	H, C, N	1.0	Noda *et al.*, *Sci. Adv.* (2018)[6]
PCzATD5	H, C, N	2.0	Wang *et al.*, *J. Mater. Chem. C* (2018)[7]
DTRZ-DI	H, C, N	1.6	Kim *et al.*, *J. Mater. Chem. C* (2018)[8]
TRZ-DI	H, C, N	1.6	
4CzIPN	H, C, N	~1.3	Uoyama *et al.*, *Nature* (2012)[9]
TRZ-m-ACRSA	H, C, N, **O**	1.2	Gan et al., Adv. Funct. Mater. (2019)[10]
DMF-BP-PXZ	H, C, N, **O**	1.0	Guo *et al.*, *Adv. Sci.* (2019)[11]
DPF-BP-PXZ	H, C, N, **O**	1.2	
SBF-BP-PXZ	H, C, N, **O**	1.1	
DPxBn	H, C, N, **O**	1.6	Kim *et al.*, *J. Phys. Chem. C* (2018)[12]
MCz-XT	H, C, N, **O**	~ 2	Lee *et al.*, *Adv. Mater.* (2017)[13]
DC-ACR	H, C, N, **O**	2.6	Chen *et al.*, *J. Mater. Chem. C* (2017)[14]
BTH-DMF	H, C, N, **S**	2.8	Liu *et al.*, *Adv. Opt. Mater.* (2018)[15]
TDBA-DI	H, C, N, **B, O**	1.1	Ahn *et al.*, *Nat. Photon.* (2019)[16]
MPAc-BO	H, C, N, **B, O**	1.0	Park *et al.*, *Adv. Funct. Mater.* (2018)[17]
TB-3PXZ	H, C, N, **B, O**	1.9	Liu *et al.*, *J. Mater. Chem. C* (2016)[18]
2	H, C, N, **B, S**	3.2	Matsuo and Yasuda, *Chem. Commun.* (2019)[19]
MPAc-BS	H, C, N, **B, S**	3.5	Park *et al.*, *Adv. Funct. Mater.* (2018)[17]
TAT-3DBTO$_2$ [a]	H, C, N, **O, S**	0.092–15[a]	dos Santos *et al.*, *Adv. Sci.* (2018)[20]
Cop-50	H, C, N, **O, S**	2.6	Liu *et al.*, *Macromolecules* (2018)[21]
Cop-10	H, C, N, **O, S**	1.4	
DPTZ-DBTO$_2$	H, C, N, **O, S**	1.9 ± 0.1	Dias *et al.*, *Adv. Sci.* (2016)[22]
BrPPM	H, C, N, **O, Br**	1.0	Xiang *et al.*, *J. Mater. Chem. C* (2017)[23]
2F-BTH-DMF	H, C, N, **F, S**	2.4	Liu *et al.*, *Adv. Opt. Mater.* (2018)[15]
MFAc-SPS	H, C, N, **P, S**	1.9	Lee *et al.*, *J. Mater. Chem. C* (2018)[24]
PTZ-mPYRCl	H, C, N, **S, Cl**	2.0	Serevicius *et al.*, *Chem. Commun.* (2019)[25]
MFAc-SPO	H, C, N, **O, P, S**	1.1	Lee *et al.*, *J. Mater. Chem. C* (2018)[24]

All the values in this table were rounded to no more than two significant figures.
[a] For TAT-3DBTO$_2$, k_{RISC} values are displayed as a range because the delayed fluorescence of TAT-3DBTO$_2$ was fitted with three exponential curves, resulting in three k_{RISC} values of different orders. The k_{RISC} values were widely distributed over more than two orders of magnitude and the average value is much smaller than the highest value.

Supplementary Table 4.4 | Device performance of OLEDs with device structures: ITO (50 nm)/TAPC (60 nm)/mAP (10 nm)/*X* vol% TpAT-tFFO:mCBP (30 nm)/PPF (10 nm)/BmPyPhB (35 nm)/Liq (1 nm)/Al (80 nm).

dopant conc. ***X*** (vol%)	EQE_{MAX}	EQE_{1000}	$EQE_{10,000}$	$EQE_{20,000}$
14	19.0	17.8	13.3	9.9
25	**19.2**	**18.1**	**14.4**	**11.7**
47	17.6	16.3	11.7	8.8
100	14.9	11.4	4.7	—

Supplementary References

[1] O. Grossman and D. Gelman, *Org. Lett.* **2006**, *8*, 1189.

[2] H. Sun, C. Zhong and J. L. Brédas, *J. Chem. Theory. Comput.* **2015**, *11*, 3851.

[3] K. Goushi, K. Yoshida, K. Sato and C. Adachi, *Nat. Photon.* **2012**, *6*, 253.

[4] H. Kaji, H. Suzuki, T. Fukushima, K. Shizu, K. Suzuki, S. Kubo, T. Komino, H. Oiwa, F. Suzuki, A. Wakamiya, Y. Murata and C. Adachi, *Nat. Commun.* **2015**, *6*, 8476.

[5] X. Wang, S. Wang, J. Lv, S. Shao, L. Wang, X. Jing and F. Wang, *Chem. Sci.* **2019**, *10*, 2915.

[6] H. Noda, H. Nakanotani and C. Adachi, *Sci. Adv.* **2018**, *4*, eaao6910.

[7] Y. Wang, Y. Zhu, X. Lin, Y. Yang, B. Zhang, H. Zhan, Z. Xie and Y. Cheng, *J. Mater. Chem. C* **2018**, *6*, 568.

[8] K. J. Kim, G. H. Kim, R. Lampande, D. H. Ahn, J. B. Im, J. S. Moon, J. K. Lee, J. Y. Lee, J. Y. Lee and J. H. Kwon, *J. Mater. Chem. C* **2018**, *6*, 1343.

[9] H. Uoyama, K. Goushi, K. Shizu, H. Nomura and C. Adachi, *Nature* **2012**, *492*, 234.

[10] L. Gan, Z. Xu, Z. Wang, B. Li, W. Li, X. Cai, K. Liu, Q. Liang and S. J. Su, *Adv. Funct. Mater.* **2019**, *29*.

[11] J. Guo, J. Fan, L. Lin, J. Zeng, H. Liu, C. K. Wang, Z. Zhao and B. Z. Tang, *Adv. Sci.* **2019**, *6*, 1801629.

[12] H. S. Kim, H. Park, S.-R. Park, S. H. Lee, Y. Ahn, Y. S. Lee and M. C. Suh, *J. Phys. Chem. C* **2018**, *122*, 28576.

[13] J. Lee, N. Aizawa, M. Numata, C. Adachi and T. Yasuda, *Adv. Mater.* **2017**, *29*, 1604856.

[14] D. Chen, X. Cai, X.-L. Li, Z. He, C. Cai, D. Chen and S.-J. Su, *J. Mater. Chem. C* **2017**, *5*, 5223.

[15] J. Liu, Z. Li, T. Hu, X. Wei, R. Wang, X. Hu, Y. Liu, Y. Yi, Y. Yamada‐Takamura, Y. Wang and P. Wang, *Adv. Opt. Mater.* **2018**, *7*, 1801190.

[16] D. H. Ahn, S. W. Kim, H. Lee, I. J. Ko, D. Karthik, J. Y. Lee and J. H. Kwon, *Nat. Photon.* **2019**, *13*, 540.

[17] I. S. Park, K. Matsuo, N. Aizawa and T. Yasuda, *Adv. Funct. Mater.* **2018**, *28*, 1802031.

[18] Y. Liu, G. Xie, K. Wu, Z. Luo, T. Zhou, X. Zeng, J. Yu, S. Gong and C. Yang, *J. Mater. Chem. C* **2016**, *4*, 4402.

[19] K. Matsuo and T. Yasuda, *Chem. Commun.* **2019**, *55*, 2501.

[20] P. L. dos Santos, J. S. Ward, D. G. Congrave, A. S. Batsanov, J. Eng, J. E. Stacey, T. J. Penfold, A. P. Monkman and M. R. Bryce, *Adv. Sci.* **2018**, *5*, 1700989.

[21] Y. Liu, Y. Wang, C. Li, Z. Ren, D. Ma and S. Yan, *Macromolecules* **2018**, *51*, 4615.

[22] F. B. Dias, J. Santos, D. R. Graves, P. Data, R. S. Nobuyasu, M. A. Fox, A. S. Batsanov, T. Palmeira, M. N. Berberan-Santos, M. R. Bryce and A. P. Monkman, *Adv. Sci.* **2016**, *3*, 1600080.

[23] Y. Xiang, Y. Zhao, N. Xu, S. Gong, F. Ni, K. Wu, J. Luo, G. Xie, Z.-H. Lu and C. Yang, *J. Mater. Chem. C* **2017**, *5*, 12204.

[24] J. Lee, N. Aizawa and T. Yasuda, *J. Mater. Chem. C* **2018**, *6*, 3578.

[25] T. Serevicius, R. Skaisgiris, J. Dodonova, L. Jagintavicius, J. Bucevicius, K. Kazlauskas, S. Jursenas and S. Tumkevicius, *Chem. Commun.* **2019**, *55*, 1975.

Chapter 5

Efficient Direct Reverse Intersystem Crossing between Charge Transfer-Type Singlet and Triplet States in Purely Organic Molecule

5.1. Introduction

In the field of organic electronics, triplet exciton harvesting is the critical problem to achieve highly efficient organic light-emitting diodes (OLEDs) and there are mainly three ways for its solution: phosphorescence, triplet fusion, and thermally activated delayed fluorescence (TADF). Phosphorescent materials can emit photons from triplet state, however, the emitters requires unevenly distributed expensive metal sources such as Ir and Pt to achieve the spin-flip transition from the triplet state to the singlet state [1]. In contrast, triplet fusion does not require any metal atom and generates one singlet exciton from two triplet excitons, and based on the system materials fluoresce from singlet state. This process, however, harvests triplet excitons only up to 50% as photon [2]. On the contrary, TADF is a promising pathway to harvest 100% triplet excitons into light within purely organic molecular framework. The triplet excitons are converted into singlet excitons through reverse intersystem crossing (RISC) and decay radiatively from singlet, resulting in delayed fluorescence. The RISC is effectively triggered by thermal energy. These advantages of low cost material design and high triplet conversion efficiency makes TADF materials promising for emitters of OLEDs and the development of efficient TADF emitters has been vigorously investigated [3].

In the early stage of the development of TADF materials, main concern was to realize negligibly small energy splitting between lowest singlet excited state (S_1) and lowest triplet state (T_1), usually termed as ΔE_{ST}, to achieve efficient RISC. This is because the spin-mixing coefficient (λ) between the singlet and triplet states is inversely proportional to ΔE_{ST} [4] as shown in following equation (1). Here SOCMEV denotes spin-orbit coupling matrix element value between S_1 and T_1.

$$\lambda = \frac{\mathrm{SOCMEV}}{\Delta E_{\mathrm{ST}}} \quad (1)$$

As a molecular structure, largely twisted donor-acceptor (D-A) systems have found out to be promising to achieve small ΔE_{ST}, because twisted D-A structure separates frontier molecular orbitals and makes S_1 and T_1 as near-degenerate charge transfer (CT) states. This D-A molecular framework have well succeeded in realizing efficient TADF materials and TADF OLEDs [5-7]. Recently, however, it has been pointed out that such largely twisted systems have vanishingly small λ due to small H_{SO}. In fact, such largely twisted systems with CT singlet and triplet states (e.g. ^{1}CT and ^{3}CT, respectively) are likely to possess vanishingly small SOCMEV. This argument was supported by the El-Sayed's rule where he mentioned *"no spin-orbit coupling between singlet and triplet states of the same configuration"* [8]. Accordingly, several groups have theoretically predicted that inclusion of any other triplet state of different configuration (e.g. locally excited (LE) triplet state (^{3}LE)) should be responsible for the efficient RISC process [9-13], and was partly experimentally proven to be the case [11, 14-17]. These reports imply that emitters originally being expected to experience RISC between ^{1}CT and ^{3}CT states are likely to go through any closely lying triplet state such as ^{3}LE. Contrarily, we have previously reported a largely twisted D-A type blue emitter named MA-TA (Figure 5.1A), which exhibited high performance with photoluminescence quantum yield (PLQY, or Φ_{PL}) of 99% and relatively fast TADF lifetime ~18 μs, even though there exist no other triplet state close to ^{1}CT and ^{3}CT [18]. Also, MA-TA consists only of carbon, hydrogen, and nitrogen and therefore heavy metal atom effect cannot be expected. The situation appear to be incompatible with the above mentioned RISC scheme, where the inclusion of any other close-lying triplet state different from the above mentioned CT states is necessary [19].

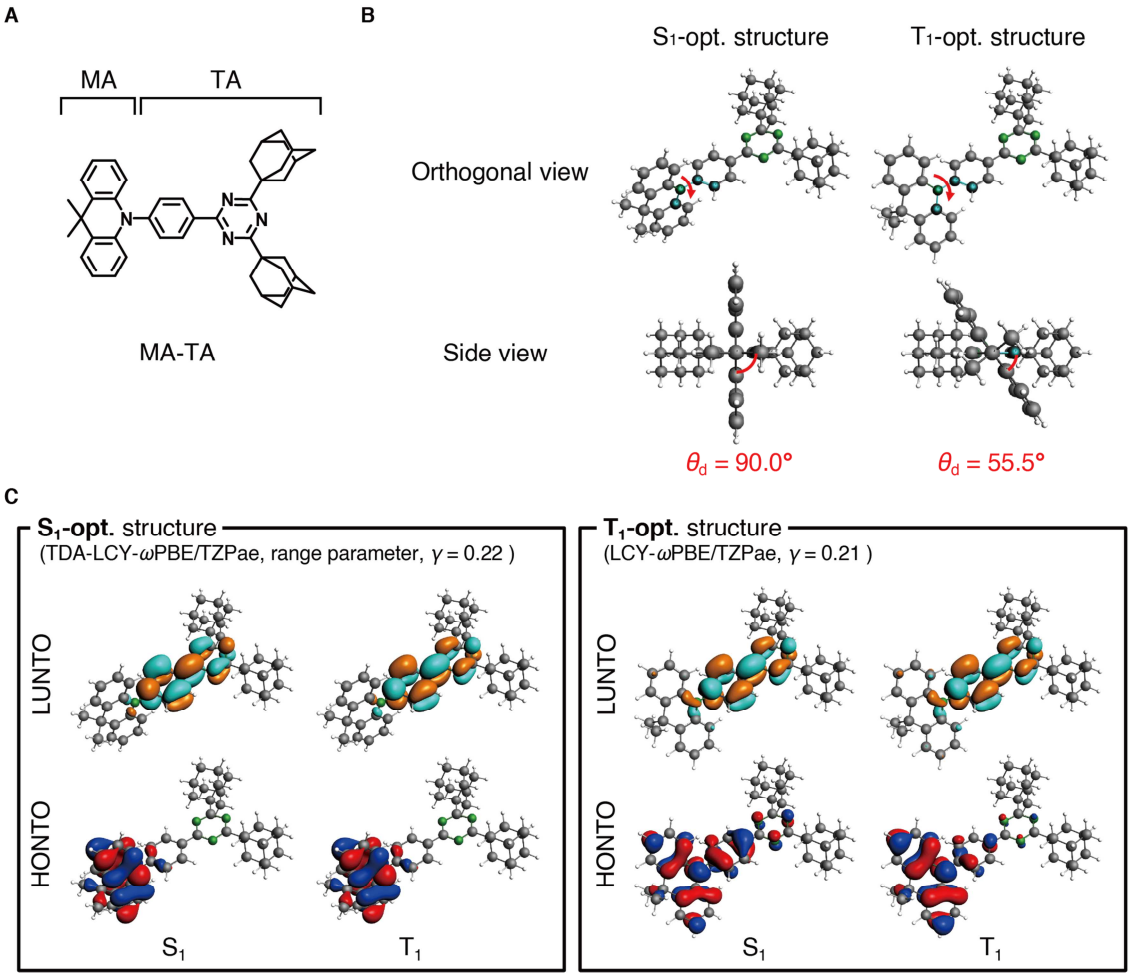

Figure 5.1. Molecular structure of MA-TA. (**A**) Chemical structure of MA-TA. (**B**) Geometries of MA-TA at S_1 and T_1 states optimized by TDA-DFT and DFT, respectively. LCY-ωPBE/TZPae level of theory with range parameter, γ = 0.22 for S_1, and γ = 0.21 for T_1 were used. (**C**) NTOs of MA-TA for S_1 and T_1 states both at the S_1- (on the left) and T_1-opt. structures (on the right).

These investigations motivated us to examine the RISC process of MA-TA. In this paper, we performed quantum chemical calculation to estimate the rate constant of RISC (k_{RISC}), which revealed that MA-TA is expected to possess relatively large k_{RISC} ranging from 10^5 to 10^6 s^{-1} directly between CT-type singlet and triplet states. Certainly, k_{RISC} was calculated to be 0 and thus RISC is strictly forbidden when D and A of MA-TA is in the S_1-optimized (S_1-opt.) structure, which corresponds to largely twisted (perpendicular) structure, but the high k_{RISC} is achievable when the torsion angle between the D and A is slightly deviated from perpendicular. We will discuss in more detail later, and such geometry corresponds to the intermediate structure between those of S_1 and T_1 from the viewpoint of torsion angle. This result indicates that the high k_{RISC} could be dynamically probable during the structural fluctuation between the excited states. In this context, we have also experimentally investigated the RISC process of MA-TA, where the energy level diagram is ^{3}LE >> ^{1}CT ~ ^{3}CT, by expecting that higher lying ^{3}LE state is not involved in the RISC process. Here, we investigated host effect on TADF property of MA-TA. Several groups have experimentally reported that the host polarity and/or polarizability change the relative energy difference between the ^{1}CT and ^{3}LE, which severely influenced the TADF performance both in photoluminescence (PL) and electroluminescence (EL) [20-22]. While the ^{1}CT and ^{3}LE states of those reported emitters are closely lying in the order of ^{1}CT > ^{3}LE in energy level, the situation is different in MA-TA; we expected negligible influence of host materials on PL and EL performance. As we expected, MA-TA was experimentally found to possess the energy diagram of ^{3}LE >> ^{1}CT ~ ^{3}CT (this being consistent with theoretical calculation), and exhibited efficient TADF in various host materials. Furthermore, in its application to OLEDs, MA-TA exhibited EQE ~ 20% irrespective of host matrices. These results indicated that MA-TA experiences efficient direct RISC between CT-type singlet and triplet states and thereby the TADF performance of MA-TA was negligibly

affected by the host choice. Here, please note that our results do not contradict to the molecular design, where involvement of any different configuration such as ^{3}LE state **"accelerates"** the RISC process.

5.2. Results and discussion

Quantum chemical calculation

Figure 5.1B shows density functional theory (DFT) and Tamm-Dancoff approximation (TDA)-DFT optimized T_1 and S_1 structure of MA-TA performed by Amsterdam Density Functional (ADF) [23] and the main difference between them was seen in the dihedral angle (θ_d) of D-A connecting position as indicated by red arrows. For the calculation, LCY-ωPBE/TZPae level of theory with optimal range separation parameter, γ = 0.21 for T_1 and 0.22 for S_1 were used. The determination of optimal γ was detailed in Supplementary Figure 5.1. At the S_1-opt. structure, dihedral angle (colored red in Figure 5.1B) between MA (donor fragment) and TA (acceptor fragment) was 90.0° and π-planes of MA and TA were almost perpendicular to each other, while θ_d at T_1-opt. structure resulted in 55.5°. We then calculated excitation energies of MA-TA on both S_1- and T_1-opt. structures by TDA-DFT (Supplementary Table 5.1). As shown in Figure 5.1C, natural transition orbital (NTO) analysis revealed that at the S_1-opt. structure, S_1 and T_1 were similar CT states where highest occupied NTO (HONTO) and lowest unoccupied NTO (LUNTO) was substantially localized on donor and acceptor fragment, respectively. This was also the case with T_1-opt. structure except that HONTOs are slightly delocalized into acceptor fragments. Such delocalization is sometimes regarded as a formation of hybridized local and CT (HLCT) excited state [24]. Consequently, while the energy differences between S_1 and T_1 (ΔE_{ST}) was very small (9.9 meV) at the S_1-opt. structures, relatively large ΔE_{ST} of 445.9 meV was obtained at the T_1-opt. structure (Supplementary Table 5.1). This larger ΔE_{ST} at the T_1-opt. structure was due to larger overlap between HONTO and LUNTO. Whereas, S_n and T_n (n = 2,3,4,…) lied more than 500 meV higher in energy than that of S_1 state and hardly expected to participate in the RISC process. The most important finding is that the HONTOs of S_1 and T_1 are delocalized into acceptor fragments to a different extent, which results in different HLCT

singlet and triplet states at T_1-opt. structure even though the states are substantially similar CT-type states. Considering above mentioned energy diagram and similar (but different) nature of CT-type S_1 and T_1 states, we reasonably expect direct RISC between S_1 and T_1.

Since drastic geometrical change was observed between the S_1- and T_1-opt. structures in especially for the dihedral angle, we investigated the effect of the dihedral angle change on RISC efficiency. We computed ΔE_{ST} and spin-orbit coupling matrix element value (SOCMEV) at each θ_d (every 2° from 50° to 90°) and then calculated the rate constant of RISC (k_{RISC}) using following equation (2) and (3) according to the Refs. [25] and [26].

$$k_{RISC} = \frac{2\pi}{\hbar} \cdot |V_{SOC}|^2 \cdot \frac{1}{\sqrt{4\pi\lambda_M k_B T}} \cdot e^{\left(-\frac{(\Delta E_{ST}+\lambda_M)^2}{4\lambda_M k_B T}\right)} \quad (2)$$

$$|V_{SOC}|^2 = \frac{1}{3} \cdot \left|\langle S_1 | \hat{H}_{SO} | T_1 \rangle\right|^2 = \frac{1}{3} \cdot (\mathrm{SOCMEV})^2 \quad (3)$$

Reasonably assuming that temperature (T) is 300 K, we calculated k_{RISC} for the case of Marcus reorganization energy, λ_M = 0.1, 0.2 and 0.3 eV. Also, T_n and S_n energy levels were calculated and confirmed that these states lied always more than 500 meV higher than the S_1 states for all the θ_d as shown in Figure 5.2A. Figure 5.2B shows k_{RISC}, SOCMEV, and ΔE_{ST} of MA-TA as a function of θ_d, where only θ_d was altered from the S_1-opt. structure. ΔE_{ST} monotonically increased as θ_d got smaller, while SOCMEV reached a peak at around 65°. The behavior of SOCMEV can be explained as follows. Thereby calculated k_{RISC} was zero at θ_d = 90°, increased and topped out at around θ_d = 80°, and then turn downward as θ_d decreased. The k_{RISC} drastically changed in the order from 10^{-3} to 10^6 s^{-1}. These results indicate that efficient RISC is expected at an intermediate θ_d between the S_1- and T_1-opt. structures. Similarly, we also investigated the probability of ISC from S_1 to T_1 and S_1 to high lying ^{3}LE state (T_2) as shown in Supplementary

Figure 5.2. The rate constant of ISC from S_1 to T_1 was in the order of 10^7 s^{-1} at the most, while that from S_1 to T_2 was less than 10^0 s^{-1}. These results indicated that ISC from S_1 to T_2 was competitively too slow to take place. In short, the efficient RISC directly between substantially similar CT-singlet and CT-triplet states of MA-TA was theoretically achievable. The calculated k_{RISC} peaked ranging from 10^5 to 10^6 s^{-1} sufficiently high among the purely organic TADF materials.

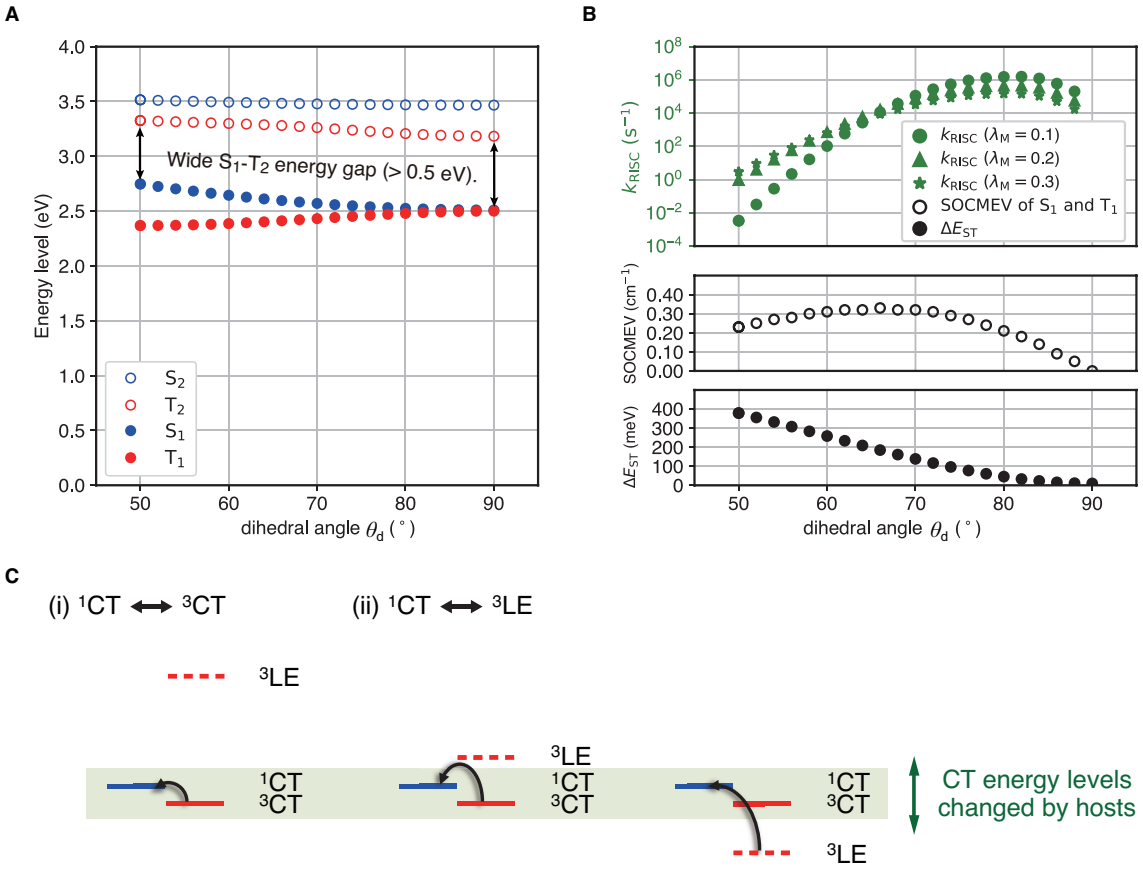

Figure 5.2. Theoretical investigation on RISC dynamics. (**A**) S_2, T_2, S_1, and T_1 energy levels of MA-TA as a function of dihedral angle (θ_d) between donor and acceptor. (**B**) k_{RISC}, SOCME, and ΔE_{ST} of MA-TA as a function of θ_d. (**C**) Schematic RISC pathway (i) without and (ii) with intervention of ^{3}LE state.

As we mentioned in the introduction, it has been previously reported that host selection brings about drastic change of photophysical properties of TADF materials, particularly PLQY and lifetime of delayed fluorescence, which in turns influences device performances [20-22]. The behavior was attributed to the change of ΔE_{ST} of the TADF materials in different host materials and the change was considered to be caused by the host polarity and/or polarizability. More specifically, those emitters in ref. [20-22] are reported to possess CT-type S_1 state and LE-type T_1 state, and the degree of energy level change for each CT and LE states differs with each other depending on host polarity and/or polarizability. Whereas, both S_1 and T_1 are expected to be similar CT-type states for the case of MA-TA and the degree of energy level change of the two states would be the same extent, which make ΔE_{ST} almost unchanged and enable efficient RISC directly between S_1 and T_1 in various host matrices. The schematic mechanisms of RISC in host materials (i) for the case of MA-TA and (ii) for the case of those TADF materials where RISC is mediated by ^{3}LE state were summarized in Figure 5.2C. These investigations motivated us to conduct PL and EL measurements of MA-TA in different host matrices.

Photophysical measurements

Before the host investigation, we experimentally verified singlet and triplet energy level diagrams of MA-TA and revealed that MA-TA possessed energy levels in the order of ^{3}LE >> ^{1}CT ≈ ^{3}CT. Photophysical measurements were conducted on the 10^{-4} M toluene solution of MA-TA and that of each donor and acceptor fragment, MA and TA, respectively. Both singlet and triplet energies were determined from the inflection points of the spectra at the high energy shoulder as shown in Figure 5.3A. From the phosphorescence spectra measured at 77 K, triplet energy of MA-TA was determined to be 2.76 eV while both MA and TA exhibited much higher triplet energy of 3.16 and 3.10 eV, respectively. Considering that the singlet energy of MA-TA was 2.78 eV from the fluorescence spectrum, the energy level diagram of MA-TA should be in the order of ^{3}LE (both over donor and acceptor) > ^{1}CT ≈ ^{3}CT, which was consistent with calculation results. Referring to the triplet energy of MA-TA, we then chose five host matrices, 1,4-bis(triphenylsilyl)benzene (UGH-2), 9-(4-tert-butylphenyl)-3,6-bis(triphenylsilyl)-9H-carbazole (CzSi), 3,3'-di(9H-carbazol-9-yl)-1,1'-biphenyl (mCBP), 2,6-Bis(9H-carbazol-9-yl)pyridine (PyD_2), and 2,8-bis(diphenylphosphoryl)dibenzo[b,d]furan (PPF), whose chemical structures are shown in Figure 5.3B. These hosts are commonly used for blue TADF and phosphorescent emitters because of their relatively high T_1 energies: UGH-2 with 3.50 eV [27], CzSi with 3.02 eV [28], mCBP with 2.81 eV [29], PyD_2 with 3.03 eV [20], and PPF with 3.1 eV [30]. Also, we intended that the HOMO and LUMO energy levels of MA-TA lie inside those of host materials as shown in Supplementary Figure 5.3 so as to avoid undesirable exciplex formation for the pure investigation of the effect of host polarity and/or polarizability on TADF performances. Figure 5.3C exhibits PL spectra of doped film of MA-TA in hosts at the emitter doping concentration of 20 vol%. PL spectra exhibited red-shift in the order of UGH-2, CzSi, mCBP, PyD_2, and PPF,

which indicates that the CT state stabilized to a different extent depending on the polarity and/or polarizability of host matrices. PL energy largely changed about 300 meV from UGH-2 to PPF. Table 5.1 and Figure 5.3D exhibit the results of PLQY and PL lifetime measurements of the doped films. On the contrary to the previous reports, MA-TA exhibited high PLQY and similar PL decay curves of delayed fluorescence irrespective of host materials. Also, experimentally determined k_{RISC} in all the host materials were 0.6–1.7×10^5 s^{-1} which shows good agreement with theoretically estimated values. Derivation of the experimental k_{RISC} was detailed in the **Supplementary Information**. These results clearly indicate that MA-TA exhibits efficient RISC in various host materials irrespective of host polarity and/or polarizability. The insensitivity of PL performance to host polarity and/or polarizability provides a wider-variety of host choices and is beneficial for the device fabrication so as to realize the best energy level matching and charge balance. For the 20 vol%MA-TA:CzSi film, we also conducted temperature dependent transient PL measurement (see Supplementary Figure 5.4) to verify the (R)ISC pathway referring to ref. [17]. From the Arrhenius plots, energetic barrier for ISC and RISC were determined to be 4.0 meV and 78.2 meV, which is much smaller than the energy gap between ^{1}CT (or ^{3}CT) and ^{3}LE of MA-TA (Figure 5.3A). This result evidences that high lying ^{3}LE states of MA-TA do not participated in the ISC and RISC.

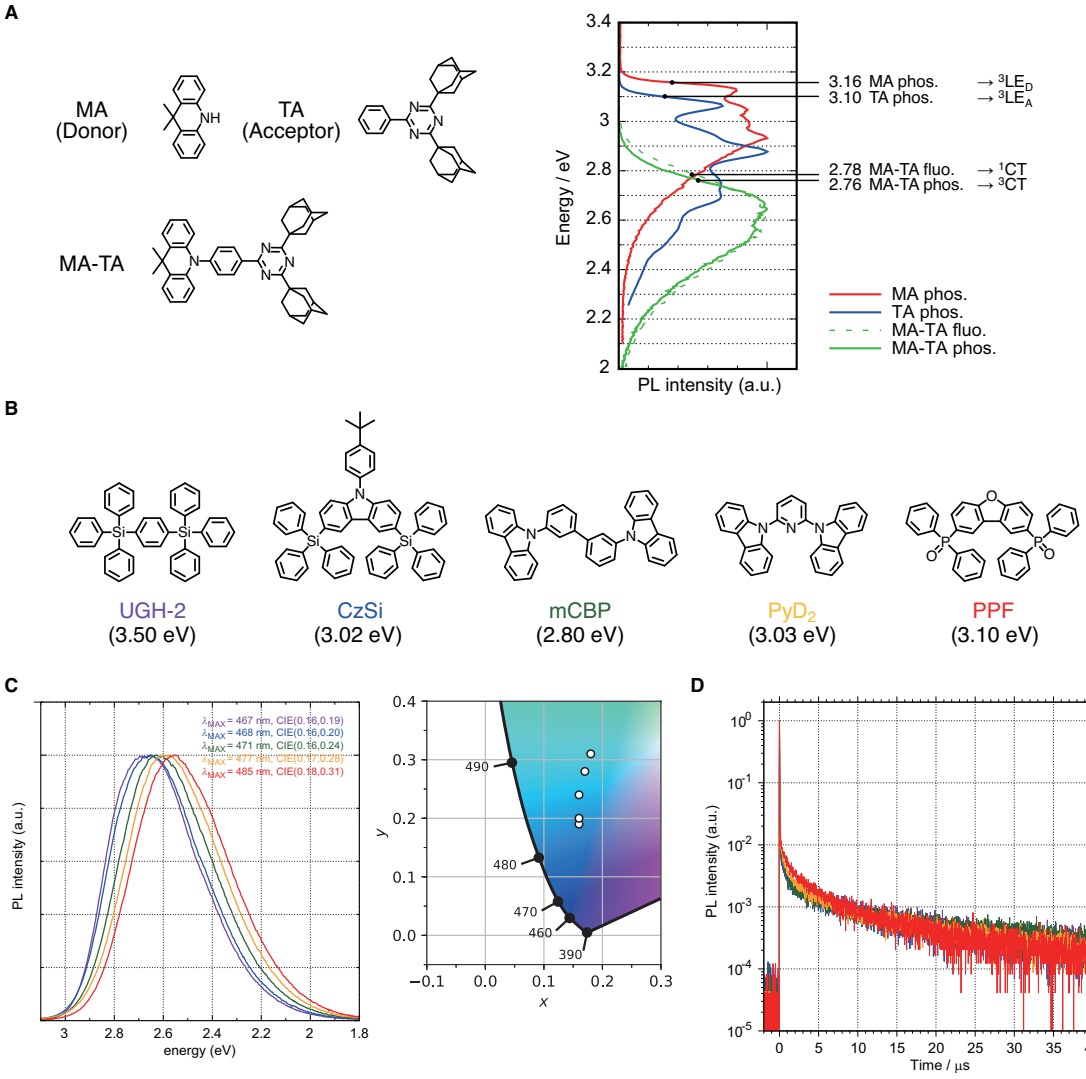

Figure 5.3. Photophysical properties of MA-TA in solution and solid states. (**A**) Chemical structures of MA, TA and MA-TA are shown on the left. Their fluorescence and phosphorescence spectra are shown on the right. $^{3}LE_{D}$ and $^{3}LE_{A}$ denotes ^{3}LE states over donor and acceptor fragment, respectively and they correspond to MA and TA fragments, respectively. (**B**) Chemical structures of host materials together with their T_1 energy in parentheses. (**C**) PL spectra and their CIE coordinates of 20 vol%MA-TA:host films. (**D**) PL decay curves of 20 vol%MA-TA:host films measured at 300 K. Emissions were observed at peak maximum wavelength of the respective films with excitation wavelength of 280 nm.

Table 5.1. PL properties of MA-TA in the doped film.

Hosts	Φ_{PL} [1] (%)	λ_{PL} (nm)	τ_p [2] (ns)	τ_d [2] [3] (μs)	k_{RISC} ($\times 10^5$ s^{-1})
UGH2	**100**	467	15.2	14.6	1.08
CzSi	**92**	468	15.4	25.8	0.65
mCBP	**78**	471	17.1	26.3	0.58
PyD_2	**83**	477	17.4	6.7	0.87
PPF	**87**	485	17.1	8.8	1.73

[1] Measured under N_2 flow with excitation wavelength of 300 nm, which correspond to the excitation wavelength of both host and emitter.

[2] Excitation wavelength of 280 nm.

[3] An average lifetime was calculated by $\tau_d = \frac{\sum A_n \tau_n^2}{\sum A_n \tau_n}$, where A_n denotes the pre-exponential factor for the τ_n.

OLED characteristics

Subsequently, we fabricated OLEDs using the doped films as emitting layers with device structures of indium-tin-oxide (ITO) (50 nm)/4,4′-cyclohexylidenebis[*N*,*N*-bis(4-methylphenyl)benzenamine] (TAPC) (60 nm)/1,3-bis(9,9-dimethylacridin-10(9*H*)-yl)benzene (mAP) (10 nm)/20 vol%MA-TA:Host (20 nm)/PPF (10 nm)/1,3-bis[3,5-di(pyridin-3-yl)phenyl]benzene (BmPyPhB) (30 nm)/lithium quinolin-8-olate (Liq) (1 nm)/Al (80 nm). The structures and performances of 20 vol%MA-TA:Host-based OLEDs are shown in Figure 5.4A–C and Table 5.2. Also, the device performances of *X* vol%MA-TA:Host-based OLEDs are summarized in Table 5.2. As expected, MA-TA exhibited maximum external quantum efficiency (EQE_{MAX}) around 20% in all the host materials with different EL emission colors similar to PL spectra. These high EQE_{MAX} values irrespective of host materials indicate that host polarity and/or polarizability do not substantially degrade device performances, which is beneficial for device optimization as we mentioned above. Contrarily, comparing the device characteristics of 20 vol%MA-TA:Host-based OLEDs (Figure 5.4A–C), the OLEDs exhibited different current density-voltage and different EQE roll-off behavior, which can be attributed to the different charge injection and transport properties of the host materials. Consequently, the choice of CzSi brought about a deep-blue and highly efficient OLED, and that of PyD_2 achieved a very bright OLED with alleviated EQE roll-off in this device structure. We also demonstrated the optimization of doping concentration using CzSi host to achieve highly efficient deep-blue TADF OLEDs, where the doping concentration of MA-TA was 4, 10, 20, 30, and 50 vol% (Figure 5.4D). The OLEDs exhibited high EQE_{MAX} of ~ 20% irrespective of doping concentration. At the doping concentration of 10 vol%, MA-TA demonstrated highest EQE_{MAX} of 23.9% and even at the practical brightness of 100 and 1,000 cd m^{-2} achieved relatively high EQE of 18.4% (EQE_{100}) and 10% ($EQE_{1,000}$),

respectively with deep-blue emission of CIE(0.15, 0.16). In this way, we can optimize the OLEDs according to purposes without concerning about the substantial EQE drop induced by host polarity and/or polarizability.

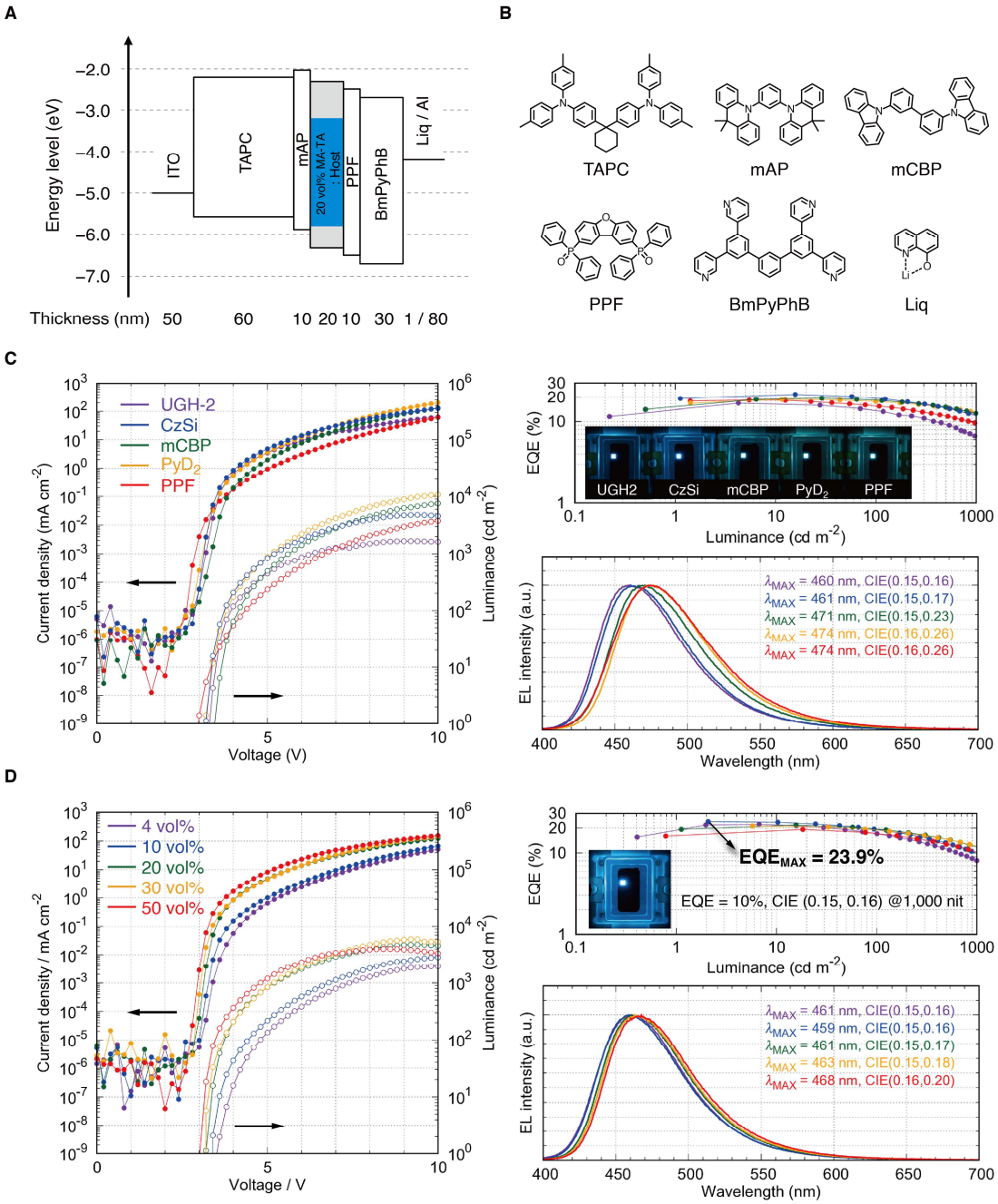

Figure 5.4. OLED performance of MA-TA. (**A**) Device structures and (**B**) materials used for the OLEDs. (**C**) Current density-voltage-luminescence (left) and EQE-luminance characteristics (upper right), and EL spectra (lower right) of OLEDs using 20 vol%MA-TA:host films as emitting layer. (**D**) Those of OLEDs using *X* vol%MA-TA:CzSi films as emitting layer, where *X* is 4, 10, 20, 30, and 50.

Table 5.2. Summary of the device performances of *X* vol% MA-TA:Host-based OLEDs with device structures of ITO (50 nm)/ TAPC (60 nm)/ mAP (10 nm)/*X* vol% MA-TA:Host (20 nm)/ PPF (10 nm)/ BmPyPhB (30 nm)/ Liq (1 nm)/ Al (80 nm).

Host	Doping conc. *X* (vol%)	EQE_{MAX} (%)	$Lum._{MAX}$ (cd m^{-2})	Power $eff._{MAX}$ (lm W^{-1})	Current $eff._{MAX}$ (cd A^{-1})	CIE(*x*,*y*)
UGH-2	20	16.9	1678	22.5	24.3	(0.15, 0.16)
	30	**18.2**	2678	28.1	28.6	(0.15, 0.18)
CzSi	4	22.1	1965	35.1	37.9	(0.15, 0.16)
	10	**23.9**	2882	28.7	31.1	**(0.15, 0.16)**
	20	21.8	4793	28.6	30.9	(0.15, 0.17)
	30	21.6	5961	30.9	31.5	(0.15, 0.18)
	50	19.2	4021	29.6	30.2	(0.16, 0.20)
mCBP	10	**19.9**	6975	35.6	29.8	(0.16, 0.24)
	20	19.5	8062	28.9	33.2	(0.16, 0.23)
PyD_2	10	18.1	9056	30.8	33.4	(0.16, 0.25)
	20	**18.8**	10990	35.2	35.9	(0.16, 0.27)
	30	17.6	10680	30.7	33.1	(0.16, 0.27)
PPF	20	**18.5**	4052	36.6	35.0	(0.16, 0.26)

5.3. Conclusion

We have theoretically and experimentally investigated the RISC process of a purely organic blue emitter, MA-TA, where ^{3}LE energy levels lie in higher energy than those of ^{1}CT and ^{3}CT with the energy diagrams of ^{3}LE >> ^{1}CT ≈ ^{3}CT. Theoretical calculation revealed that efficient RISC is achievable even directly between the similar ^{1}CT and ^{3}CT owing to the slight hybridization of different nature by change of the torsion angle between donor and acceptor fragments, even though T_n states lies at least 500 meV higher than the S_1 and T_1 states. The calculated k_{RISC} between S_1 and T_1 was ranging from 10^5 to 10^6 s^{-1}, which is in good accordance with experimental k_{RISC} of 0.6–1.8×10^5 s^{-1} for MA-TA in solid-state host matrices. Furthermore, PL performance of MA-TA showed less sensitivity to host polarity and/or polarizability compared to ordinary TADF materials, which facilitated device optimization and yielded high-performance OLEDs with EQE ~ 20% in various host materials. MA-TA provided a deep-blue TADF OLED exhibiting EQE_{MAX} = 23.9%, EQE_{100} = 18.4% and $EQE_{1,000}$ = 10% with emission color of CIE(0.15, 0.16). In this way, we revealed that TADF molecular design where emitters possess highly twisted structure with the energy diagram of ^{3}LE >> ^{1}CT ≈ ^{3}CT is also promising for efficient RISC as well as the trendy molecular design involving any other triplet state of different configuration from ^{1}CT state. We would like to note again that our results do not contradict to the molecular design, where intervention of different nature of triplet state such as ^{3}LE state **"accelerates"** the RISC process. In addition, the molecular design facilitated and expanded the host choice because the TADF performance of the emitter based on the concept likely to be less sensitive to host polarity and/or polarizability. This host insensitivity is especially effective for deep-blue OLED since the host choice for deep-blue materials is inherently limited compared to other emission colors. We believe that our theoretical and experimental investigations provide insight into RISC mechanism of TADF mateirals and that

our molecular design strategy will boost the development of deep-blue TADF materials and deep-blue TADF OLEDs.

(Chapter 5 is the Author's version of an unsubmitted work that will be submitted for publication.)

5.4. References

[1] H. Xu, R. Chen, Q. Sun, W. Lai, Q. Su, W. Huang and X. Liu, *Chem. Soc. Rev.* **2014**, *43*, 3259.

[2] D. Y. Kondakov, *Phil. Trans. R. Soc. A* **2015**, *373*, 20140321.

[3] Z. Yang, Z. Mao, Z. Xie, Y. Zhang, S. Liu, J. Zhao, J. Xu, Z. Chi and M. P. Aldred, *Chem. Soc. Rev.* **2017**, *46*, 915.

[4] H. Uoyama, K. Goushi, K. Shizu, H. Nomura and C. Adachi, *Nature* **2012**, *492*, 234.

[5] T. Nakagawa, S. Y. Ku, K. T. Wong and C. Adachi, *Chem. Commun.* **2012**, *48*, 9580.

[6] G. Mehes, H. Nomura, Q. Zhang, T. Nakagawa and C. Adachi, *Angew. Chem. Int. Ed.* **2012**, *51*, 11311.

[7] W.-L. Tsai, M.-H. Huang, W.-K. Lee, Y.-J. Hsu, K.-C. Pan, Y.-H. Huang, H.-C. Ting, M. Sarma, Y.-Y. Ho, H.-C. Hu, C.-C. Chen, M.-T. Lee, K.-T. Wong and C.-C. Wu, *Chem. Commun.* **2015**, *51*, 13662.

[8] M. A. El-Sayed, *J. Chem. Phys.* **1963**, *38*, 2834.

[9] C. M. Marian, *J. Phys. Chem. C* **2016**, *120*, 3715.

[10] J. Gibson, A. P. Monkman and T. J. Penfold, *Chemphyschem* **2016**, *17*, 2956.

[11] M. K. Etherington, J. Gibson, H. F. Higginbotham, T. J. Penfold and A. P. Monkman, *Nat. Commun.* **2016**, *7*, 13680.

[12] I. Lyskov and C. M. Marian, *J. Phys. Chem. C* **2017**, *121*, 21145.

[13] P. K. Samanta, D. Kim, V. Coropceanu and J. L. Brédas, *J. Am. Chem. Soc.* **2017**, *139*, 4042.

[14] F. B. Dias, J. Santos, D. R. Graves, P. Data, R. S. Nobuyasu, M. A. Fox, A. S. Batsanov, T. Palmeira, M. N. Berberan-Santos, M. R. Bryce and A. P. Monkman, *Adv. Sci.* **2016**, *3*, 1600080.

[15] T. Hosokai, H. Matsuzaki, H. Nakanotani, K. Tokumaru, T. Tsutsui, A. Furube, K. Nasu, H.

Nomura, M. Yahiro and C. Adachi, *Sci. Adv.* **2017**, *3*, e1603282.

[16] H. Noda, H. Nakanotani and C. Adachi, *Sci. Adv.* **2018**, *4*, eaao6910.

[17] H. Noda, X.-K. Chen, H. Nakanotani, T. Hosokai, M. Miyajima, N. Notsuka, Y. Kashima, J.-L. Brédas and C. Adachi, *Nat. Mater.* **2019**, *18*, 1084.

[18] Y. Wada, S. Kubo and H. Kaji, *Adv. Mater.* **2018**, *30*, 1705641.

[19] P. L. dos Santos, M. K. Etherington and A. P. Monkman, *J. Mater. Chem. C* **2018**, *6*, 4842.

[20] G. Méhes, K. Goushi, W. J. Potscavage and C. Adachi, *Org. Electron.* **2014**, *15*, 2027.

[21] P. L. dos Santos, J. S. Ward, M. R. Bryce and A. P. Monkman, *J. Phys. Chem. Lett.* **2016**, *7*, 3341.

[22] S.-J. Woo, Y. Kim, Y.-H. Kim, S.-K. Kwon and J.-J. Kim, *J. Mater. Chem. C* **2019**, *7*, 4191.

[23] G. te Velde, F. M. Bickelhaupt, E. J. Baerends, C. Fonseca Guerra, S. J. A. van Gisbergen, J. G. Snijders and T. Ziegler, *J. Comput. Chem.* **2001**, *22*, 931.

[24] W. Li, Y. Pan, L. Yao, H. Liu, S. Zhang, C. Wang, F. Shen, P. Lu, B. Yang and Y. Ma, *Adv. Opt. Mater.* **2014**, *2*, 892.

[25] H. Sun, C. Zhong and J. L. Brédas, *J. Chem. Theory. Comput.* **2015**, *11*, 3851.

[26] ADF Thermally Activated Delayed Flourescence (TADF), https://www.scm.com/doc/Tutorials/Advanced/ADF_optimizing_TADF_emission.html (accessed 1st December 2019).

[27] X. Ren, J. Li, R. J. Holmes, P. I. Djurovich, S. R. Forrest and M. E. Thompson, *Chem. Mater.* **2004**, *16*, 4743.

[28] M.-H. Tsai, H.-W. Lin, H.-C. Su, T.-H. Ke, C.-C. Wu, F.-C. Fang, Y.-L. Liao, K.-T. Wong and C.-I. Wu, *Adv. Mater.* **2006**, *18*, 1216.

[29] S. A. Bagnich, A. Rudnick, P. Schroegel, P. Strohriegl and A. Kohler, *Phil. Trans. R. Soc. A* **2015**, *373*, 20140446.

[30] P. A. Vecchi, A. B. Padmaperuma, H. Qiao, L. S. Sapochak and P. E. Burrows, *Org. Lett.* **2006**, *8*, 4211.

5.5. Supplementary Information

Supplementary Text

Theoretical calculation

Optimization of range parameter, γ, for LCY-ωPBE functional

Optimization of the range parameter, γ, for LCY-ωPBE functional was performed according to ref.[1]. As shown in Supplementary Figure 5.1, the optimal value of γ was determined from the point exhibiting minimum J^2, where $J^2 = \sum_{i=0}^{1}[\varepsilon_H(N+i) + IP(N+i)]^2$. Here, N, $\varepsilon_H(N)$, and $IP(N)$ denote the electron number of the target molecule, its HOMO energy, and vertical ionization potential, respectively.

Calculation of k_{RISC}

In the equation (1), $\hbar$ and k_B denote reduced Planck constant of 6.58×10^{-16} eV·s and Boltzmann constant of 8.62×10^{-5} eV·K^{-1}, respectively.

Photophysical measurements

General procedures

Photoluminescence (PL) spectra were measured by a spectrofluorometer (FluoroMax Plus, HORIBA, Japan). Photoluminescence quantum yield (PLQY or Φ_{PL}) was measured with an absolute PLQY spectrometer (C9920-02, Hamamatsu Photonics, Japan) under a N_2 flow. For the solution experiments, we used a toluene solvent of spectrochemical analysis grade purchased from FUJIFILM Wako Pure Chemical Corporation. Phosphorescence spectra were observed at 77 K while fluorescence observed at an ambient temperature at 300 K. The transient PL decay measurements were conducted with a fluorescence lifetime measurement system (Quantaurus-Tau C11367-01, Hamamatsu Photonics, Japan) at 300 K. Temperature-dependent transient PL decay measurements were performed using cryostat (Oxford Instruments, Optistat DN2, UK) as shown in Supplementary Figure 5.5. Here, we obtained the PL lifetimes with two exponential fitting of respective curves over the region of 0–20 μs. Energetic barrier of ISC and RISC was determined by the Arrhenius plot of k_{ISC} and k_{RISC}, respectively, where the k_{ISC} and k_{RISC} were determined according to the ref.[2].

Determination of experimental k_{RISC}

Assuming that rate constants of radiative decay from T_1 to S_0 and non-radiative decay from T_1 to S_0 are zero, k_{RISC} can be expressed as following equation (4) according to ref.[3].

$$k_{RISC} \approx \frac{(k_p + k_d)}{2} \pm \sqrt{\left(\frac{k_p + k_d}{2}\right)^2 - k_p k_d \left(1 + \frac{{\Phi_{PL}}^d}{{\Phi_{PL}}^p}\right)}, \qquad (4)$$

where k_p, k_d, ${\Phi_{PL}}^p$ and ${\Phi_{PL}}^d$ are the rate constants of the prompt emission component, that of delayed emission component, PLQY for prompt component, and PLQY for delayed component, respectively.

Device fabrication and characterization of organic light-emitting diodes

Patterned indium-tin-oxide (ITO) substrates were cleaned by 10 min of sonication in detergent and H_2O (twice), 5 min exposure to hot steam of 2-propanol, and UV-O_3 irradiation for 30 min. Organic layers and Al cathode were deposited on the patterned ITO substrates with a deposition apparatus (SE-4260, ALS Technology, Japan) in different chambers both at ~10^{-4} Pa. The OLEDs with active areas of 4 mm^2 were finally encapsulated with glass caps containing getter films to remove oxygen and moisture. The performance of the OLEDs was characterized with an integrating sphere (C9920-12, Hamamatsu Photonics, Japan) equipped with a source meter (2400, Keithley, Japan). The device performances were measured in the forward direction in 200-meV steps.

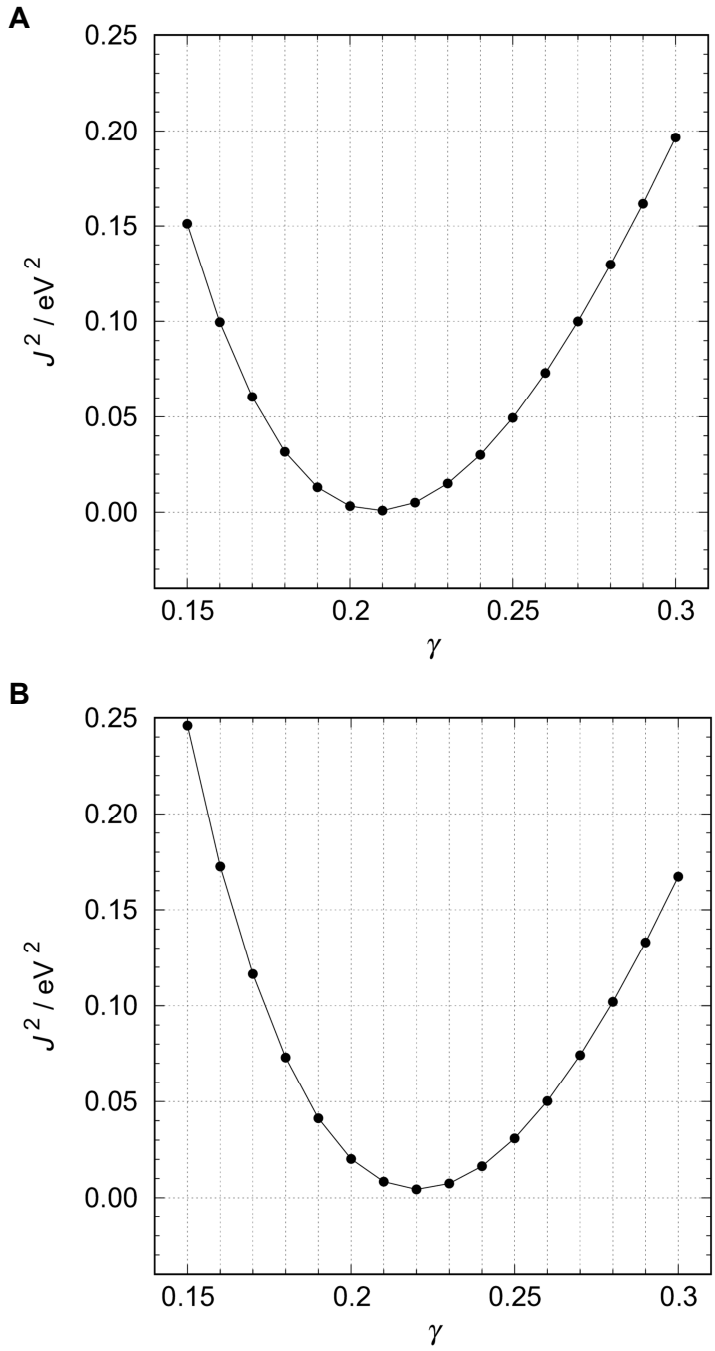

Supplementary Figure 5.1. J^2-γ plots of (**A**) S_1- and (**B**) T_1-opt. structure of MA-TA for LCY-ωPBE functional.

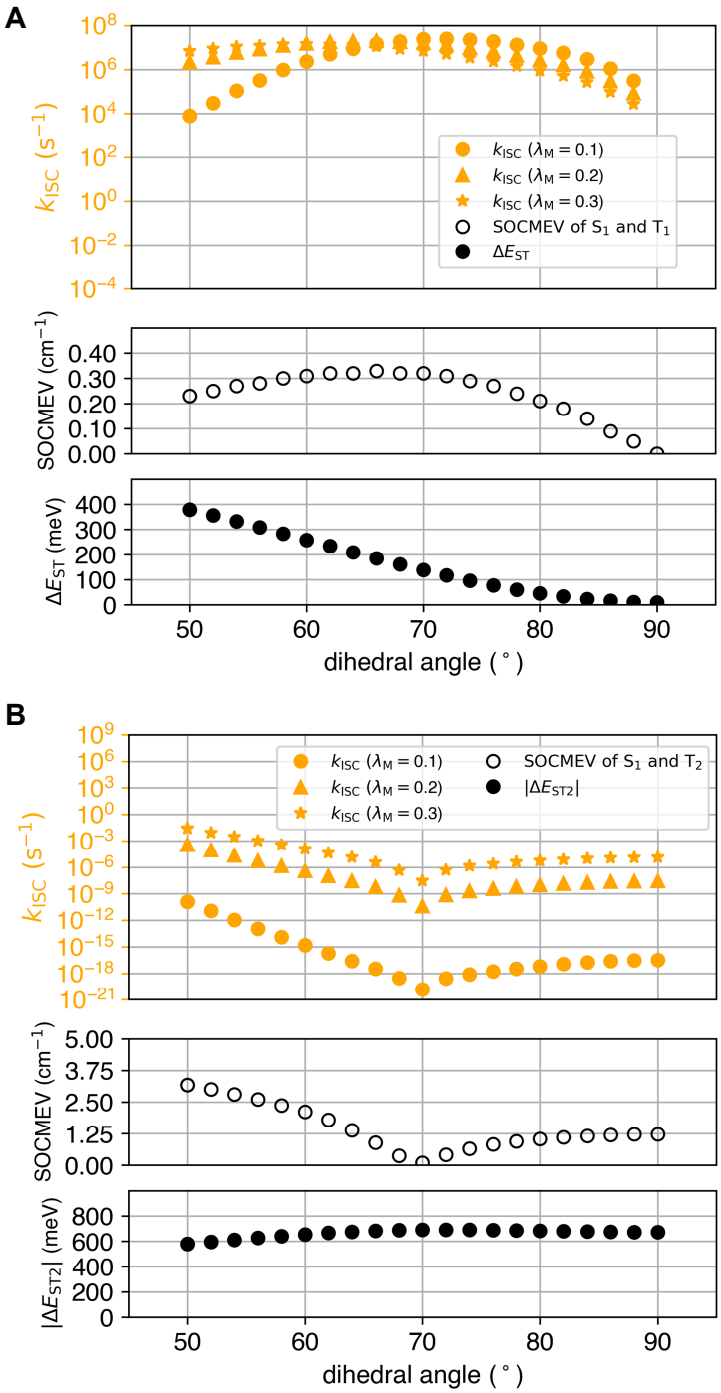

Supplementary Figure 5.2. Investigation on ISC dynamics (A) between S_1 and T_1 and (B) between S_1 and T_2. k_{RISC}, SOCMEV, and $|\Delta E_{ST2}|$ of MA-TA are exhibited as a function of dihedral angle, θ_d. Here, $|\Delta E_{ST2}|$ denotes the absolute value of the energy difference between S_1 and T_2.

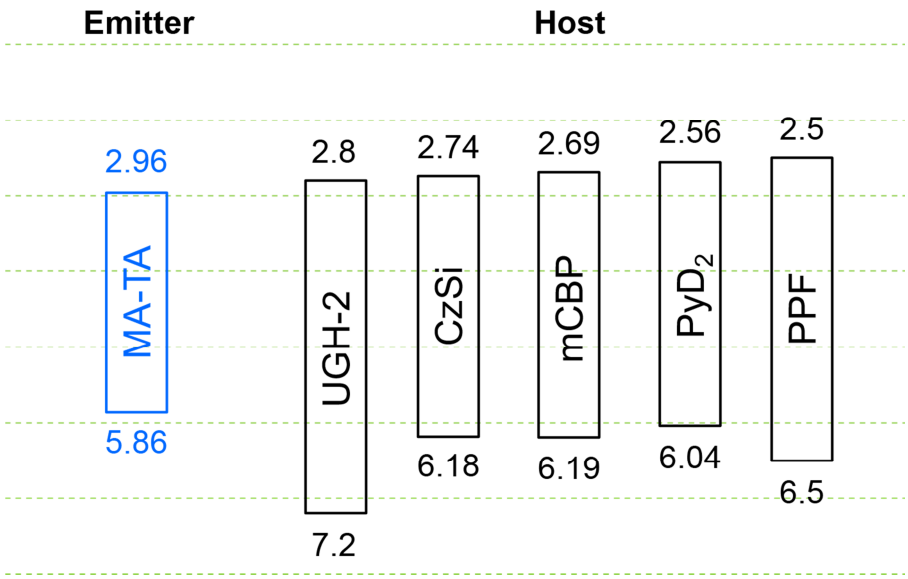

Supplementary Figure 5.3. Energy level diagrams of MA-TA and host materials. Values are in the unit of eV.

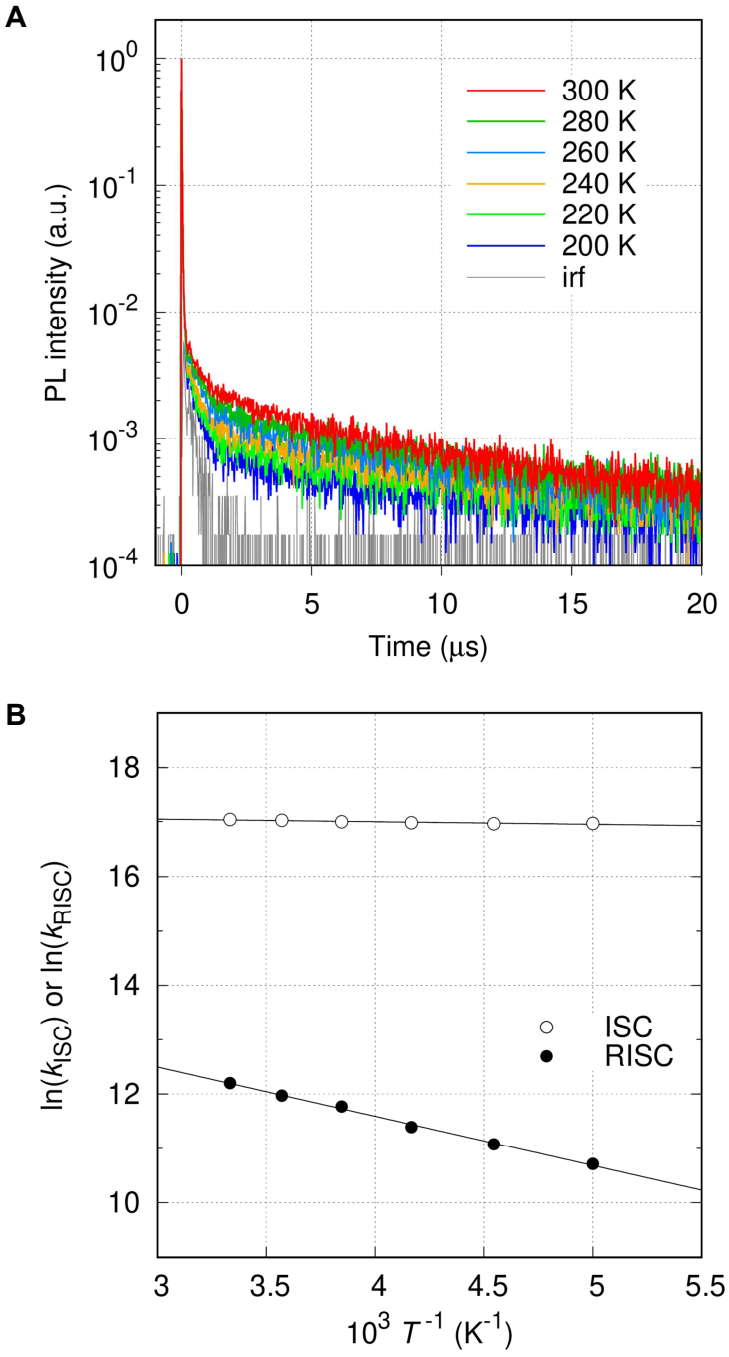

Supplementary Figure 5.4. Transient PL decay of a 20 vol%MA-TA:CzSi film measured at different temperature from 200 to 300 K. (A) PL decay curves at respective temperatures together with the instrument response function (irf). (B) Arrhenius plots for the ISC and RISC.

Supplementary Table 5.1. Calculated excitation energy of T_n and S_n states at the S_1- and T_1-opt. structures, where *n* denotes integers from 1 to 5.

Excited states	Energy levels / eV	
	S_1-opt.	T_1-opt.
T_1	2.5001	2.2933
T_2	3.1833	3.3271
T_3	3.2769	3.3658
T_4	3.3547	3.4382
T_5	3.4961	3.4794
S_1	2.5101	2.7392
S_2	3.4666	3.5112
S_3	3.6791	3.7659
S_4	3.7998	3.8212
S_5	4.1368	4.0863

Supplementary References

[1] H. Sun, C. Zhong and J. L. Brédas, *J. Chem. Theory. Comput.* **2015**, *11*, 3851.

[2] K. Masui, H. Nakanotani and C. Adachi, *Org. Electron.* **2013**, *14*, 2721.

[3] Y. Wada, H. Nakagawa, S. Matsumoto, Y. Wakisaka and H. Kaji, **2019**, 10.26434/chemrxiv.9745289.v1.

Summary

This thesis described investigations on development of highly efficient TADF molecules, and realization of highly efficient OLEDs. The results and findings in the respective chapters are summarized as follows.

In Chapter 1, a solution-processable green TADF material, named 3ACR-TRZ, was developed. 3ACR-TRZ is composed of electron donating fragment (9,9-dimethyl-9,10-dihydroacridine) and electron accepter fragment (2,4,6-triphenyl-1,3,5-triazine) and was found out to be a solution-processable TADF emitter. Owing to the steric hindrance of protons between the donor and the acceptor fragment, well-separated HOMO and LUMO are realized and ΔE_{ST} was experimentally determined to be very small value of 0.015 eV. 3ACR-TRZ clearly exhibited TADF with high photoluminescent quantum yield (PLQY) of 97% in a solid-state host layer and displayed a high maximum EQE (EQE_{MAX}) of 18.6% in its application to solution-processed OLEDs. From these results, it is found that the combination of 9,9-dimethyl-9,10-dihydroacridine and 2,4,6-triphenyl-1,3,5-triazine are promising for solution-processable molecular structure.

In Chapter 2, solution-processed host-free TADF OLEDs were developed using DMAC-TRZ, which consists of the same donor and acceptor core of 3ACR-TRZ, as TADF emitter. On the contrary to the ordinary TADF materials, DMAC-TRZ exhibited high PLQY of 84% even in the solution-processed neat film and concentration quenching were found to be suppressed. Furthermore, DMAC-TRZ exhibited bipolar carrier transporting property with both hole and electron mobilities of ~ 10^{-4} cm^2 V^{-1} s^{-1}. These results indicated that DMAC-TRZ is promising as a solution-processesable host-free TADF emitter. When the neat film of DMAC-TRZ was used as an emission layer for solution-processed OLED, EQE_{MAX} of 17.6%

was realized. Also, when device structure was optimized, relatively high EQEs of 16.3% and 13.7% at the practical brightness of 100 cd m^{-2} and 1,000 cd m^{-2}, respectively were realized. Deep-blue TADF-OLEDs always suffer from scarce host choices and the results in this Chapter provide an insight that the development of host-free deep-blue TADF materials release from the complicating host investigation.

In Chapter 3, deep-blue TADF materials were developed by simple adamantyl substitution. Starting from the acceptor fragment, 2,4,6-triphenyl-1,3,5-triazine, 1-adamantyl substituents were simply introduced to the structure, and MA-TA, FA-TA, and PA-TA were designed by combining to three different donor fragments. Owing to the electron donating ability of adamantyl substituents, LUMO energy of acceptor fragment was pushed up and the energy gaps of MA-TA, FA-TA, and PA-TA were drastically increased compared to that of sky-blue TADF emitter, DMAC-TRZ as introduced in Chapter 2. Also, solubility of the material and thermal stability of amorphous state were improved due to bulky structure and large molecular weight of the adamantyl substituent. MA-TA, FA-TA, and PA-TA can be dissolved into even in non-halogenated solvent such as toluene and exhibited excellent glass transition temperature of 147, 207, and 186 °C, respectively. As a result, it was found that the *adamantyl substitution* simultaneously endowed high solubility, excellent thermal stability, and efficient deep-blue emission. In their application to solution-processed deep-blue OLEDs, MA-TA, FA-TA, and PA-TA realized EQE_{MAX} of 22.1% with CIE(0.15, 0.19), EQE_{MAX} of 11.2% with CIE(0.15, 0.13), and EQE_{MAX} of 6.7% with CIE(0.15, 0.10), respectively.

In Chapter 4, systematic molecular design, “tilted face-to-face optimization (tFFO)”, to achieve very fast RISC was demonstrated. In order to realize fast RISC, control of not only ^{3}CT and ^{1}CT energy levels, but also that of locally excited triplet (^{3}LE) is required. It was found that distance (d_{DA}) between face-to-face aligned donor and acceptor fragments affect severely on

both ^{1}CT and ^{3}CT energy levels, but not on ^{3}LE states. On the basis of this observation, an example molecule was designed, where 9,9-dimethyl-9,10-dihydroacridine and 2,4-diphenyl-1,3,5-triazine was selected as donor and acceptor fragments, respectively. Theoretical calculation predicted that 1,8-position of triptycene provided the optimal d_{DA} to achive $E(^3CT) \approx E(^3LE) \approx E(^1CT)$, where $E(X)$ denotes the energy level of the X state. Importantly, completely parallel face-to-face alignment of the donor and acceptor fragments resulted in vanishingly small spin-orbit coupling matrix element value (SOCMEV) not only between ^{1}CT and ^{3}CT but also between ^{1}CT and ^{3}LE. This problem was solved by simply *"tilting"* the face-to-face alignment and was realized by connecting the donor and acceptor to 1,8-position of triptycene. The resulting molecule, TpAT-tFFO, was calculated to possess significant SOCMEV between ^{1}CT and ^{3}LE with well energy level matching, $E(^3CT) \approx E(^3LE) \approx E(^1CT)$. As expected, TpAT-tFFO exhibited very large rate constant of RISC ($k_{RISC} = 1.2\times10^7$ s^{-1}), which is fastest RISC in the purely organic molecule composed of only H, C, and N. Owing to the large k_{RISC}, excellent device performance was achieved and in particular, EQE roll-off was suppressed. Furthermore, when TpAT-tFFO was used as TADF sensitizer, bright blue OLED was achieved with CIE(0.15, 0.23) with EQE_{MAX} = 18.7% and maximum luminance = 18,000 cd m^{-2}. In particular, EQE roll-off was alleviated at high brightness and EQE of 14.4% and 11.8% even at 5,000 cd m^{-2} and much high brightness of 10,000 cd m^{-2}. From these observations, tFFO strategy is promising to achieve very fast RISC by simultaneous realization of energy level matching, $E(^3CT) \approx E(^3LE) \approx E(^1CT)$, and significant SOC. The tFFO strategy is versatile molecular design and can be expanded to various types, various numbers, and various combinations of donors, acceptors and scaffolds.

In Chapter 5, direct reverse intersystem crossing (RISC) between charge transfer (CT) type singlet and triplet states was theoretically and experimentally demonstrated to be feasible even

in purely organic molecules. At the S_1-optimized geometry, torsion angle between donor and acceptor of MA-TA was perpendicular (90º), which make S_1 and T_1 states the same CT states and the SOCMEV between S_1 and T_1 states resulted in zero. However, considering that the RISC process originates from T_1 state, T_1-optimized structure was considered and found that torsion angle between donor and acceptor was deviated from perpendicular (55º), which afforded non-zero SOCMEV. From these observations, ΔE_{ST} and SOCMEV of MA-TA were computed at different dihedral angles, and thereby k_{RISC} were calculated. Sufficiently high values from 10^5 to 10^6 s^{-1} were predicted when the torsion angle was slightly deviated from the perpendicular at around 80º even though S_1 and T_1 are substantially CT states. Experimentally, k_{RISC} values in different host materials were determined to be $0.6–1.8\times10^5$ s^{-1}, which were almost consistent with the calculation results. It is plausibly concluded that MA-TA dynamically experiences RISC directly between CT-type S_1 and T_1 states. It was also found that TADF performances of MA-TA were less sensitive to host selection. Host polarity and/or polarizability are known to severely influence on CT energy level, which sometimes change the order of CT and LE states. However, owing to the energy diagram of $E(^3\text{LE}) > E(^1\text{CT}) \approx E(^3\text{CT})$ and to direct RISC between CT-type S_1 and T_1 states, host polarity and/or polarizability have only little effect on ΔE_{ST}, and thus k_{RISC} and TADF performance in the case of MA-TA. Consequently, MA-TA displayed different EL emission colors depending on different host polarity and/or polarizability as is the case with conventional TADF materials, but exhibited EQE_{MAX} around 20% in all the host materials as is NOT the case with conventional TADF materials. This chapter provides insight into simple TADF molecular design which realizes efficient TADF and ensures insensitivity to host selection.

In this thesis, the author developed several TADF molecules and investigated the correlation between their molecular structures and their TADF performance. Large amount of

efforts have been devoted to develop TADF molecules and to understand the mechanism of TADF in the last one decade all over the world. However, performance of TADF materials especially of device lifetime in deep-blue OLEDs are still not yet sufficient enough for fulfilling the level of commercial utilization. Furthermore, even the mechanism of TADF is still under discussion. The findings in this thesis not only provide insight into molecular design, but also contribute to the progress in understanding of TADF phenomenon.

List of Publications

Chapter 1

1) Wada, Y.; Shizu, K.; Kubo, S.; Suzuki, K.; Tanaka, H.; Adachi, C.; Kaji, H.

"Highly efficient electroluminescence from a solution-processable thermally activated delayed fluorescence emitter"

Appl. Phys. Lett. **2015**, 107, 183303.

(Chapter 1 is the unedited Author's version of a Submitted Work that was subsequently accepted for publication in *Appl. Phys. Lett.*, copyright © American Institute of Physics after peer review. To access the final edited and published work see the following website: https://aip.scitation.org/doi/10.1063/1.4935237)

Chapter 2

2) Wada, Y.; Shizu, K.; Kubo, S.; Fukushima, T.; Miwa, T.; Tanaka, H.; Adachi, C.; Kaji, H.

"Highly efficient solution-processed host-free organic light-emitting diodes showing an external quantum efficiency of nearly 18% with a thermally activated delayed fluorescence emitter"

Appl. Phys. Express **2016**, 9, 032102.

(Chapter 2 is the unedited Author's version of a Submitted Work that was subsequently accepted for publication in *Appl. Phys. Express*, copyright © The Japan Society of Applied Physics after peer review. To access the final edited and published work see the following website: https://iopscience.iop.org/article/10.7567/APEX.9.032102)

Chapter 3

3) Wada, Y.; Kubo, S.; Kaji, H.

"Adamantyl Substitution Strategy for Realizing Solution-Processable Thermally Stable Deep-Blue Thermally Activated Delayed Fluorescence Materials"

Adv. Mater. **2018**, 30, 1705641.

(Chapter 3 is the unedited Author's version of a Submitted Work that was subsequently accepted for publication in *Adv. Mater.*, copyright © WILEY‐VCH Verlag GmbH & Co. KGaA after peer review. To access the final edited and published work see the following website: https://onlinelibrary.wiley.com/doi/full/10.1002/adma.201705641)

Chapter 4

4) Wada, Y.; Nakagawa, H.; Matsumoto, S.; Wakisaka, Y.; Kaji, H.

"Molecular Design Realizing Very Fast Reverse Intersystem Crossing in Purely Organic Emitter"

Submitted.

(Previous version of a Submitted Work was posted on a preprint server. *ChemRxiv.* **2019**, DOI:10.26434/chemrxiv.9745289.v1. See the following website: https://doi.org/10.26434/chemrxiv.9745289.v1)

Chapter 5

5) Wada, Y.; Wakisaka, Y.; Kaji, H.

"Efficient direct reverse intersystem crossing between charge transfer-type singlet and triplet states in purely organic molecule"

To be submitted.

Other Publications

6) Shizu, K.; Miwa, T.; Wada, Y.; Ogata, I.; Kaji, H.

Thermally activated delayed fluorescence emitter with symmetric acceptor-donor-acceptor structure

J. Photopolym. Sci. Technol. **2017**, 30, 475-481.

7) Zhang, D. D.; Suzuki, K.; Song, X.; Wada, Y.; Kubo, S.; Duan, L.; Kaji, H.

Thermally Activated Delayed Fluorescent Materials Combining Intra- and Intermolecular Charge Transfers

ACS Appl. Mater. Interfaces **2019**, 11, 7192-7198.

Acknowledgements

The studies presented in this thesis were carried out under the direction of Professor Hironori Kaji at Institute for Chemical Research, Kyoto University. The author would like to express his gratitude to Professor Hironori Kaji for his invaluable suggestion and kind guidance throughout the study.

The author is grateful to Professor Hirofumi Sato and Professor Shu Seki, Department of Molecular Engineering, Graduate School of Engineering, Kyoto University, for their guidance in preparing this thesis.

Sincere appreciation is due to Professor Chihaya Adachi and Dr. Hiroyuki Tanaka, Center for Organic Photonics and Electronics Research (OPERA), Kyushu University for the enormous collaboration in this study. The author is also sincerely grateful to Assistant Professor Tatsuya Fukushima, Assistant Professor Katsuyuki Shizu, Assistant Professor Katsuaki Suzuki, Dr. Hiromichi Nakagawa, Mr. Shosei Kubo, Mr. Takuya Miwa, Mr. Yasuaki Wakisaka, and Mr. Soma Matsumoto, at Institute for Chemical Research, Kyoto University, for their significant contribution in this study. The author is particularly grateful to Technician Kyohko Ohmine and Technician Ayaka Maeno at Institute for Chemical Research, Kyoto University, for their kind support of NMR measurement in this study.

The author acknowledges to his colleagues, Dr. Furitsu Suzuki, Mr. Fumiya Tanaka, Mr. Hirotaka Ishibashi, Mr. Isamu Ogata, Mr. Tsutomu Miura, Mr. Hiroki Uratani, Mr. Sotaro Higaki, Mr. Tomoya Misono, and Ms. Ayaka Sawada, Mr. Kazuki Moriwaki, Mr. Yu Kusakabe for their useful discussion and encouragement. Thanks are also given to other staffs and students at Institute for Chemical Research, Kyoto University, for their kindness during this study.

This study was supported by Japan Society for the Promotion of Science (JSPS) through

the “Funding Program for World-Leading Innovative R&D on Science and Technology (FIRST Program).” This work was also supported by JSPS KAKENHI (Grant Nos. 25248053, 17H01231, and 17J09631) and the Collaborative Research Program of Institute for Chemical Research, Kyoto University (Grant No. 2015-14). NMR measurements were supported by the Joint Usage/Research Center (JURC), Institute for Chemical Research, Kyoto University, Japan. Computation time was provided by the SuperComputer System, Institute for Chemical Research, Kyoto University, Japan, and the Academic Center for Computing and Media Studies (ACCMS), Kyoto University, Japan. NMR measurements were supported by the Joint Usage/Research Center (JURC), Institute for Chemical Research, Kyoto University, Japan.

Finally, the author heartily wishes to express his thanks to his parents, Kouki Wada and Yumiko Wada, his grandmother, Toshiko Wada and all his relatives. Also, the author would like to dedicate special thanks to my late grandfather, Ihachi Wada and late grandmother, Tomie Isojima.

Yoshimasa Wada